Turbulent drag reduction using dolphin-inspired ultrasonic skin microvibrations

イルカを規範としたマイクロ超音波壁面振動による乱流抵抗低減

February 2025

WANG DONGYUE
Graduate School of Science and Engineering
CHIBA UNIVERSITY

（千葉大学審査学位論文）

Turbulent drag reduction using dolphin-inspired ultrasonic skin microvibrations

イルカを規範としたマイクロ超音波壁面振動による乱流抵抗低減

February 2025

WANG DONGYUE

Graduate School of Science and Engineering

CHIBA UNIVERSITY

ABSTRACT

The dolphin, as a high-speed marine species, possesses exceptional hydrodynamic performance. Its ability to cruise at high speeds over long distances with low energy consumption is one of the capabilities highly sought after in various modes of transportation. Biologists and engineers have long been dedicated to understanding the hydrodynamics enabling dolphins to swim at speeds seemingly beyond their energetic capabilities, a phenomenon known as Gray's paradox. Drag reduction is considered the key to achieving such high levels of performance. Dolphins are able to reduce drag primarily due to streamlining of the body and appendages and special behaviors, such as compliant skin, surface microstructures, polymer additives, boundary layer heating and acceleration. However, these factors, through identified, are still insufficient to fully explain the mystery behind Gray's paradox. Inspired by the skin microvibrations observed during the swimming of a dolphin, we propose that the wall (skin)-bounded turbulent flows-induced boundary layer would be dynamically altered by such skin vibrations, which could achieve a novel turbulent drag reduction.

The dolphin skin, characterized by high flexibility and sensitivity, allows it to respond to the stimulations acted on it, resulting in micro-oscillations on its surface. In this thesis, we hypothesize that the high-intensity and ultrasonic click signals emitted from the melon can act as an internal excitation source to drive dynamic oscillations on dolphin skin, in the form of longitudinal micro-ultrasonic wave (LMUW). A comprehensive computational fluid dynamic (CFD) study is performed in terms of the LMUW-induced near-flow variations, dynamic boundary model and drag reduction effect. The addition of LMUW based on a flat plate model is firstly simulated at a fixed Reynolds number (Re) of 1.26×10^6. Three different LMUW modes were applied, including two traveling waves (upstream and downstream) and a standing wave. Due to the micro-scale and high-frequency features, the LMUW greatly impacts the near-wall flow but without exerting significantly influence in the surrounding macroscale flow field. The introduction of LMUW creates a novel dynamic boundary layer which is highly related to the motion modes, leading to significant variations in the drag

force distributions. Friction drag becomes negative, i.e., thrust, in the upstream traveling and standing LMUWs, whereas it significantly increases in the downstream LMUW mode. In contrast, pressure drag induced by downstream LMUW is reduced, even completely eliminated, while it increases in the other two modes. The negative pressure drag induced by downstream LMUW is capable of offsetting the increase in friction drag, ultimately reduction the total drag, thus introducing a novel pressure-dominated drag reduction mechanism.

Informed and validated by numerical results, we further derived a theoretical model for the velocity profile of the dynamic boundary layer, capable of effectively capturing the essential boundary flows and analytically correlating the LMUW-excited near-wall turbulent flow with the friction- and pressure-drag reduction. The theoretical model reveals that variations in an analytical function $G(\psi)$ in the streamwise velocity equation plays a dominant role in determining both the friction and pressure drag. More importantly, different from the conventional drag-reduction methods that directly suppress turbulent fluctuations, the LMUW-induced drag reduction strategy enables both the direction and magnitude of the friction- and pressure-based drag to be manipulated by tuning the wavy wall motion.

Additionally, considering that dolphins as biological organisms, likely achieve drag reduction through a combination of multiple factors, the streamlined body shape is integrated with skin LMUW. A standard streamlined model NACA0012 with skin LMUW on its surface is applied, firstly with a fixed incoming flow and the same *Re* as the previous flat plate model. When the arrangement of skin LMUW motion aligns with the actual arrangement of microstructures on dolphin skin - specifically, covering large area of the body and symmetrical distributions about the centerline - the addition of downstream traveling LMUW can significantly reduce, or even eliminate, total drag acting on the body without altering lift under small angle of attack conditions typical of dolphin swimming. This drag-reduction advantages brought by skin vibrations can also be reflected in subsequent actual swimming calculations by simulating dolphin propulsion through the addition of a tail fluke motion on the streamlined model. The negative pressure generated by the downstream traveling LMUW provides an additional skin thrust without affecting the tail propulsion, thereby aiding in accelerating the swim and improving swimming efficiency.

Therefore, we infer that this dynamic drag reduction method, based on the skin

LMUW motion, has great potential to further unravel the sophisticated drag reduction mechanisms in association with Gray's paradox and provides an active drag reduction strategy by manipulating both the direction and magnitude of boundary flow, exciting a new inspiration for the development of drag reduction technology.

Key words: dolphin swimming, drag reduction, skin microvibration, dynamic boundary

CONTENTS

Chapter 1 GENERAL INTRODUCTION

1.1 BACKGROUND AND MOTIVATION

Human development is inseparable from the exploitation and utilization of energy, making energy issues a strategic concern for national economic and social development. With the continuous advancement of human society, the energy consumed to overcome surface friction in various transportation equipment and pipeline transport devices has become a significant component of fuel consumption. For instance, the surface friction resistance accounts for approximately 50% of the total drag in conventional aircraft and marine vehicles [1,2]. Therefore, the discovery of drag reduction phenomena is primarily significant in enhancing fluid transport efficiency and reducing driving energy consumption, offering substantial energy-saving value.

The issue of drag reduction can be tracked back to the 1930s. For the following four decades, research on drag reduction was based on the assumption that “the smoother the surface, the lower the resistance”, attempting to reduce surface frictional resistance by decreasing surface roughness. It was not until the 1970s that scientists at NACA discovered that V-shaped grooves aligned with the flow direction, simplified from the microstructure of shark skin, had the ability to reduce drag [3]. This finding questioned the traditional belief that smoother surfaces automatically lead to reduced resistance. Subsequently, researchers conducted extensive studies on groove drag reduction technology, leading to the gradual development of turbulence drag reduction theories and techniques that continue to evolve to this day.

When an object moves at a certain speed within a fluid medium, a very thin fluid boundary layer forms closely along the surface of the vehicle due to the viscosity of liquid. Within this boundary, laminar flow exhibits a smooth and orderly pattern, whereas turbulent flow appears disorganized and chaotic. And there exists numerous vortices and irregular flows in a turbulent state, which increases shear stress and momentum transfer, leading to greater friction and consequently increased drag [4,5]. Therefore, the key to achieving wall

friction drag reduction lies in optimizing the near-wall boundary flow structure of vehicles to reduce the value of viscous shear stress. Currently, drag reduction technology development, based on the underlying mechanisms, can be generally divided into two main approaches: one targets maintaining laminar flow to delay the transition from laminar to turbulent boundary layers, while the other aims to reduce turbulent drag by modifying turbulent flow structures near the vehicle surface [1].

Marine high-speed fish, including whales, sharks, dolphins, and tuna, have developed extraordinary swimming and survival abilities through long natural evolution, providing natural inspiration for drag reduction research. From a hydrodynamic perspective, the remarkable swimming abilities of these fish are essentially a matter of flow control. Fish can effectively control the flow structure of their surrounding fluid by flexibly deforming their bodies or fins and through undulating movements of body according to their requirements. Therefore, describing hydrodynamic models of fish and revealing their low-drag, high-efficiency swimming mechanisms have great scientific and engineering value, driving drag reduction technology using bionic principles to become a popular research topic. Dolphin, as one of the marine high-speed fish, exhibits exceptionally superior hydrodynamic performance. Its low-energy, long-distance, high-speed cruising capabilities are highly desired in various transportation tools. Unlike sharks that rely on the microstructures of their skin for drag reduction, dolphin's flexible skin suggests that there may exists a dynamic adjustment mechanism during cruising to adapt to external flow fields. This dynamic adjustment can be achieved by manipulating the movement or deformation of the skin to alter boundary flow structures and reduce drag. Despite the diverse and varied research on drag reduction mechanisms of dolphin, it has not yet fully explained its high-efficiency and low-resistance swimming characteristics. Therefore, based on the biological functional characteristics of dolphin, exploring the reasons for its excellent hydrodynamic performance, conducting research on drag reduction mechanism and low-friction biomimetic skin design, seeking engineering-applicable flow control measures, are of great significance for innovative design of drag reduction technology and achieve higher economic and environmental goals such as reducing fuel consumption and greenhouse gas emissions.

1.2 TURBULENT DRAG REDUCTION TECHNOLOGIES

The scientific community is dedicating substantial efforts to advancing turbulent drag-reduction technologies, which would significantly lower fuel consumption. Achieving friction drag reduction primarily involves two approaches: passive control and active control. Passive approaches often involve shape optimization and surface microstructure arrangement without the need to consume additional energy. In contrast to passive ones, active flow control methods are capable of offering greater flexibility and achieving better drag-reduction performance but require the energy consumption by an external source [6,7].

1.2.1 Passive approaches

1.2.1.1 Drag reduction using micro-structured surfaces

Shark skin provides much of the inspiration for the drag reduction achieved by the non-smooth surfaces, which possesses unique properties. As shown in figure 1-1(a), there exists the scales known as dermal denticles on shark skin, which contain specially sized and spaced grooves (generally 0.2-0.5 mm in size with the grooves spaced 30-100 μm) aligned parallel to the swimming direction indicated by the arrows [4,8]. Scientists have simplified this shark skin morphology into a two-dimensional (2D) riblets shape in the streamwise direction to analyze its drag reduction effect in both experimental and computational methods and discovered that these riblets structures have demonstrated up to a 10% drag reduction compared with a smooth, flat surface, breaking through the tradition of smoother drag [3,8–13]. Researchers have not reached a consensus on the exact drag-reduction mechanism of this groove surface. Two possible drag reduction mechanisms have been proposed including the vortices control in the turbulent flow and the turbulence fluctuations reduction in the crossflow direction. In the first case, the vortices formed by the riblet surfaces are considered to play a crucial role. Microgrooves on the surface can prevent the near-wall streamwise vortices in figure 1-1(b) from falling into the valleys when the vortex size exceeds the groove opening width, and limit the spanwise motion of vortex, shifting intense turbulent activities occurring away from the wall and filling the groove bottoms with low-speed fluid. Additionally, because the spanwise motion of streamwise vortices is restricted, secondary vortices are generated and move into the groove valleys, weakening the ejection of low-

momentum fluid into the outer region and thereby inhibiting the momentum exchange process [13–15]. The second mechanism, also known as the "protrusion height theory", was firstly proposed by Bechert et al shown in figure 1-1(c). They suggested that when the rib tips sufficiently extend above the starting point of the velocity profile, the longitudinal microgrooves align the turbulent flow with the direction of mean flow by suppressing the cross-flow component fluctuation *w'*. By diminishing the near-wall *w'* fluctuations, momentum transfer in the boundary turbulent flow will also be decreased, leading to a reduction in wall shear stress [16,17].

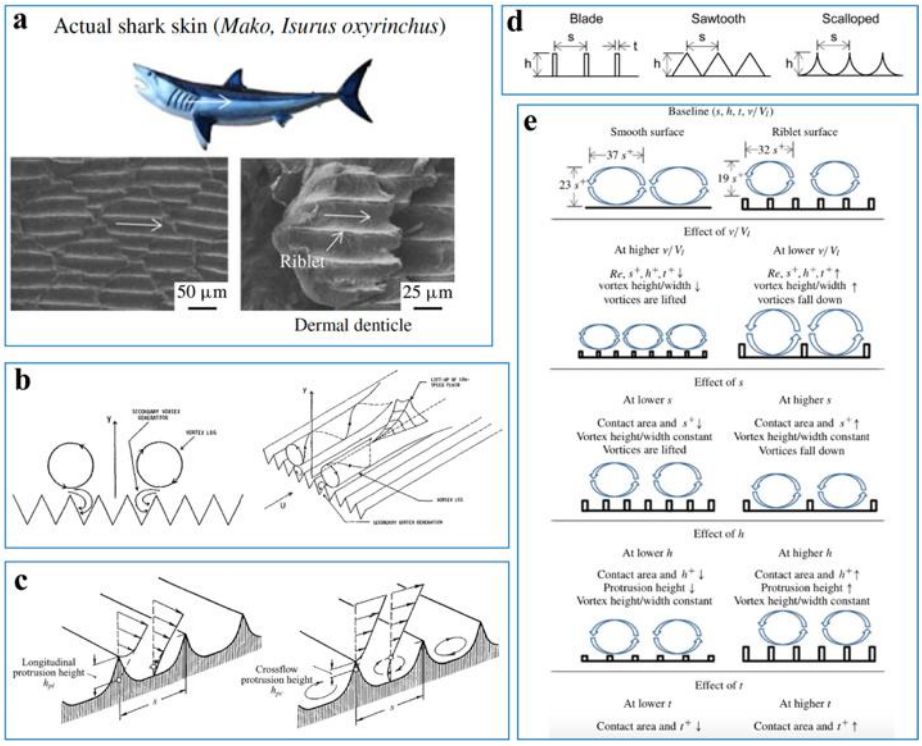

Figure 1-1 Microgrooves drag reduction inspired by shark skin.

(a) SEM micrographs of shark skin [8]; (b) "Vortices control" mechanism [14]; (c) "Protrusion height" mechanism [17]; (d) Typical groove shape [8–10]; (e) Drag reduction effect influenced by rib geometry and flow characteristics [8].

It is worth noting that both mechanisms for achieving drag reduction are highly dependent on the riblet geometry and flow properties. In the research conducted by Martin et al., they established three typical groove shape [figure 1-1(d)]–blade, sawtooth, and

scalloped–to explore the drag reduction effect influenced by the microgroove geometry and flow characteristic and found that the blade riblet achieves the greatest drag reduction. The effect exploration was based on this blade structure and the results agreed more with the first mechanism. The rotation of streamwise vortices along the axis aligns with the direction of mean velocity, producing ejection and sweeping motions where fluid with high velocity interacts and mixes with the near-wall low-speed fluid. This interaction generates regions of elevated shear stress and, consequently, increased the resistance. An appropriate selection of riblet size can be helpful to lift these vortices away from the surface of the wall, decreasing the region subjected to high shear stress and thus decreasing drag [figure 1-1(e)]. Optimal drag reduction is achieved under the condition of the vortices being approximately 1.5 times the rib spacing size. As the vortices approach and become smaller than the size of riblet spacing, the riblet will increase the drag [8–10].

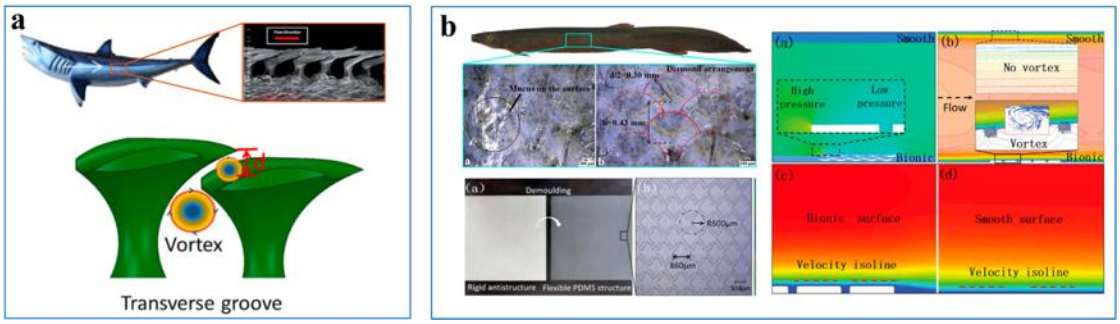

Figure 1-2 Drag reduction induced by micro-structured surfaces

(a) Shark denticles [12]; (b) Drag reduction induced by the surface morphology of loach [18]

The staggered distribution of shark denticles results in its skin not merely a simple 2D groove but a complex 3D structure. Research have shown that the transverse groove beneath shark denticles also play a positive role in drag reduction [19,20]. As illustrated in figure 1-2(a), stable low-speed vortices form in the transverse groove due to the interaction between denticles and fluid. On the one hand, the presence of these vortices induces reverse flow on the surface of denticles, leading to negative values of shear stress in streamwise direction in certain areas, thereby reducing wall friction. On the other hand, these vortices prevent the external flow from directly contacting the skin surface, acting similarly to rolling bearings.

This increases the thickness of viscous sublayer, reduces the near-wall velocity gradient, and thereby lowers wall shear stress. This phenomenon is also observed in the skin morphology drag reduction of other fish species, such as loach. Similar to shark skin, the orderly arrangement of the bionic loach scales in figure 1-2(b) induces a stable low-pressure region within the bionic scale area that absorbs fluid from the surroundings, thereby filling the scale area with liquid and facilitating the transition of interaction between the liquid and the substrate to liquid-liquid contact, thus lowering the flow resistance. Additionally, the vortices formed in the gap between scales also cause the buffering effect, contributing to drag reduction [18,21].

1.2.1.2 Drag reduction using superhydrophobic surfaces

The drag reduction method of superhydrophobic surfaces (SHS) is inspired by lotus leaves. Researchers found that the surface of a lotus leaf is covered with a dual scale roughness created by papillose epidermal cells and an additional layer of epicuticular waxes. The roughness of the papillae allows the contact angle to exceed 150°, resulting in a decreasing surface/liquid contact area with the liquid droplets resting solely on the tips of the micro/nano-texturing shown in figure 1-3(a). Consequently, contaminating particles are captured by the droplets and removed as the liquid rolls off the leaf, a phenomenon termed the “Lotus Effect” by Barthlott and Neinhuis [22–26]. The effect, when applied to underwater vehicles, not only facilitates self-cleaning but also holds great potential for drag reduction. Watanabe et al. verified that this superhydrophobic surface could achieve a drag reduction effect of up to 14% in laminar pipe flow [27]. Additionally, the velocity profile obtained from fitting experimental data confirmed that the flow velocity at SHS is not zero [27–31]. Considering the wetting characteristic of SHS, researchers believe that there may exist two main reasons for its drag reduction mechanism. First, SHS with very low surface energy reduces the intermolecular attraction between liquid and solid, transforming the originally no-slip boundary condition into a slip boundary condition at the surface. Tretheway and Meinhart found in experiments with superhydrophobic microchannels that an obvious velocity slip occurs on the wall surface, with the slip velocity reaching approximately 10% of the free-stream velocity. Thus, they considered the wall slip caused by the no-adhesion of SHS [figure 1-3(b)] as one of the key reasons for achieving drag reduction [32,33]. The second

reason is that researchers believe surface tension prevents liquid from entering the micro/nanostructure on the surface, causing air to be trapped within the micro/nanostructure and forming an air-liquid interface, which reduce the solid/liquid contact area. And due to this air-liquid interface, significant slip velocity shown in figure 1-3(c) is generated. The slip velocity at the center of the air-liquid interface can reach 60% of the average mainstream velocity, resulting a considerable reduction in the velocity gradients near the wall and thereby achieving a substantial drag reduction effect [33–37].

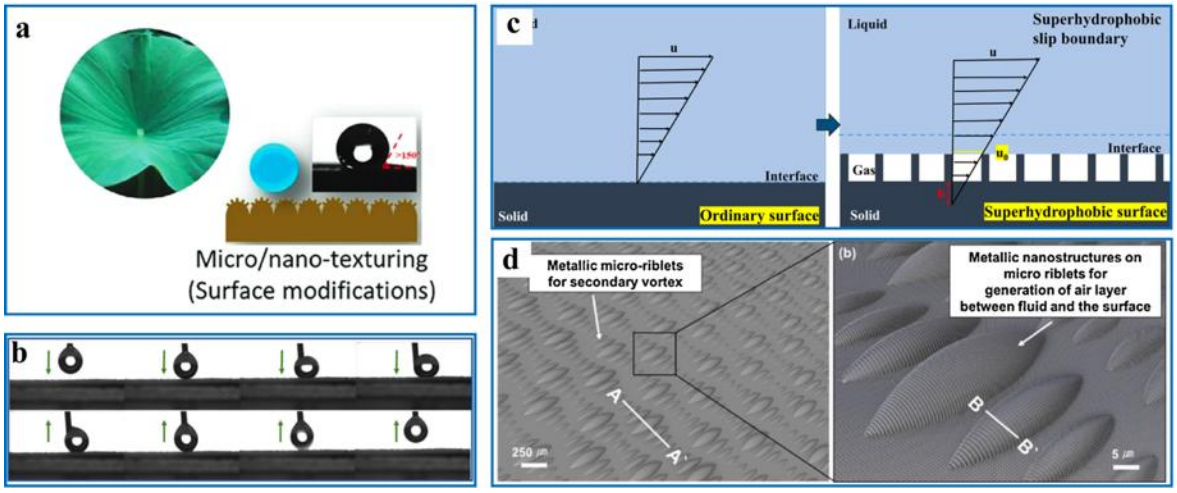

Figure 1-3 Drag reduction of superhydrophobic surfaces

(a) Lotus effect [26]; (b) No-adhesion of superhydrophobic surfaces [31]; (c) Boundary slip model [33]; (d) Combination of micro-riblets and superhydrophobic properties [38].

Combining the above two reasons, the key of drag reduction by SHS relies on the presence of slip velocity near the superhydrophobic surface, which reduces the boundary velocity gradient, thereby lowering the wall shear stress and delaying the transition of the flow state from laminar to turbulent. Additionally, the micro/nano-texturing on SHS is beneficial to form a low-shear gas-liquid interface, reducing the contact between liquid and solid. The combination of these factors results in the excellent drag reduction of SHS. Due to the advantages provided by SHS in drag reduction and self-cleaning, scientists are also exploring combining this superhydrophobicity with other drag reduction methods, such as microgrooves. As indicated in figure 1-3(d), a drag reduction surface with highly ordered

hierarchical structures: nanostructures existing on micro-riblets allows for the simultaneous integration of two strategies: the air-layer effect created by nanostructures and secondary vortex generation facilitated by micro-riblets, resulting in even more superior drag reduction performance [38,39].

1.2.1.3 Drag reduction by adding polymer additives

Nearly all fished are covered with an integumental mucous secretion that plays a vital role in various aspects of their biology, including disease resistance, offspring care, shelter, and locomotion. In the context of locomotion, the layer of mucus is believed to reduce frictional drag [40,41]. Inspired by the drag reduction achieved by fish mucus, research using polymer additives to decrease drag has been ongoing for a long time. As early as the 1940s, scientists discovered that adding polymers to fluid mediums can reduce flow resistance, which is known as the "Toms phenomenon" [42,43]. At present, a unified mechanism for the this drag reduction method has yet to be established. Representative hypotheses include: 1) the addition of polymer additives reduce the near-wall velocity gradient, thereby reducing the frequency of turbulent bursts, stabilizing the boundary flow, and consequently reducing friction drag; 2) the polymer additives are affected by the boundary layer flow, inducing a compliant effect and forming a gradient in elastic modulus shown in figure 1-4, effectively reducing turbulent pressure fluctuations and thereby reducing the drag [44,45]. Although this drag reduction method offers advantages such as high efficiency and simplicity of use and has wide applications in various engineering fields such as firefighting and pipeline transportation, it also has certain drawbacks including the need for continuous injection, poor environmental adaptability and limited cost-effectiveness, which have hindered its application in underwater vehicles. Therefore, researchers are considering combining polymer drag reduction technology with other surface drag reduction techniques to achieve complementary advantages between different methods and thereby achieve better drag reduction effect. Studies have shown that combining polymer additives with microgrooves, by using a slow-release coating technique to release polymer solutions at the bottom of grooves, significantly achieves friction drag reduction in turbulent boundary layer, thus obtaining better drag reduction effects [15,46–50].

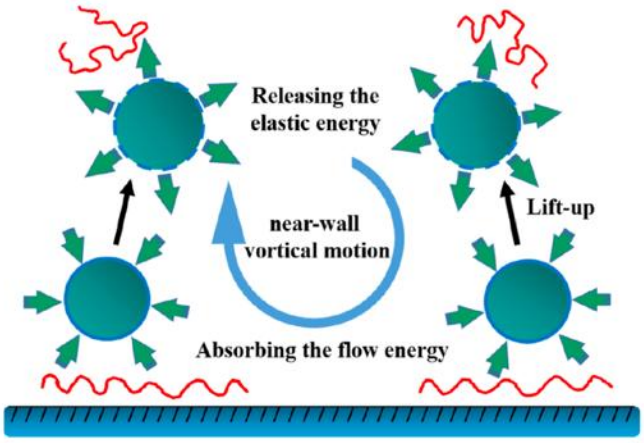

Figure 1-4 Schematic representation of drag reduction mechanism induced by polymer additives [45]

1.2.2 Active approaches

1.2.2.1 Drag reduction through gas lubrication

For objectives moving in the liquid, the near-wall flow can be substituted with a gas layer, significantly reducing the density near the surface. This presents a promising approach for achieving friction drag reduction [51]. For ships operating at low speeds, where friction drag constitutes the majority of resistance, bubble injection has demonstrated significant practical value in reducing drag. The bubble injection rate and mode significantly influence the drag reduction mechanisms. When the rate of air injection increases, drag reduction by microbubble gradually change to by mixture state, and eventually evolving into the drag reduction by a whole air layer, shown in figure 1-5 [52]. Although the primary mechanism of drag reduction for all these methods relies on the low viscosity of air medium, there still exists a slight difference between bubble drag reduction (BDR) and air layer drag reduction (ALDR). Specifically, beyond the low shear stress resulting from reduced viscosity, BDR also affects the coherent structure in turbulent boundary layer. This effect is accompanied by the formation of air waves, which further contribute to drag reduction [53]. These air (void) waves are not induced by the local interactions between bubble and bubble but arise from interacting the void with the internal structure of turbulent boundary layer over a more dynamic scale [53,54]. The development of void wave is an intrinsic process influenced by multiple factors such as bubble buoyancy, wall wettability and sliding bubble behavior. The generation of void waves within turbulent boundary layer improves the effect of drag

reduction [53–55]. ALDR requires a higher injection rate to be maintained, but it can directly replace the original liquid/solid boundary with a gas/solid boundary, significantly reducing frictional resistance. According to the investigation of Elbing et al., the friction drag reduction exceeding 80% can be achieved across the whole smooth model in the case of ALDR [56]. Although the drag reduction in ALDR is more effective than BDR, maintaining the conditions necessary for the formation of the air is challenging. To address this challenge, Du et al. focused on improving the precision of surface cavity structures by injecting gas into a superhydrophobic surface. The integration of injected bubbles with a superhydrophobic surface has been verified to be an effective method for sustaining the air layer [53,57]. But some research indicates that the microbubble drag reduction method is more suitable for low-speed vessels. As the speed increases, the peak drag reduction rate diminishes [53,54]. However, when the submerged object moves at a sufficient high speed in water, a very important flow phenomenon, known as cavitation, is noticed. Based on this gas generation phenomenon, artificial ventilation and cavitator are employed with the aim of controlling the instability, noise and other disadvantages caused by cavitation as much as possible, while simultaneously reducing frictional resistance by forming an air layer for the high-speed underwater vehicle [58–62].

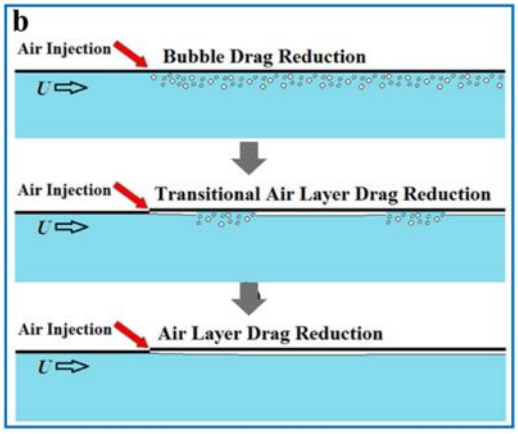

Figure 1-5 Air lubrication: transition from BDR to ALDR [52]

1.2.2.2 Drag reduction induced by near-wall forcing

The friction drag increase in turbulent boundary arises from the intensified momentum

exchange driven by the quasi-streamwise vortices [63]. Therefore, once the boundary layer becomes fully turbulent, flow control strategies primarily focus on minimizing the mixing of streamwise momentum within the boundary region, which is typically accomplished by suppressing the turbulent fluctuations in the wall-normal direction. From a time-averaged perspective, reducing these fluctuations decreases wall shear stress in turbulence, resulting in a friction drag reduction dependent reducing the near-wall velocity gradient [7].

Based on this objective, a direct approach is to monitor the motion at a given height in the wall-normal direction and then counteract the wall-normal motion through a localized and dynamically adjustable opposing injection, implemented via blowing/suction techniques or by inducing opposing momentum through body forces. This method is called "opposition control" and firstly proposed by Choi et al. in 1994 [64], which can effectively reduce wall-normal fluctuations and turbulent shear stress, thereby achieving the drag reduction. Fukagata et al. [65] reviewed the turbulent drag reduction mechanisms induced by streamwise traveling waves achieved by blowing/suction from wall or wall deformation and point out their significant drag reduction capabilities and relevant mechanisms. As illustrated in figure 1-6(a), wall blowing and suction typically involve applying a control input v_w (i.e., blowing/suction velocity) on the channel wall. v_w on the upper and lower surface is symmetrical and we give the velocity of the lower surface as an example:

$$v_w = a\cos[k(x - ct)], \qquad (1-1)$$

where k and c represent the wavenumber and wave speed of the streamwise traveling wave, respectively. The position of channel surface remains unchanged, but the variation in velocity at different positions over time creates the effect of traveling waves. Min et al. [66] firstly explored the effect of wall blowing/suction, forming a streamwise traveling wave, in a 2D laminar channel flow under a constant flow rate condition at Re=2000. As shown in figure 1-6(b), the upstream traveling waves (UTWs, $c < 0$) result in a negative drag increment at the condition of $c < -1$, suggesting a sub-laminar drag. Conversely, the drag increment in downstream traveling waves (DTWs, $c > 0$) always positive, indicating no drag reduction effect. Researchers proposed a "pumping effect" to explain this phenomenon [67–69]. The upstream traveling blowing/suction can reduce the pressure gradient required to maintain a constant flow rate. In other words, the addition of UTWs helps generate the pressure gradient needed to sustain the flow which has been validated by Luchini [70] in their numerical study

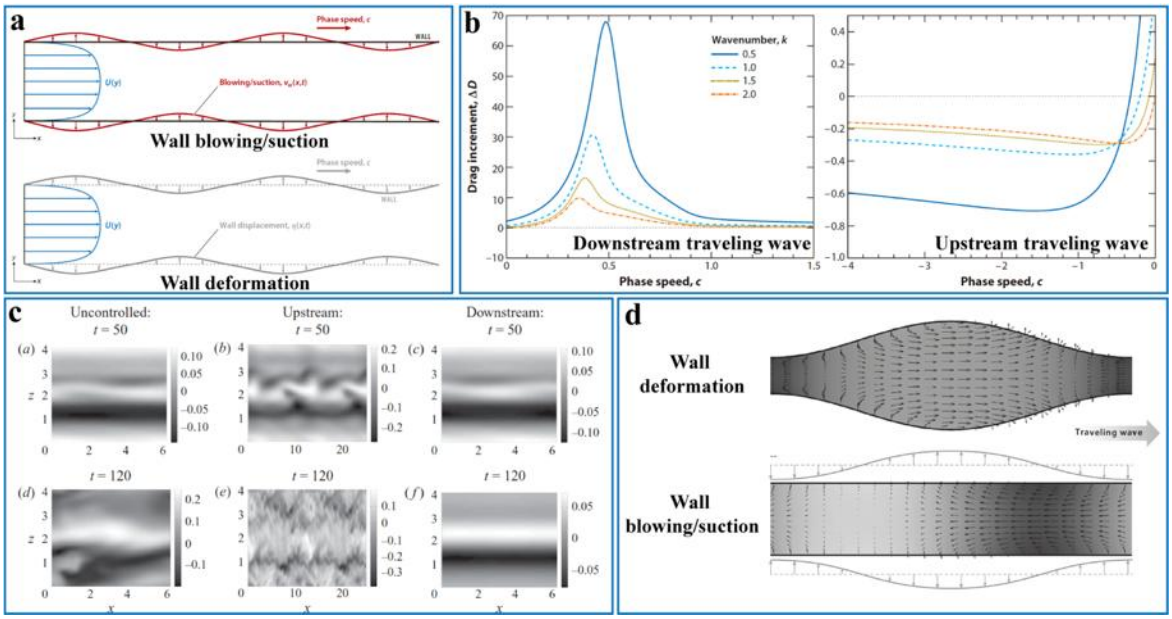

Figure 1-6 Turbulent drag reduction by streamwise traveling waves of wall-normal forcing

(a) Wall blowing/suction and wall deformation [65]; (b) Drag increment induced by wall blowing/suction [66]; (c) Comparison of streamwise velocity fluctuations between uncontrolled flow and controlled flow by wall blowing/suction [69]; (d) Pumping effect induced by wall deformation and wall blowing/suction [65].

that a steady flow rate can be maintained even with the pressure gradient eliminated. This demonstrates that the UTW of wall blowing/suction relies more on a thrust generation rather than a drag reduction. Although the pumping effect allows the upstream traveling wave to achieve some drag reduction, the UTWs are ineffectively for controlling the turbulence onset as they enhance receptivity to stochastic disturbances relative to the uncontrolled flow. The turbulence onset in a bypass transition is typically marked by the emergence of streamwise streaks and their eventual breakdown. Figure 1-6(c) shows the streamwise velocity fluctuations in the cases of the uncontrolled, UTW-induced and DTW-induced flows, respectively. Compared to the uncontrolled flow, the UTW-induced streak distortion appears before t=50 and a wide range of spatial scales emerges as time progresses. In contrast, the DTW effectively suppresses velocity fluctuations, capable of reducing the intensity of streaks and thus preserving the laminar [68,69]. Therefore, considering the impact of different traveling waves on flow and drag, in the UTWs case, drag reduction is primarily achieved

by the pumping effect brought by wall blowing/suction, but the flow will be destabilized. In the DTWs case, the pump effect has a negative effect on drag reduction. However, since the DTWs can stabilize the flow, when the drag reduction induced by the stabilization can offset the negative effect of pumping, drag reduction can also be achieved [65].

Although using wall blowing/suction to achieve the streamwise traveling wave is appealing due to its minimal reliance on extensive sensor systems, implementing devices to produce such a wave is technically challenging. A practical alternative is to replace the wall blowing/suction with wall deformation to form the traveling waves. As shown in figure 1-6(a), the wall deformation can be actuated by separately distributed generators. The shape of wall surface changes in this wall deformation case. The DTW-induced drag reduction effect in the form of wall deformation was firstly studied over half a century ago. Inspired by the swimming motion of fish, Taneda and Tomonari [71] established an experiment to investigate the development of boundary layer near a plate with waving motion like fish swimming and found an effect of relaminarization induced by the DTW when its wave speed is slightly higher than the external incoming flow ($c/U \approx 1.2$). Subsequently, Shen et al. utilized the DNS method to investigate the boundary flow and force distribution around a similar wavy wall and found the conclusions consistent with the results by Taneda and Tomonari. And the downstream traveling waves can reduce the total drag [71,72]. This shows some differences from the wall blowing/suction. Fukagata et al. have also explained the reasons for this difference in their review. As demonstrated in figure 1-6(d), the wall blowing/suction-induced pumping effect is opposite to the wave direction. In contrast, the effect caused by wall deformation aligns with the wave direction. Therefore, the UTW of wall blowing/suction drives the fluid to move along the flow direction, generating thrust and exhibiting drag reduction. However, the situation is exactly the opposite to the wall deformation. The positive pumping effect provided by the downstream traveling wall deformation, combined with the ability of DTWs to stabilize the flow, results in good drag reduction characteristics for the DTW of wall deformation [65]. There also exist many studies using body force/Lorentz forcing to add opposing momentum to achieve the “opposition control” [7,73]. In my opinion, the basic principle is the same as wall blowing/suction, only the method differs. However, most research of opposition control is based on numerical simulations regardless of the method, and there are still certain difficulties in practical

applications.

To achieve the attenuation of velocity fluctuations, the wall oscillation in spanwise direction is the most common method used in the research. Figure 1-7(a) displays the simplest actuated method by oscillating the whole wall in the spanwise direction purely as a function of time, following the equation:

$$W_m(t) = W_m \sin\left(\frac{2\pi t}{T}\right). \qquad (1-2)$$

The wall oscillation induces an unsteady spanwise shear layer – a "Stokes layer" – that can achieve the suppression of turbulent velocity fluctuations and reduction of the wall shear stress [7]. Under a fixed Reynolds number condition, the extent of drag reduction is determined by two forcing parameters W_m and T, which represent the wall velocity amplitude, and the oscillation period, respectively. Here, we give the non-dimensional forms of these two parameters, such as:

$$W_m^+ = \frac{W_m}{u_\tau} \text{ and } T^+ = \frac{T u_\tau^2}{\upsilon}, \qquad (1-3)$$

where u_τ is the friction velocity on the wall, ρ and υ are is the density and kinematic viscosity of the fluid, respectively. It is observed through several numerical and experimental studies that the drag reduction increases monotonically with W_m, but the effectiveness of drag reduction peaks when T^+ is approximately 100. Under this condition, the maximum drag reduction ratio is approximately 40% and the unsteady Stokes layer thickness is $y^+ = yu_\tau/\upsilon \approx 15-20$, which means that the strain in this unsteady Stokes layer is nearly limited to the viscous sublayer. With T^+ being larger than 100, this unsteady Stokes layer continues to develop, thus gradually penetrating the buffer layer and eventually influencing the fully turbulent layer. The influence of the Stokes layer extending beyond the viscous sublayer will increase the turbulence generation, thereby counteracting its drag reduction effects within the viscous sublayer, resulting in a weakened effect of drag reduction. As T^+ continues to increase beyond 400, drag reduction will not occur [7,74–77].

Figure 1-7(b) shows a more complex actuation form in which a streamwise traveling-wave pattern can be generated through the spanwise wall oscillation. Here, x, y and z in figure 1-7(b) denote the coordinates in the streamwise, wall normal, and spanwise direction, respectively. And this actuation can be described by:

$$W_m(x,t) = W_m \sin(\kappa_x x - \omega t). \qquad (1-4)$$

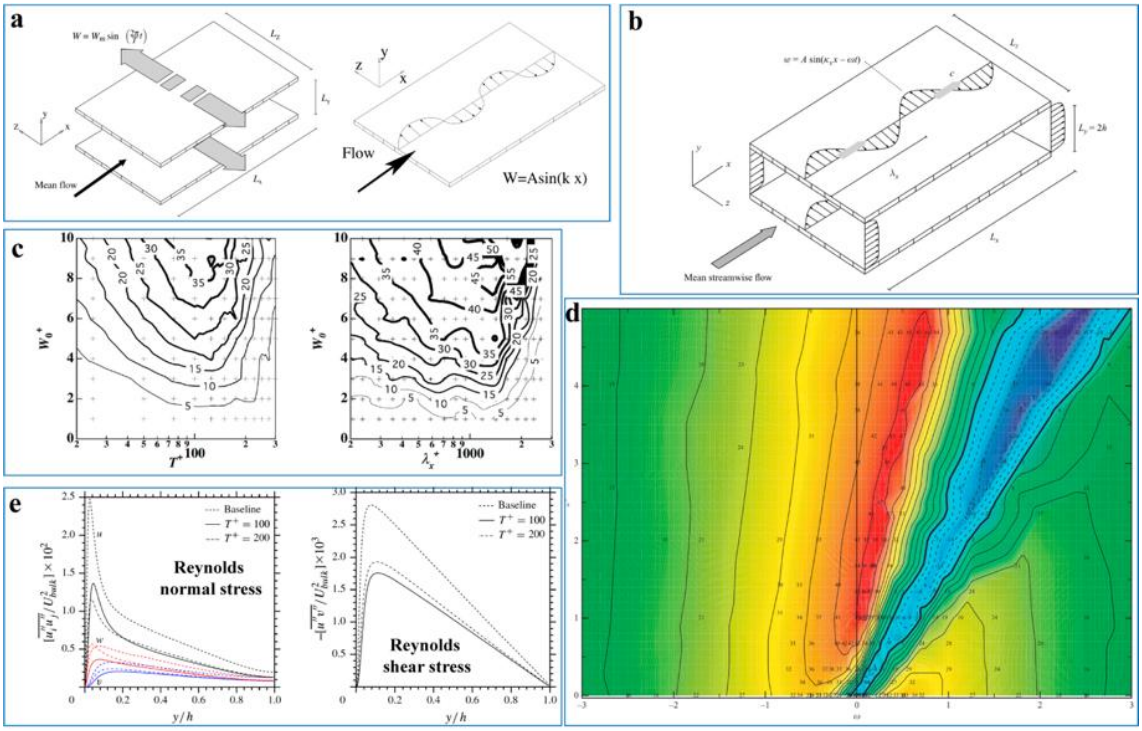

Figure 1-7 Spanwise wall oscillation-induced turbulent drag reduction

(a) Sketch of wall oscillation in purely temporal or spatial forcing [76,78]; (b) Wall motion involves streamwise-traveling waves of spanwise wall velocity [79]; (c) Drag reduction as a function of time period, wavelength and amplitude [80]; (d) Map of friction drag reduction in the $\omega - \kappa_x$ plane [79]; (e) Reduction of Reynolds stress induced by wall spanwise oscillation [81].

It is the simultaneous action of temporal ($\kappa_x = 0$) and spatial ($\omega = 0$) elements. In recent years, research on this combination type of forcing obtains more attention than those by purely temporal oscillations shown in figure 1-7(a) due to its superior drag reduction performance and flexibility, allowing for effective net power saving through parameter adjustment in equation (1-4). Due to the addition of wave propagation characteristics, in this case, the streamwise wavenumber $\kappa_x = 2\pi/\lambda_x$ where λ_x is the wavelength and the frequency ω play an important role on the drag reduction. The first investigation about the combination is provided by Quadrio et al. [79]. Prior to this, researchers conducted studies focusing separately on purely temporal and spatial forcing [74–80,82]. Figure 1-7(c) indicates the DNS simulations about drag reduction rate in temporally- and spatially- periodic controls for a channel flow under the condition of constant flow rate when Re_τ = 150. The maximum

drag reduction ratio is appropriately 35% when $T^+ \approx 100$ for the temporal element and is about 45% for spatial forcing when $\lambda_x^+ \approx 1000$. Obviously, the spatial control generally achieves better drag reduction effect than the temporal cases [80]. Although Viotti et al. [78] and Yakeno et al. [80] have demonstrated that the results from purely spatial control is largely analogous to the purely temporal oscillations, the flow response to the traveling waves becomes intriguingly complex when influenced by the combination of κ_x and ω. Both the reduction and increase of drag may be observed in the combination cases. The results shown in figure 1-7(d) are referred to as "Quadrio map", with data derived from DNS simulations over a channel flow conducted by Quadrio et al. under the fixed conditions of $Re_\tau = 200$ and $W_m^+ = 12$ but a variation in frequency and wavelength. Two regions with different effects can be seen in the contours. In the red zone, an intense drag reduction occurs. The maximum drag reduction rate in this region is about 48%, which is higher than that in the two pure single-condition oscillations. The situation of drag reduction being 47-48% corresponds to a wide range of κ_x. But in the blue region, the drag increases significantly up to 23%. This region is surrounded by two lines (thick black lines) with the meaning of zero drag reduction. The phase speed is constant ($c \approx 0.35$ and $c \approx 0.6$) in this space. It is noted that the significant drag increase appears in the case of forward-traveling waves, whereas conversely, the backward-traveling waves always lead to drag reduction at any wave speed [7,79].

Currently, there is no clear or widely accepted paradigm that can fully and convincingly explain the physical mechanisms behind drag reduction. Here, we briefly introduce the possible mechanisms of drag reduction based on the most common explanations in the literature, focusing on the near-wall turbulence statistics. From the perspective of velocity fluctuations, when spanwise oscillations induced by wall forcing occur, a significant velocity attenuation occurs in the wall-normal direction, indicating a substantial suppression of ejections and sweeps near the wall. There is also clear evidence shown in figure 1-7(e) that the spanwise oscillation reduces the Reynolds shear stress and turbulent kinetic energy in the boundary, contributing to reduce drag [81,83–87]. And from the perspective of vorticity fluctuations, the wall-normal component is linked to the intensity and the near-wall spanwise components is associated with the regeneration of the low-speed streaks. When the spanwise actuation is added, especially close to the optimal parameters, both spanwise and wall-normal vorticity correlation are attenuated, leading to a reduction in the intensity of the low-

speed streaks. Additionally, the streamwise components, which reflect the presence of quasi-streamwise vortices and the intensity of uplift ejections/sweeps corelated to the generation of low-speed streaks, also decrease. All the attenuations weaken the turbulent mixing in the boundary and contribute to drag reduction [7,81]. Of course, there are many other explanations [88–91], but the key point I think essentially boils down to the interaction between wall excitation and boundary flow in the near-wall region, suppressing turbulent production and controlling near-wall turbulent behavior to achieve reduction of drag.

Overall, current turbulent drag reduction methods focus more on achieving friction drag reduction. For fully developed turbulence, friction drag is not only dependent on the velocity gradient in the near-wall region according to Newton friction law but also to the Reynolds stress. Therefore, the turbulent drag reduction strategies may be categorized into two approaches: the first one is by direct reduction of near-wall velocity gradient; and the other one is by the attenuation of velocity fluctuations. In the drag reduction methods mentioned before, the superhydrophobic surfaces evidently apply the first strategy, while other methods are more related to the second strategy which involves controlling turbulent structures. Although turbulent drag reduction methods have seen significant development in recent decades, further technique breakthroughs for better drag reduction performance and engineering operability and applicability are still required.

1.3 DRAG STRATEGIES INSPIRED BY DOLPHINS

It has been a longstanding impression that dolphins swim with a low energy consumption. The earliest description about the dolphins' swimming ability comes from Aristotle, who wrote, "It [the dolphin] appears to be the fleetest of all animals, marine and terrestrial…" (*Historia Animalium*). In 1936, James Gray proposed the famous "Gray's paradox" that the calculating forces required to overcome fluid drag and maintain high speed appeared significantly greater than that generated by dolphin's muscle [92]. Thus, it is inferred that dolphins possess some special drag reduction mechanism enabling their high-speed swimming. This mechanism of high-speed swimming by dolphins continues to receive widespread attention as movement in water is considerably more challenging because of its higher density and viscosity compared to air [93,94]. Unveiling biological behaviors and

understanding mechanics of dolphin swimming may provide a theoretical and technical support for achieving drag reduction or high-speed navigation in surface or underwater vehicles.

1.3.1 Streamlined body shape

Streamlining is an important feature of dolphin as the drag on dolphin can be minimized primarily by the streamlined shape of the body and appendages. As shown in figure 1-8, the streamlined shape features a fusiform shape, resembling a typical feature with a rounded leading edge, a maximum thickness at the midpoint, and a gradually tapering tail. This streamlined shape was firstly studied in the dolphin by Sir George Cayley around 1800, being identified as a design with least resistance. The streamlined shape decreases drag by reducing the pressure difference across the body, enabling the boundary liquid to flow smoothly along the body surface without separating until it reaches the tail end [95,96].

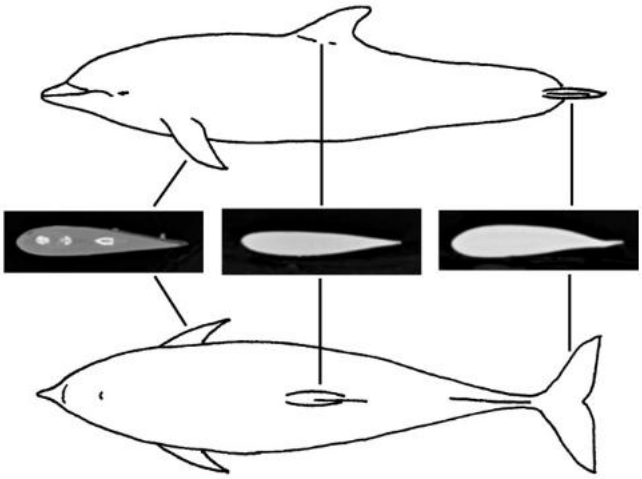

Figure 1-8 Streamlined shape of body and appendages of dolphin [96]

There is an indicator called the fineness ratio (*FR*), the rate between the body length and maximum diameter, used to describe the degree of streamlining. For rotating bodies, drag is minimized when *FR* is in the range of 3-7. Generally, dolphins usually have a *FR* value between 3.3 and 8.0 [95,96]. However, the fineness ratio is only a rough indicator of the streamlining degree because the shape variation of body cannot be shown by just *FR*. Therefore, another indicator (the position of maximum thickness, knows as the shoulder) are used to describe the streamlining. This position is crucial as it marks the point where the

flow transfers from laminar to turbulent and the potential separation position of the boundary layer. The pressure distribution before the shoulder is conducive to maintaining the laminar. In most high-speed swimming fishes, the shoulder position is shifted rearward, maintaining the laminar boundary flow and thereby reducing drag. The shoulder position of dolphin is typically located about 34-45% of the body length from the rostrum [95,96]. Although the streamlined body shape of dolphin is a key factor in reducing drag, experimental measurements base on dolphin-shaped model have shown that the drag under these model conditions is nine times greater than the actual drag experienced by dolphins [96–98]. Therefore, there are other factors that influence the hydrodynamic performance of dolphins.

1.3.2 Dolphin skin characteristics

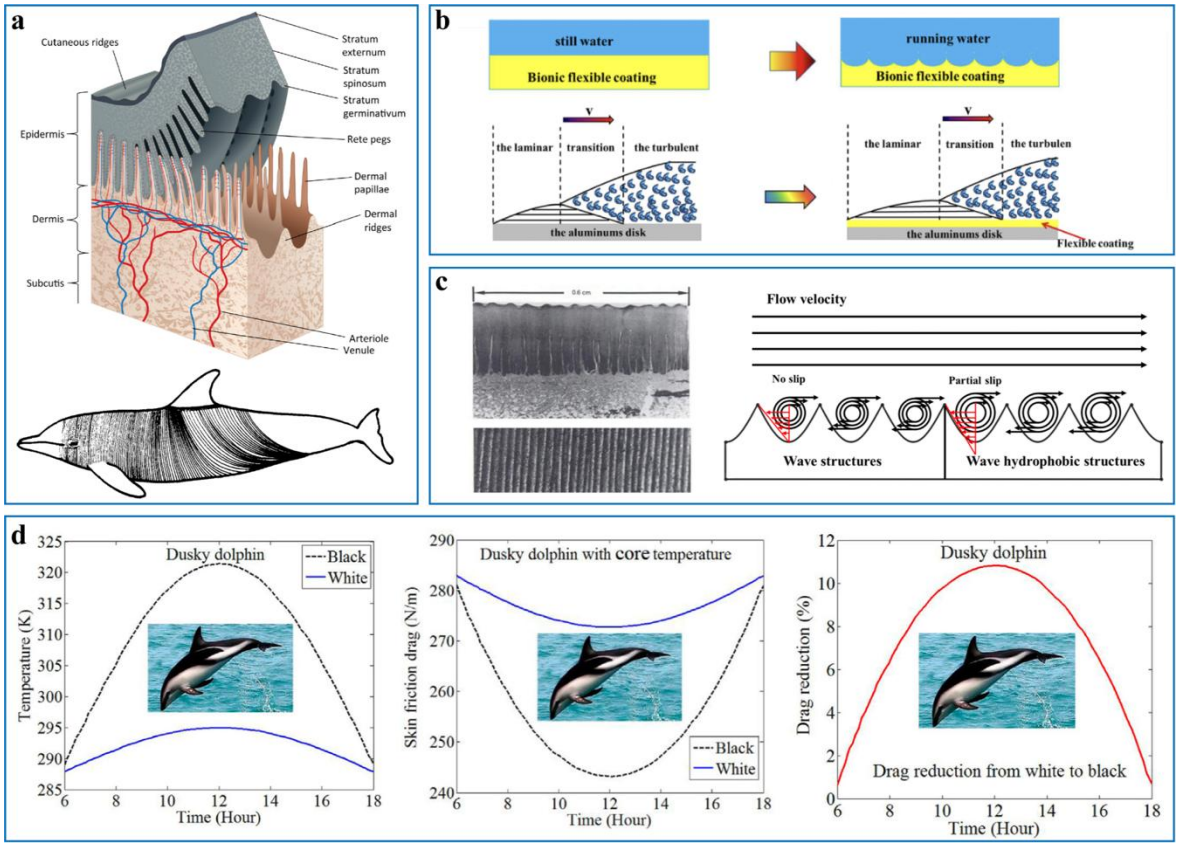

Figure 1-9 Dolphin skin characteristics

(a) The structure of dolphin skin [99,100]; (b) Dolphin-inspired bionic flexible coating [101,102]; (c) Near-wall vortices induced by the traveling wavy surface morphology on dolphin skin [103]; (d) Drag reduction caused by the skin temperature and color of dolphins [104].

The structure of dolphin skin can be divided into three layers: epidermis, dermis and subcutis, from the skin surface to the inside [figure 1-9(a)]. Most of the surface of the dolphin epidermis is covered with wavy, regular ridges known as cutaneous ridges. As indicated in figure 1-9(a), these ridges run almost perpendicular to the body's longitudinal axis, encircling the trunk in a circumferential pattern from the rostrum to the dorsal fin, but being absent in certain areas, such as most of the head and the region around the pectoral fins. In the area behind the dorsal fin, near the tail, the direction of these ridges changes and is oblique to the body axis laterally [99,100,105]. Beneath the epidermis lies the dermis, which can be divided into the papillary layer and the stratum reticulare layer. The papillary layer is adjacent to the basal layer of the epidermis, while the stratum reticular layer is much thicker and constitutes the main part of the dermis. The reticulare layer contains a lot of elastic fibers, giving the dolphin skin significant elasticity. The subcutis is located beneath the dermis, consisting of fat cells and collagen fiber bundles, commonly known as blubber. The fat tissue in the subcutis is very soft and highly deformable under external pressure [100].

1.3.2.1 Viscous damping

Based on the flexible and deformable characteristics of dolphin skin, Kramer proposed the drag reduction mechanism of viscous damping. He suggested that the compliant skin of dolphin can achieve the maintenance of a laminar boundary layer without separation, delaying the boundary layer transition and thereby achieving drag reduction. Moreover, Kramer designed a flexible rubber coating with the columnar structure. To address the issues of stress release and surface pressure waves in the columnar model, he further developed a ribbed and a multilayer homogeneous coating. These three types of compliant coating are all composed of three layers, with rubber of different elastic moduli simulating the epidermis, dermis and subcutis of dolphin from the outside to the inside. Kramer applied these rubber coating to a rigid towing body and conducted experiments by towing the body in river and seawater using a tugboat. The drag coefficients and the rate of drag reduction relative to the original rigid body are measured, showing a maximum drag reduction rate of 59% [106]. Although Kramer's research achieved promising results, it has been questioned by other researchers due to the difficulties in reproducing the experimental outcomes. And according to figure 1-9(a), the actual dolphin skin composition is highly organized and complex,

suggesting that the attempt with the rubber coating proposed by Kramer might be superficial and not functionally significant. Carpenter also argued in 2006 that the mechanical properties of Kramer's coating is ideal and would not exactly match those of dolphin skin, as Kramer used a towing speed of 18 m/s, which is twice the maximum swimming velocity typically assumed for dolphins [107]. In addition to the above theoretical doubts, experiments on drag reduction with compliant walls have shown variability, with some achieving limited success and others failing [107–110]. This demonstrates that there is still much to learn about the complex characteristics of dolphin skin. But it should be noticed that some bionic attempts based on the compliant wall have already achieved remarkable results. Li et al. applied a mixed solution of polydimethylsiloxane and ethyl acetate onto an aluminum plate. Heating the coated aluminum plate resulted in a bionic dolphin-inspired flexible coating. This flexible skin has been verified to achieve a 21.6% drag reduction effect [101]. They attribute the achievement of drag reduction to the viscoelastic properties of the coating itself. When a disk coated with this bionic flexible material moves in the water, the interaction between the coating and the water induces the wall deformation, generating the spanwise transversal traveling waves, as illustrated in figure 1-9(b). These deformations suppress fluid pressure fluctuations and highly absorb the turbulent kinetic energy. Additionally, the formation of these waves increases the thickness of boundary, providing some advantages to reduce the drag of the hull. The combined effect of these factors delays the transition of boundary layer from laminar to turbulent, thus achieving drag reduction [101,102].

1.3.2.2 Surface morphology

Dolphins are reported to be structured by shallow (less than 100 μm high) but regular cutaneous ridges, that cover most of their bodies [99,100,105]. These ridges are presented in a traveling wave pattern and are oriented perpendicular to the long axis of body [figure 1-9(a)]. These unique traveling wave grooves serve to mitigate the friction drag during cruising. Previous studies revealed that these traveling wave grooves can effectively reduce the friction drag. Under the influence of this structure, near-wall vortices are generated at the concave region of grooves and collided with the incoming flow, which has been substantiated through particle image velocimetry (PIV) and numerical simulation [103,111]. The top of these vortices aligns with the incoming flow direction, while the bottom near the

groove walls is opposite, resulting in a decrease in near-wall flow velocities, thereby reducing wall friction drag. Another perspective suggests that the presentence of such vortices is capable of converting the liquid/solid sliding friction on the wall into rolling friction, act as an effect called “rolling bearing”, thereby diminishing viscous resistance [figure 1-9(c)]. However, it is worth noting that the drag reduction effect of this stationary wavy wall is highly related to the shape of the waves. Only by appropriately designing the shape parameters according to the flow conditions can better drag reduction effects be induced [18,103].

1.3.2.3 Skin temperature and color

Many research have reported that the increase in temperature may lead to improved flow performance, such as delayed transition to turbulence and reduced vortex shedding [96]. Most notably, it results in a reduction of the skin drag. Li et al. demonstrated that a temperature increase of 20 °C in water can reduce the skin friction in turbulent flow basically by decreasing Reynolds shear stress in near-wall flow [112]. Peeters et al. reported that a temperature increase will contribute to decrease the density and viscosity of water, thereby suppressing vortices generation in the boundary, which in turn reduces the energy dissipation near the wall [113]. Based on the advantages of drag reduction brought about by skin temperature, some insightful scientists have begun to focus on the interaction between an organism’s skin color, skin temperature and drag resistance. Hassanalian et al. initially investigated the influence of different color (black and white) on skin drag reduction based on migrating birds’ wings. They found that the wing boundary layer with black-colored surface exhibits lower density and higher viscosity compared to those with a white-colored surface. This occurs because the wing surface temperature can be raised by the black color, correspondingly leading to decreased density and increased viscosity, but with an overall reduction in drag [114–117]. This different color distribution on skin surface is not only seen in bird wings but also in aquatic animals, such as the Killer whales and Dusky dolphins. Hassanalian et al. further conducted a study on Dusky dolphins, which exhibit distinct coloration with a black upper body and a white lower body. They calculated the changes in temperature, density and viscosity within the boundary layer over the body, as well as the resulting skin drag. As shown in figure 1-9(d), at midday the skin with black color on the

upper body reaches a temperature of 320 K, nearly 25 °C warmer than the white region. And due to the rise of temperature, the water density and viscosity in the near-wall region decrease, ultimately resulting in a skin friction drag reduction. Figure 1-9(d) highlights the drag reduction ability for the Dusky dolphins, showing that at midday, when the upper body is black, the skin drag can be decreased by up to 11% compared to the white region [104]. This also provide an explanation about why the fast marine animals have such a color scheme.

1.3.3 Secretions

The skin of a swimming dolphin generates a new layer of cells approximately every two hours, resulting in a relatively high rate of epidermal cell shedding. This shedding behavior of the dolphin's epidermal corneocytes also affects the wall shear stress. Nagamine et al. conducted direct numerical simulations on flexible surfaces covered with tiny particles, using the shedding of these particles to simulate the shedding of corneocytes from the dolphin's epidermis, aiming to explore the relationship between particle shedding and flow dynamics [118]. The results indicate that these shed cells can increase wall shear stress. However, the chemical and physical properties of dolphin skin and its high shedding rate effectively prevent dirt or other organisms from adhering to the dolphin skin surface, thereby maintaining its low-drag characteristics. Additionally, Uskowa et al. pointed out the presence of highly viscous secretions composed of proteins and polysaccharides around the dolphin' eyes [96]. Sokolov et al. suggested that these secretions do not affect the drag performance of dolphin [119], while Uskowa et al. argued that these ocular secretions can reduce water viscosity, thereby enhancing hydrodynamic performance. However, due to the limited coverage of these secretions, their overall impact on the dolphin's drag is not significant [96].

1.3.4 Adaptive surface drag reduction

The concept of adaptive drag reduction originates from further studies on the tissue structure of dolphin skin. The dermis of skin contains a lot of nerve bundles and capillaries, which enable the skin to sensitively detect variables in external flow field, such as fluctuations in pressure, velocity, and hydrodynamic load gradients [100]. This biological capability allows dolphins to dynamically alter their skin surface morphology in real-time, optimizing their adaptation to the current flow field and thereby achieving minimal drag. In

the case of viscous damping mentioned above, it relies on the material properties of the flexible surface. When water flows over a flexible surface, there is a potential for rich fluid-surface interaction, which can suppress inherent dynamic instabilities in boundary. Additionally, the deformation of the flexible surface allows for pressure release in the boundary layer, reducing flow resistance. However, this method of drag reduction is a passive one, where the flexible surface deforms in response to external flow conditions.

Adaptive surface drag reduction, on the other hand, differs in that it reflects a more active feedback control mechanism. It actively adjusts the surface shape based on the incoming flow conditions, making the material properties of the surface less critical. This approach collects flow fields information, employs specific control strategies and actuation methods, and more accurately controls the relevant flow field structures. It is applicable to different flow fields and can adjust in real-time to changing conditions, maintaining stable and effective drag reduction even in complex and variable flow environments [120–125]. For these reasons, adaptive drag reduction has gradually become a research hotspot both domestically and internationally. However, experimental research on adaptive drag reduction is currently limited by factors such as obtaining control signals and the design and manufacturing of micro-scale devices. As a result, most studies on adaptive control remain in the realm of numerical research.

1.4 RESEARCH CONTENTS AND SIGNIFICANCE

The current research on drag reduction methods and mechanisms reveals that whether it is the non-smooth drag reduction approach based on bionic shark skin surfaces or methods involving surface modification or bubble injection, all these techniques alter the near-wall flow structure through external intervention to achieve drag reduction. However, these approaches are unidirectional and have low inclusivity and applicability to different external flow conditions. In contrast, dolphins possess flexible skin that deforms according to varying external flow states. Although this is primarily a passive deformation relying on the viscoelastic properties of the skin surface, it reflects the interaction between the skin and the external flow field, providing new inspiration for the design of drag reduction method. However, existing studies indicate that the drag reduction mode based solely on the passive

deformation of dolphin skin cannot fully explain why dolphins exhibit such powerful hydrodynamic performance. The numerous capillaries and nerves within the dermis layer of dolphin skin suggest the possibility that dolphins actively regulate their skin dynamically in response to external flow fields, owing to their skin's sensitivity to these fields. Exploring this active regulation mechanism could help develop more adaptable artificial drag-reduction coatings to meet a wider range of engineering needs. Additionally, due to the deformability of dolphin skin, other biological behaviors exhibited by dolphins, such as echolocation and jumping, may also influence the state of their skin, thereby altering the near-wall flow structure to enhance hydrodynamic performance. Therefore, the drag reduction method relying on dolphin skin is complex, dynamic, and multifactorial, differing significantly from previous static drag reduction methods that relied solely on surface structure. The outstanding hydrodynamic performance and high adaptability to different flow fields demonstrated by this drag reduction method hold significant research value in both scientific and engineering fields.

Therefore, this study aims to further elucidate the complex, dynamic, and multifactorial drag reduction mechanisms of dolphins. We introduce a novel active control method inspired by dolphin skin to modify drag force through a longitudinal wave motion with ultrasonic oscillating frequencies and micro-size amplitudes. An integrated numerical analysis based on the skin motion are conducted to unveil the effect of the dynamic skin behavior on the boundary flow and drag distributions. Recognizing that dolphin's drag reduction is not the result of a single factor but rather the combined effect of multiple factors, we integrate the streamlined body shape and tail propulsion with the dynamic skin surface to jointly investigate the secrets behind the excellent hydrodynamic performance of dolphin. Main contents of the thesis include:

(1) A novel boundary layer and drag distribution induced by dynamic skin motion

Chapter 2 presents an integrated study of the turbulent flows passing a dynamic moving wall surface. Large-eddy simulations are performed to explore the dynamic motion-induced boundary flow and force distributions under different motion conditions. Chapter 3 provides a theoretical analysis of how dynamic skin motion affects the drag forces. A theoretical model for the dynamic boundary layer is established, further explaining the interaction between flow and drag in the near-wall boundary induced by wall motion.

(2) Hydrodynamic performance resulting from the combination of dynamic wall motion and streamlined body shape

Since dolphin drag reduction is the result of multiple factors working together, and its streamlined body shape is also a key factor in achieving its drag reduction, the streamlined body shape is considered in combination with the dynamic skin motion to explore their combined effects. Chapter 4 investigates this combined effect through the application of numerical simulations and provides different combination strategies for optimizing the drag reduction performance.

(3) The impact of dynamic skin motion on flow and drag during actual swimming

Chapter 5 examines the role of dynamic skin motion under the conditions of actual swimming, including tail-driven propulsion. With visualizations of overall and near-wall local flow structures around the dolphin body, the effective contribution of dynamic skin motion to propulsion during swimming is revealed, providing strong explanation for its long-distance and low-resistance swimming.

The key findings and conclusions, as well as the future work are summarized in Chapter 6. This work deepens the understanding of drag reduction mechanisms in dolphin swimming specifically in association with the dynamic skin wavy motion. The findings not only offer biological insights that could help resolve the mystery of Gray's paradox in relation to dolphin swimming but also provide a novel strategy for drag reduction technologies.

Chapter 2 TURBULENT DRAG REDUCTION USING DOLPHIN-INSPIRED DYNAMIC WALL MOTION

2.1 INTRODUCTION

Dolphins have always been an inspiration for research on drag reduction owing to their remarkable high-speed swimming and hydrodynamic performance. According to the investigation in Chapter 1 regarding dolphin's drag reduction strategies, the skin characteristics are considered to play a dominant role in reducing the friction drag on skin, acting as both a passive method in delaying the laminar-turbulent transition due to the skin's compliance and applying active control through skin surface oscillations. Microvibrations on the skin of warm-blooded animals, invisible to the human eye, have been studied extensively since 1960s [126]. In 1964, Haider and Lindsley used a special piezo-electric transducer to measure the behaviors on a female bottle-nosed dolphin skin (*Tursiops truncatus*), recording the presence of microvibrations on the skin surface [126]. Figure 2-1(a) shows sample records of microvibrations from a dolphin when it is out of water and swimming in water, revealing the amplitude of dolphin microvibrations is 3 to 4 times larger than that of human (1~5 μm). The presence of these microvibrations suggests in itself that the dolphin skin may not be static but dynamic during swimming. In addition, Ridgway et al. observed that dolphin skin can response to the applied stimuli and found that dolphin skin is highly sensitive to the vibrations or small pressure changes acted on its surface [99]. As a result, dolphin can response to the stimulations acted on it [figure 2-1(b)] and be very prone to deformation or oscillation due to its high sensitivity and flexibility. All these findings above suggest that there may exist a dynamic skin boundary during dolphin cruising.

There may be many possible stimulations due to dolphin's own behaviors and complex flow flied environment. Here we focus on a possible internal stimulus derived from the acoustic behaviors of dolphins. Dolphins can emit a series of high-directional, ultrasonic click signals for hunting and echolocation from its melon [127–133]. And it is worth noting that

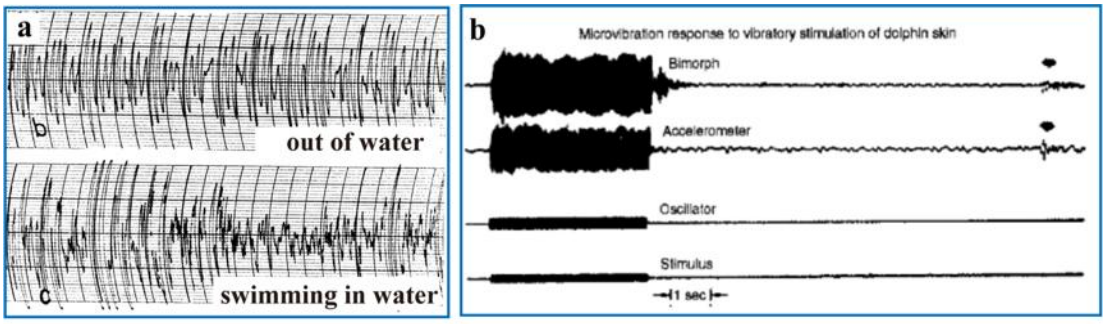

Figure 2-1 Dynamic behaviors of dolphin skin

(a) Microvibrations on dolphin skin (137); (b) Microvibration response to vibration stimulation of dolphin skin (110)

the skin near the melon is very sensitive [99,134]. Therefore, motivated by the microvibrations and high sensitivity of dolphin skin, we hereby hypothesize that the ultrasonic click signals with high intensity may act as an internal excitation to drive ultrasonic oscillations on the compliant skin during dolphin swimming. These oscillations produce a longitudinal traveling wave on the skin surface, herein termed as longitudinal micro-ultrasonic waves (LMUWs), with ultrasonic oscillating frequencies and micro-size amplitudes, as shown in figure 2-2. The dynamic boundary phenomena induced by the skin oscillation inspire us with insights to explore a novel active turbulent control strategy and drag reduction mechanisms while unveiling the mystery in dolphin swimming.

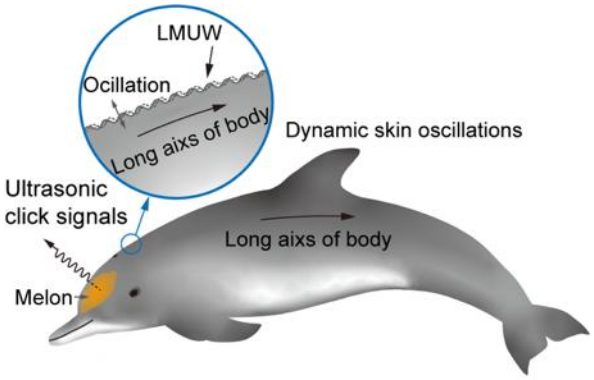

Figure 2-2 Dynamic skin oscillations in the form of LMUW

In addition, it is noteworthy that these microstructures on dolphin skin are oriented perpendicular to the body's long axis, which is the direction of dolphin swimming. This

orientation means that these skin ridges can create resistance to downstream flow, resulting in not only friction-based resistance but also the shape-induced pressure drag. In order to achieve an overall drag reduction on the skin, it is necessary not only to reduce the friction drag but also to ensure that this reduction compensates for the pressure drag caused by the shape. This suggests that achieving drag reduction through skin surface adaptations might be more challenging for dolphins compared to sharks, whose skin features longitudinal microgrooves with ridges aligned parallel to the swimming direction [135]. Despite this, even though the unique structure of dolphin skin leads to pressure drag, introducing an additional factor that affects total drag, the dolphin's remarkable hydrodynamic performance in high-speed, low-drag swimming, which rivals that of sharks, raises an intriguing question: what role does the shaped-induced pressure drag play in the dynamic boundary layer induced by skin oscillation?

In this chapter, we aim to explore the novel boundary flow and corresponding drag distribution induced by the LMUW wall motion and investigate the impact of the original skin friction and shape-induced pressure drag on overall total resistance in the dynamic boundary layer. A conceptual physical model of an open channel in which a portion of the bottom wall undulates to produce LMUWs is designed. Large-eddy simulations (LES) of the LMUW-altered turbulent flow are performed with three motion modes, comprising a standing wave and two traveling waves (downstream and upstream) in the streamwise direction. The overall flow and local flow details near the dynamic wall under different motion conditions are presented. And a comprehensive analysis is conducted on the correlation between the boundary flow and drag distribution acting on the moving wall.

2.2 DYNAMIC WALL MOTION MODEL

2.2.1 Open channel model with a LMUW-induced wavy wall

We consider the three-dimensional (3D) incompressible turbulent flow in an open channel over a partially LMUW-induced undulating wall (wavy motion). As illustrated in figure 2-3, the coordinate system (x, y, z) is defined such that x, y, and z denote the streamwise, vertical (normal to the wall), and spanwise coordinates, respectively. The wall

wavy motion is confined to the rear half of the open channel (0.82L, 0.88L) with an undulation region length of L_{uw}, where the wall-normal wavy motion is given in the form of two traveling waves (downstream and upstream) in the streamwise direction and a standing wave. The LMUW-induced undulating wall for traveling waves is defined as:

$$y_{w-tr} = a\sin[k(x-ct)]\,, \qquad (2-1)$$

and that for standing waves is expressed as:

$$y_{w-st} = a\sin(kx)\cos(2\pi ft), \qquad (2-2)$$

where a is the amplitude of the LMUW, λ is the wavelength, $k = 2\pi/\lambda$ is the wavenumber, f is the undulating frequency, and $c = \lambda f$ is the speed of the traveling waves. The propagation direction of the traveling wave is distinguished by the sign of c: the upstream traveling LMUW (c<0) propagates in the direction opposite to the external flow U, whereas for c>0, the wave propagates in the same direction as U, corresponding to the downstream traveling LMUW. The subscripts of *tr* and *st* represent traveling and standing waves, respectively. Hence, three velocity components (u, v, w) of the LMUW-induced wall are given as,

$$\left.\begin{array}{c} u_w = 0 \\ v_{w-tr} = (-kca)\cos[k(x-ct)] \\ v_{w-st} = (-2\pi fa)\sin(kx)\sin(2\pi ft) \\ w_w = 0 \end{array}\right\}. \qquad (2-3)$$

Inspired by the swimming performance of dolphins, the undulating frequency of the LMUW-induced wavy wall motion is set to the peak frequency of dolphin click signals, *i.e.*, f =100 kHz [127–133]. The freestream incoming flow has a velocity of U = 12.5 m/s, corresponding to a representative Re at which young dolphins perform a low swimming speed [104]. A low-frequency and large-amplitude traveling wave is often observed in fish swimming, allowing them to achieve a minimum power input at a specific condition of c/U = 1.2 for a fixed U [72,136]. Thus, we can calculate the traveling speed of the LMUWs to be 15.0 m/s, and hence the wavelength λ = 150 μm. The amplitude of the wavy wall motion is taken as 20 μm, based on the measurements of microvibration amplitudes on dolphin skin [126]. Given the inflow velocity U and the channel length L, the Reynolds number, $Re = UL/\upsilon$ (where υ is the kinematic viscosity of water, 1.0048×10^{-6} m^2s^{-1}) is calculated to be 1.24×10^6. This is identical to a low-speed swimming case (1.0 m/s) of a dolphin with a body length of 1.3 m, corresponding to a characteristic $Re_c = U\lambda/\upsilon$ for LMUWs of around 1900. The flow velocity U corresponds to that of the acceleration phase of dolphins, whereas the top cruising

speed may be up to 12.5 m/s [104,107]. The Strouhal number $St = 2fa/U$ is calculated as 0.32, falling perfectly within the range observed in swimming fish [136]. Furthermore, the Mach number $Ma = V_w/V_{sound}$ is calculated to be 0.0083 based on the peak normal velocity ($V_w = kca$ or $2\pi fa$) of the wavy wall motion and the speed of sound in water (V_{sound} = 1500 ms^{-1}). This is much less than 0.3, indicating that the fluid compressibility due to the ultrasonic vibration and wall forcing on the fluid flow can be neglected, confirming that the flow field is incompressible.

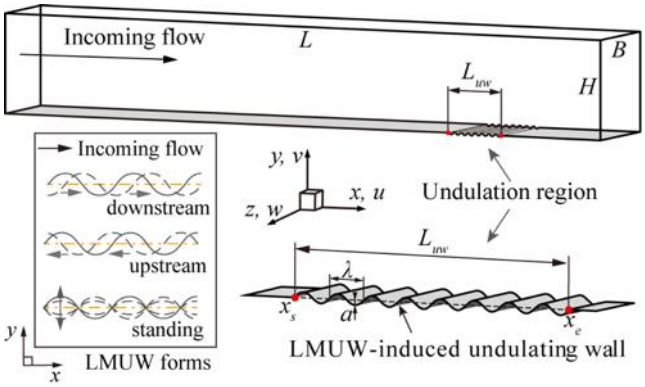

Figure 2-3 Schematic of turbulent flow over a partially undulating wall

2.2.2 Three-dimensional LES modeling

The governing equations for unsteady and incompressible viscous flow include the continuity equation, which follows the mass conservation,

$$\frac{\partial u_i}{\partial x_i} = 0, \qquad (2-4)$$

and the momentum equation, which follows the momentum conservation,

$$\frac{\partial u_i}{\partial t} + \frac{\partial (u_i u_j)}{\partial x_j} = -\frac{1}{\rho}\frac{\partial p}{\partial x_i} + \frac{\partial}{\partial x_j}\left[\upsilon\left(\frac{\partial u_i}{\partial x_j} + \frac{\partial u_j}{\partial x_i}\right)\right], \qquad (2-5)$$

where ρ is the fluid density, u is the velocity, p is the pressure, and υ is the kinematic viscosity. Flows can be governed by these partial differential equations, which, except for some special cases, cannot be solved analytically. To approximate solutions numerically, researchers employ a discretization method that transforms these differential equations into a series of algebraic equations, making them solvable on a computer [137]. The field of solving the flow governing equations on a computer using the numerical techniques to predict the flow behavior is known as computational fluid dynamics (CFD). ANSYS Fluent is a commonly

used commercial CFD software, widely applied in the research of fluid flow. And the model of large eddy simulation (LES) is one of the common turbulent models in CFD. Turbulent flows are characterized by eddies spanning a wide range of length and time scales. The large-scale motions are significantly more energetic than the small-scale ones and are the primary contributors to the transport of conserved properties due to their size and strength. In contrast, the small-scale motions are relatively weaker and contribute minimally to this transport [137]. As a result, LES focuses on accurately resolving the large eddies while modeling the small ones, making it a cost-effective and efficient approach for high *Re* flows or those involving complex geometries. In the LES modeling, large eddies are resolved by directly solving the Navier-Stokes (N-S) equation [equation (2-5)] while the unresolved/filtered small eddies are modeled by a subgrid-scale model. Various subgrid-scale models are available to be selected in Fluent, and here we select the wall-adapting local eddy-viscosity (WALE) model, which performs well in handling wall boundary layer flows and can effectively capture flow characteristics near the wall [138]. The filtered continuity and N-S equations in LES can be written in the form:

$$\frac{\partial \overline{u_\iota}}{\partial x_i} = 0, \tag{2-6}$$

$$\frac{\partial \overline{u_\iota}}{\partial t} + \frac{\partial \left(\overline{u_\iota}\overline{u_\jmath}\right)}{\partial x_j} = -\frac{1}{\rho}\frac{\partial \bar{p}}{\partial x_i} + \frac{\partial}{\partial x_j}\left[\upsilon\left(\frac{\partial \overline{u_\iota}}{\partial x_j} + \frac{\partial \overline{u_\jmath}}{\partial x_i}\right)\right] - \frac{\partial \tau_{ij}}{\partial x_j}, \tag{2-7}$$

where τ_{ij} is the subgrid-scale stress which can be defined by

$$\tau_{ij} = \overline{u_\iota u_\jmath} - \overline{u_\iota}\,\overline{u_\jmath}. \tag{2-8}$$

This unknow stress term is then modeled by the eddy-viscosity assumption, expressed as

$$\tau_{ij} - \frac{\delta_{ij}}{3}\tau_{kk} = -2\upsilon_t \overline{S_{\iota\jmath}}, \tag{2-9}$$

where υ_t is the turbulent eddy viscosity given by the WALE subgrid-scale model. $\overline{S_{\iota\jmath}}$ is the rate-of-strain tensor of the resolved field, defined as

$$\overline{S_{\iota\jmath}} = \frac{1}{2}\left(\frac{\partial \overline{u_\iota}}{\partial x_j} + \frac{\partial \overline{u_\jmath}}{\partial x_i}\right). \tag{2-10}$$

The eddy viscosity υ_t is given by

$$\upsilon_t = (C_w\Delta)^2 \frac{\left(S_{ij}^d S_{ij}^d\right)^{3/2}}{\left(\bar{S}_{ij}\bar{S}_{ij}\right)^{5/2} + \left(S_{ij}^d S_{ij}^d\right)^{5/4}}, \tag{2-11}$$

where S_{ij}^{d} denotes the traceless symmetric part of the square of the velocity gradient tensor, defined as

$$S_{ij}^{d} = \frac{1}{2}\left(\bar{g}_{ij}^{2} + \bar{g}_{ji}^{2}\right) - \frac{1}{3}\delta_{ij}\bar{g}_{kk}^{2}. \qquad (2-12)$$

Here, $\bar{g}_{ij}^{2} = \bar{g}_{ik}\bar{g}_{kj}$ and $\bar{g}_{ij} = \partial\overline{u_i}/\partial x_j$ represent the velocity gradient tensors (148).

In this study, to ensure a sufficient resolution of the multiscale eddy motion induced by the wavy wall, we employed LES-based modeling to resolve the fully developed open-channel turbulent flow over a computational domain of L (100 mm, streamwise) × H (20 mm, vertical-normal) × B (=L_{uw}, 6 mm, spanwise) using the ANSYS Fluent 16.0 commercial software (ANSYS, Inc.). The pressure-velocity coupling (SIMPLEC) algorithm was used to solve the incompressible N-S equations, and the least squares cell-based scheme was adopted to solve the variables gradients. The bounded central differencing and second order implicit schemes were respectively employed to discretize the momentum and transient formulations, which can bring some advantages on simulation stability and numerical dissipation reduction. The subgrid-scale model constant (C_w) was set to 0.325. As indicated in figure 2-3, the inlet and outlet boundaries are placed at distances of 13.7L_{uw} and 2.0L_{uw} from the undulation region, respectively; the upper boundary is 3.3L_{uw} away from the bottom wall surface. As discussed in the following sections, the LMUWs excite microvibrations with a maximum amplitude of 20 μm, which is on the order of L_{uw}/300, so the placement of the boundaries is reasonable for the numerical convergence and accuracy of the simulations. The constant mass-flow rate condition is imposed at the given *Re* by applying a freestream velocity at the inlet, free outflow condition at the outlet, no-slip condition on the wall, free-slip condition at the upper boundary, and periodic boundary condition at both spanwise boundaries.

Simulations were first conducted in the open channel with a flat bottom wall to obtain a fully developed turbulent flow over the undulation region. The LES framework was then applied with the undulation region excited by the LMUWs in the form of two traveling waves (downstream and upstream) in the streamwise direction and a standing wave. The normal wavy motion of the undulation region can be defined at a coordinate x and time t for a traveling wave in the form:

$$y_w = F(x)a\sin[k(x-ct)]G(t), \qquad (2-13)$$

where $F(x)$ is introduced to ensure a smoothly deforming wall undulation adjacent to the

non-undulating region, given in the form of $F(x) = 1\text{-}\exp[(x_s\text{-}x)/\lambda]$ at the start point [$F(x) = 0$ at x_s] and $F(x) = 1\text{-}\exp[(x\text{-}x_e)/\lambda]$ at the end point [$F(x) = 0$ at x_e] of the undulation region (figure 2-3). This function is very close to 1 after five wavelength cycles. The function $G(t)$ is used to ensure the transition from the initial flat wall to the undulating wavy wall smoothly: $G(t) = 1\text{-}\exp[-(2ft)^2]$, *i.e.*, $G(t) = 0$ at $t = 0$ and approaches 1 as t increases. The dynamic mesh model in Fluent was employed to update the computational grids due to the wavy wall motion with a time step of $T/100$, which was confirmed to be sufficient to ensure the smooth regridding of the computational domain. And the time step has also been verified to satisfy the Courant Friedrichs-Lewy condition (i.e., CFL<1) for accurate resolution of the instantaneous flows around the models. All LES simulations run included up to 20 undulating cycles as the flow converged to stable fully developed turbulence. And the flow and force distributions usually exhibit stable periodic variations after five cycles, and the instantaneous flow variables after the flow becomes periodically stable are used for the analysis of near-wall flow and drag force.

2.2.3 Mesh verification and validation

A structured grid system was employed, with grids clustered to the undulating wavy wall in the streamwise direction and to the wall surface in the vertical direction. Two grid resolutions were tested to confirm the independence of the results with respect to the grid of a basic grid system with 600 (streamwise) × 61 (spanwise) × 100 (vertical) cells and a fine grid system with 900 (streamwise) × 76 (spanwise) × 100 (vertical) cells. In the undulating region, the grids were densely and evenly distributed with 400 cells in the basic grid system and 600 cells in the fine grid system in streamwise direction, respectively. Evenly spaced grids were distributed in the spanwise direction. The height of first mesh layer adjacent to the wall surface was set as 0.002 mm, meeting the requirement of the dimensionless wall distance, $y^+ = u^* y/\upsilon \approx 1$, where u^* denotes the friction velocity, y is the distance to the wall surface, and υ is the local kinematic viscosity of the fluid.

The grid-independence was verified by comparing the total drag coefficient (C_d), defined by

$$C_d = \frac{F_f + F_p}{0.5\rho U^2 S}, \qquad (2-14)$$

where F_f and F_p are the friction drag and pressure drag, respectively, S is the undulation region area, U is the freestream velocity, and ρ is the density of water. The friction (C_f) and pressure (C_p) drag coefficients are respectively defined by

$$C_f = \frac{F_f}{0.5\rho U^2 S} \text{ and } C_p = \frac{F_p}{0.5\rho U^2 S}, \qquad (2-15)$$

As shown in figure 2-4(a), the C_d is almost independent of the grid resolution over a complete undulating cycle, with a marginal difference of 1.8% in the time-averaged total drag coefficient (C_D) between the basic and fine grids.

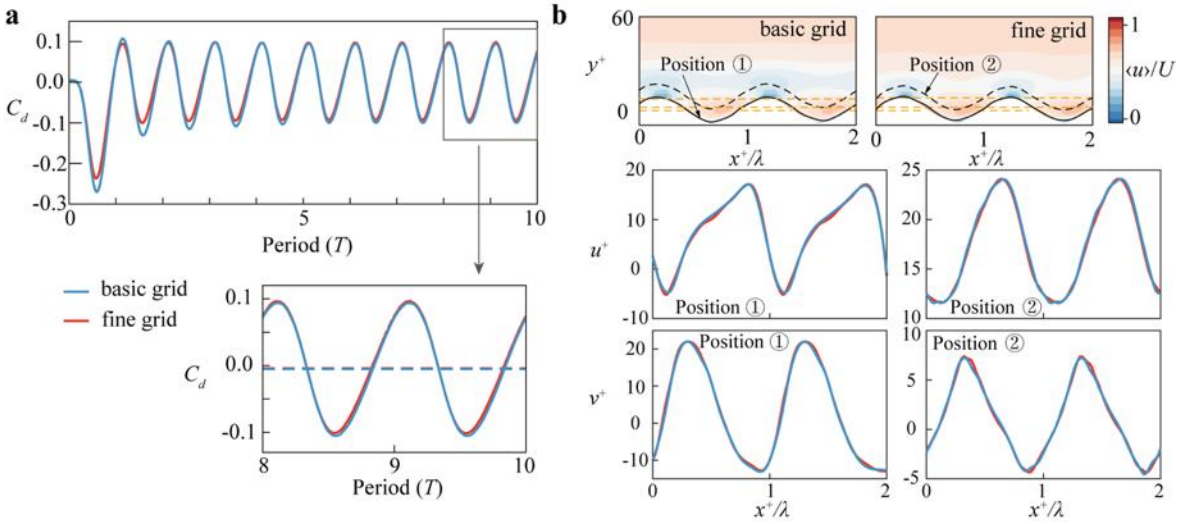

Figure 2-4 Mesh verification

(a) Mesh independence in terms of total drag; (b) Comparison of near-wall velocity distributions

The near-wall velocity contours on wavy wall (on x-y plane at $z = B/2$) and streamwise velocity (u) and vertical velocity (v) distributions at two different positions under downstream traveling LMUW at $0T$ are also compared in figure 2-4(b) for the two grids. Position 1 (solid lines) and Position 2 (dashed lines) respectively represent the distance of $0.2a$ and a from the undulating wall. $\langle u \rangle$ is the velocity magnitude given by $\langle u \rangle = \sqrt{u^2 + v^2 + w^2}$; the streamwise and vertical coordinates are normalized by $x^+ = [(x-x_s)/L_{uw}+n\lambda]$ and $y^+ = u_{ref}^* y/\upsilon$, where n is an integer and u_{ref}^* denotes the friction velocity of flat plate, u and v are normalized by $u^+ = u/u_{ref}^*$ and $v^+ = v/u_{ref}^*$, respectively. The results show a good consistency between the two grids. Thus, the basic grid system was adopted in all subsequent simulations, considering the balance between numerical accuracy and

computing time.

The LES formulation was further validated by comparing the measurements obtained from a conceptual physical model in association with the wall-bounded turbulent flows around a flexible membrane at $Re = 1.1\times10^5$, $St = 0.22$ when forced to undulate in the form of a streamwise traveling wave in a water channel [139]. With the same grid system, boundary condition settings, and flow conditions ($c/U = 1.2$) as in the open channel simulations, the velocity distributions in the vicinity of the moving wall surface given by the computational (lines) and experimental (dots) schemes are in good consistency, as depicted in figure 2-5. This indicates that the LES formulation can accurately capture the wall-bounded turbulent flow structures actuated by streamwise traveling waves.

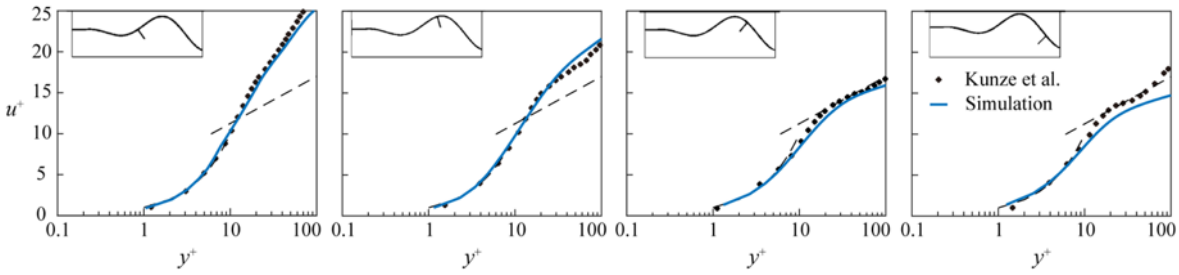

Figure 2-5 Validation through a comparison of velocity profiles obtained in simulations and experiments

2.2.4 LMUW-induced near-wall flow structures

The boundary flow fields actuated by three LMUWs are visualized in the near-wall region in figure 2-6. Obviously, the normal microscale vibrations actuated by the LMUW-induced wavy motion excites micro-normal forcing onto the wavy wall surface. These have a significant impact on the velocity fluctuations, which are primarily confined to the viscous sublayer of the turbulent boundary layer. This occurs in all three LMUM motions and is clearly distinguishable from the near-wall laminar flow separation or turbulent fluctuations observed in conventional wavy motion-excited flow fields in terms of the low-frequency and large-amplitude oscillatory strategies in association with active flow control methods [65,140] and biological swimming and flight [136,141]. Importantly, the impact of these LMUWs on the dynamic boundary flow [figure 2-6(b-d)] is restricted to the undulation region, barely altering the wall-bounded turbulent flow outside of this region. This indicates that LMUW-based active flow control could provide a straightforward and effective method of actively

manipulating the local microscale shear flow and velocity fluctuations adjacent to the wall surface without exerting any significant influence on the surrounding macroscale flow fields.

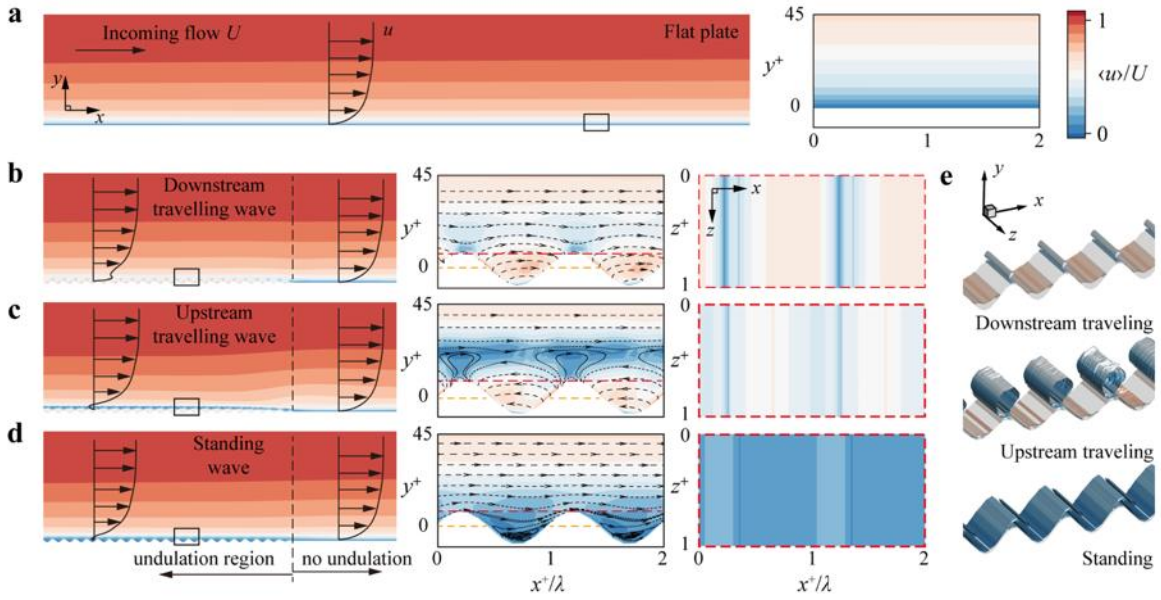

Figure 2-6 LMUW-induced near-wall flow structures

(a) Flat plate without wavy motion; (b) Downstream traveling LMUW; (c) Upstream traveling LMUW; (d) Standing LMUW; (e) Regular transverse roller-like flow structures induced by LMUWs

The turbulent fluctuations are characterized by a novel dynamic boundary layer that is significantly different from the conventional dynamic Stokes layer [7]. Figure 2-6(b-d) indicates the streamwise velocity vectors and contours adjacent to wavy wall surface actuated by the three LMUWs at 0T in a magnified view on the x-y plane in mid-span and the x-z plane at y=a (wave peak, red dashed lines). Here z coordinate is normalized by the length of undulation region, defined as z^+=z/L_{uw}. These fluctuations produce a multilayer eddy motion in the low-viscosity sublayer of less than approximately four wave amplitudes (4a, or $y^+ < 30$) in the vertical (normal) direction, a periodic eddy motion in the streamwise direction, and a marginal secondary flow in the spanwise direction. The traveling wave-excited normal forcing obviously plays a dominant role in altering the multi-eddy motion, and thereby the velocity fluctuations: the downstream traveling wave ($c > 0$) results in a downstream flow, and thus an enhanced velocity gradient [figure 2-6(b)], while the upstream traveling wave ($c < 0$) induces an upstream flow, i.e., a reversed velocity against the

streamwise flow [figure 2-6(c)] at the trough of the wavy wall. The vertical velocity profiles in association with traveling waves remain unchanged over a cycle, with only variations in phase. The standing wave lacks any propagative nature but leads to variations in wall shape over an undulating cycle: the alterations in the near-wall flow are induced by the time-varying wall configuration, presenting more complicated features [figure 2-6(d)]. As indicated in figure 2-6(e), a two-dimensional feature of transverse roller-like flow structures appears in all three motion modes, which is visualized by iso-surface of the Q-criterion of 1×10^9 with colors corresponding to the velocity magnitude contours. The presence of roller-like structures indicates that the actively controlled LMUW-excited wall motions can regularize the near-wall dynamic boundary flow, resulting in a similar flow structure to stable relaminarization [142].

2.2.5 Drag reduction mechanisms

The LMUW-actuation alters the velocity fluctuations remarkably within the viscous sublayer, thereby manipulating the friction-drag variation, which is highly associated with the LMUW mode. Here, we introduce a friction-drag reduction rate (DR_{FD}) and a total-drag reduction rate (DR_D), where the rate of drag reduction can be defined as $DR=(C_{\text{plate}}-C)/C_{\text{plate}}$, and compare the time-averaged coefficients of friction drag ($C_F = \int_0^T C_f \mathrm{d}t/T$), pressure drag ($C_P = \int_0^T C_p \mathrm{d}t/T$), and total drag ($C_D = \int_0^T C_d \mathrm{d}t/T$) among the three wavy motion walls and flat plate wall in table 2-1. The upstream traveling wave enables a significant reduction in the wall shear, eventually resulting in a reversed wall shear and negative friction drag, i.e., a thrust (DR_{FD} = 8.62). The downstream traveling wave enhances the wall shear, thereby producing increased friction drag (DR_{FD} = -6.76), as commonly observed in the undulating swimming of aquatic animals [136,143]. The standing wave generates transient variations in the wavy wall configuration during an undulating cycle, inducing vortical and reversed flows adjacent to the trough wall [figure 2-6(d)], as also detected in the case of the static wavy wall [72], resulting in a time-varying wall shear alteration that is capable of reducing the friction drag (DR_{FD} = 0.95).

The time-varying wavy configuration of the undulating wall also generates pressure drag (table 2-1 and figure 2-7), which depends on the LMUW mode, but displays different features than the friction drag. There exists a tradeoff in drag reduction between friction- and

pressure-based drag: contrary to the friction drag, the pressure-based drag is greatly reduced in the case of the downstream traveling wave, and eventually becomes negative, i.e., a thrust; however, the pressure drag is significantly increased under the upstream traveling wave and shows a slight increase with the standing wave. Interestingly, the variation in the pressure drag corresponds precisely to the complexity of the multi-eddy motion induced by the LMUW motion. As depicted in figure 2-6(b-e), the dynamic boundary layer is highly correlated with the LMUW mode, resulting in significant variations in flow fields: the downstream traveling wave ($c > 0$) generates a downstream flow [figure 2-6(b)], resulting in a pressure-based thrust; the upstream traveling wave ($c < 0$) produces a reversed upstream flow [figure 2-6(c)], hence enhancing the pressure-based drag; and the standing wave shows a moderate pressure drag compared to the traveling waves.

Table 2-1 Drag coefficients and drag reduction rates associated with LMUW-actuated undulating wall

	C_P	C_F	C_D	DR_{FD}	DR_D
Plate	0	0.0019941	0.0019941	-	-
Downstream	−0.0191917	0.0154825	−0.0037092	−6.76	2.86
Upstream	0.0388282	−0.0151944	0.0236338	8.62	−10.85
Standing	0.0073387	0.0000961	0.0074348	0.95	−2.73

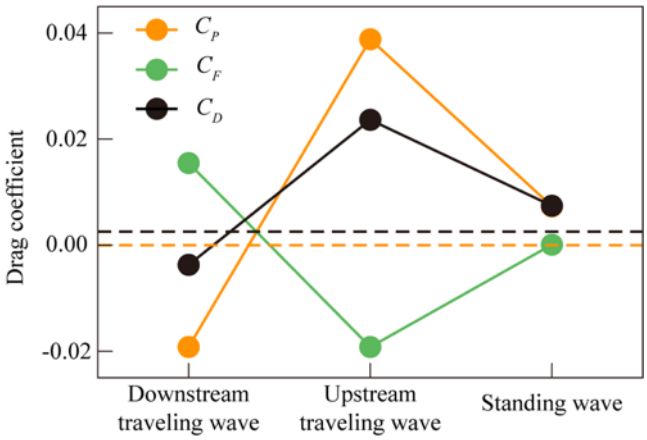

Figure 2-7 Comparison of drag coefficients acting on LMUW-actuated undulating wall

2.3 A LMUW-INDUCED NOVEL DYNAMIC BOUNDARY

Due to the movement of dynamic undulating wall, the fluid near the wall changes accordingly, inducing a dynamic boundary layer different from that of a flat plate boundary.

In section 2.2, we observed the LMUW-induced boundary layer and its great potential in drag reduction under specific oscillation frequency condition (f=100 kHz). Considering that such high-frequency, micro-scale amplitude wall oscillations only affect the near-wall region without influencing the overall flow field, we specifically focus on the variations in the dynamic boundary layer and establish a computational model that concentrates solely on the oscillating wall surface and its immediate surroundings to investigate the details of flow characteristics in the dynamic boundary layer under different oscillation conditions.

2.3.1 Simulation model for details of dynamic boundary

The details of wall oscillations are extracted, and a small computational domain is established to focus solely on the flow details in the near-wall region, which can be shown in figure 2-8. The three possible LMUW modes, mentioned in the previous section, are also applied here, and the wall shape parameters and external flow conditions remain consistent with those shown in section 2.2. But the oscillation frequency is adjusted to achieve different wave speeds.

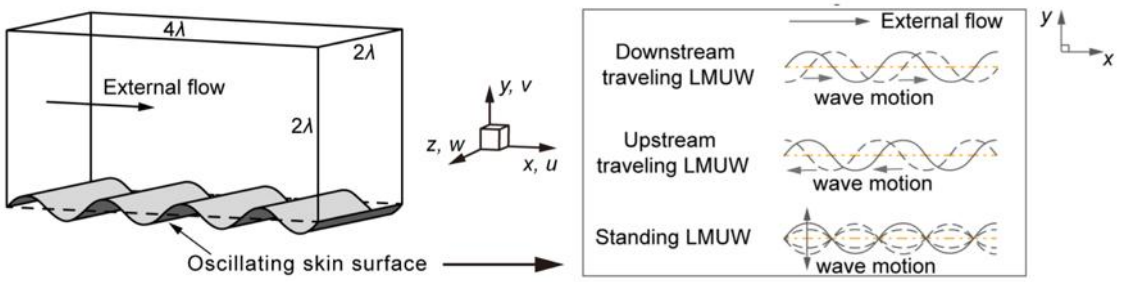

Figure 2-8 Computational domain for the flow details of dynamic boundary layer

The simulations were also conducted using ANSYS Fluent 16.0 software. The LES model with a subgrid-scale model (WALE) and a pressure-based solver were employed to resolve the turbulent flow over a computational domain of 4λ (streamwise)$\times 2\lambda$ (vertical)$\times 2\lambda$ (spanwise). According to the results in section 2.2, the LMUWs induce multilayer eddy motion in the near-wall region, extending approximately less than four wave amplitudes ($4a$) in the vertical direction, periodic eddy motion in the streamwise direction, and marginal secondary flow in the spanwise direction. This suggests that the computational domain size is sufficient to adequately cover the near-wall LMUW-actuated region. The

Reynolds number $Re=U\lambda/\upsilon$ (where υ is the kinematic viscosity of water), based on the external flow and wavelength, is approximately 1900, equivalent to the characteristic Reynolds number mentioned before. The constant mass-flow rate condition is applied at the given Reynolds number by setting a freestream velocity at the inlet, a pressure outlet condition at the outlet, a no-slip condition on the moving wall, a free-slip condition at the upper surface, and periodic boundary conditions at both spanwise boundaries. Wall oscillation is achieved using the dynamic mesh model in Fluent with a time step of T/500. The simulation is continued for 10 vibration cycles to obtain stable results and a fully developed near-wall boundary.

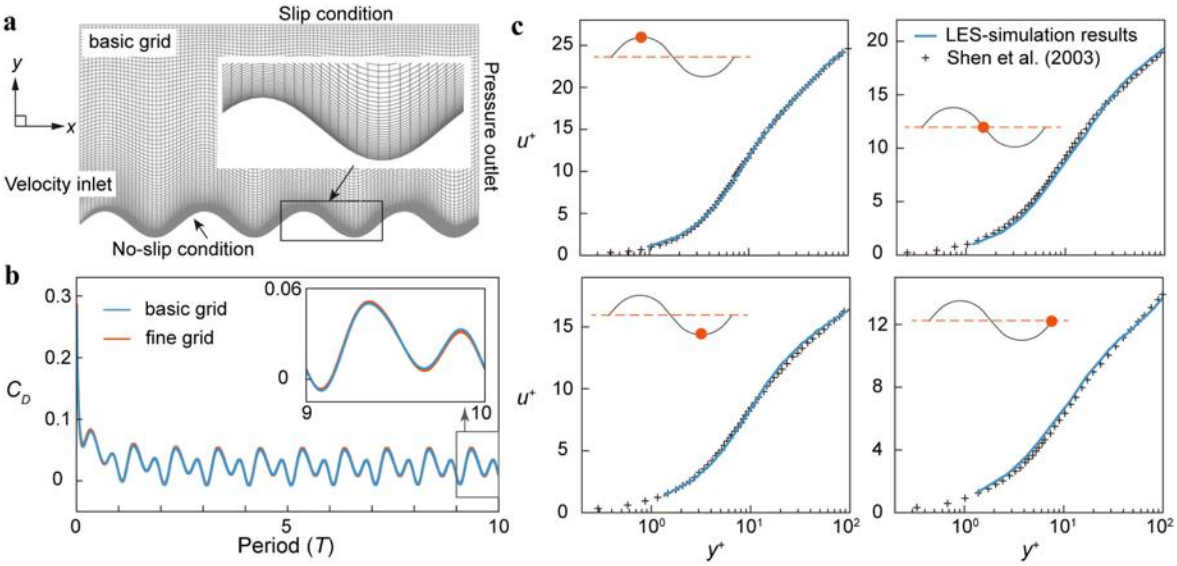

Figure 2-9 Mesh verification and validation

(a) Computational grid; (b) Mesh independence; (c) Validation

A structured grid system was employed, with grids clustered around the oscillating skin surface in the vertical direction and uniformly distributed in the streamwise and spanwise directions. Two grid resolutions were tested to ensure the mesh independency: a basic grid system [figure 2-9(a)] with 100 (streamwise)×50 (spanwise)×81 (vertical) nodes, and a fine grid system with 150 (streamwise)×75 (spanwise)×100 (vertical) nodes. The height of the first mesh layer in both systems were set as 0.001mm to guarantee $y^+=u_\tau y/\upsilon$ <1. Grid independence was verified under the downstream LMUW excitation by comparing the total drag coefficient (C_d). As shown in figure 2-9(b), the difference between the two grids is

minimal, indicating the achievement of mesh independence. Therefore, to obtain enough numerical accuracy with less computing time, the basic grid system shown in figure 2-9(a) was used for all subsequent simulations. This LES-based simulation method has been validated in section 2.2 by the comparison between the simulation results and experimental data from Kunze and Brücker [139], demonstrating excellent consistency. Here, we also compare our simulation results with that in the research of Shen et al. [72], who used a similar computational domain to simulate turbulent flow near a moving wavy wall with a *Re* of 10170, a wave steepness (*ka*) of 0.25 and c/U=1.2 (downstream traveling wave). As shown in figure 2-9(c), the velocity distributions at different locations within one wavelength are in good agreement, indicating that the LES formulation accurately captures the near-wall flow details around the dynamic wavy surface.

2.3.2 Dynamic boundary layer for traveling LMUWs

Simulated near-wall turbulent flows induced by traveling LMUW-based excitations are visualized on the *x-y* plane in mid-span, as depicted in figure 2-10. For comparison, the flow past a stationary wavy surface with the same shape parameters is also computed. This stationary case displays a typical near-wall vortex at the trough [figure 2-10(a)], exhibiting a "rolling bearing" effect that reduces skin friction drag, consistent with the drag reduction mechanism of traveling wave morphology on dolphin skin described in previous studies [18,103]. When the wavy wall is in motion, same as the results in section 2.2, the moving wall drives the surrounding fluid into motion. Consequently, for the upstream traveling LMUW, the flow inside the wall's concave region begins to exhibit a trend opposite to the external flow, whereas for the downstream LMUW, it remains in the same direction as the external flow [figure 2-10(b)]. As the frequency of LMUW excitation increases, the directional flow induced by wall oscillation becomes more intense, causing the original near-wall vortex to gradually dissipate and form a novel dynamic boundary layer. Due to the wavy motion, the upstream LMUW generates a reverse flow at the trough, while the downstream LMUW causes a small-area reverse flow at the crest. This reverse flow eventually aligns with the external flow direction with the increasing distance from the wall,. As a result, a saddle point flow (low-speed region) forms above the trough in upstream cases and above the crest in downstream cases, facilitating the transition of near-wall reverse flow into the external flow.

The typical dynamic boundary layer consists of the LMUW-induced directional flow (either in the same direction or opposite to the external flow) and the saddle point flow.

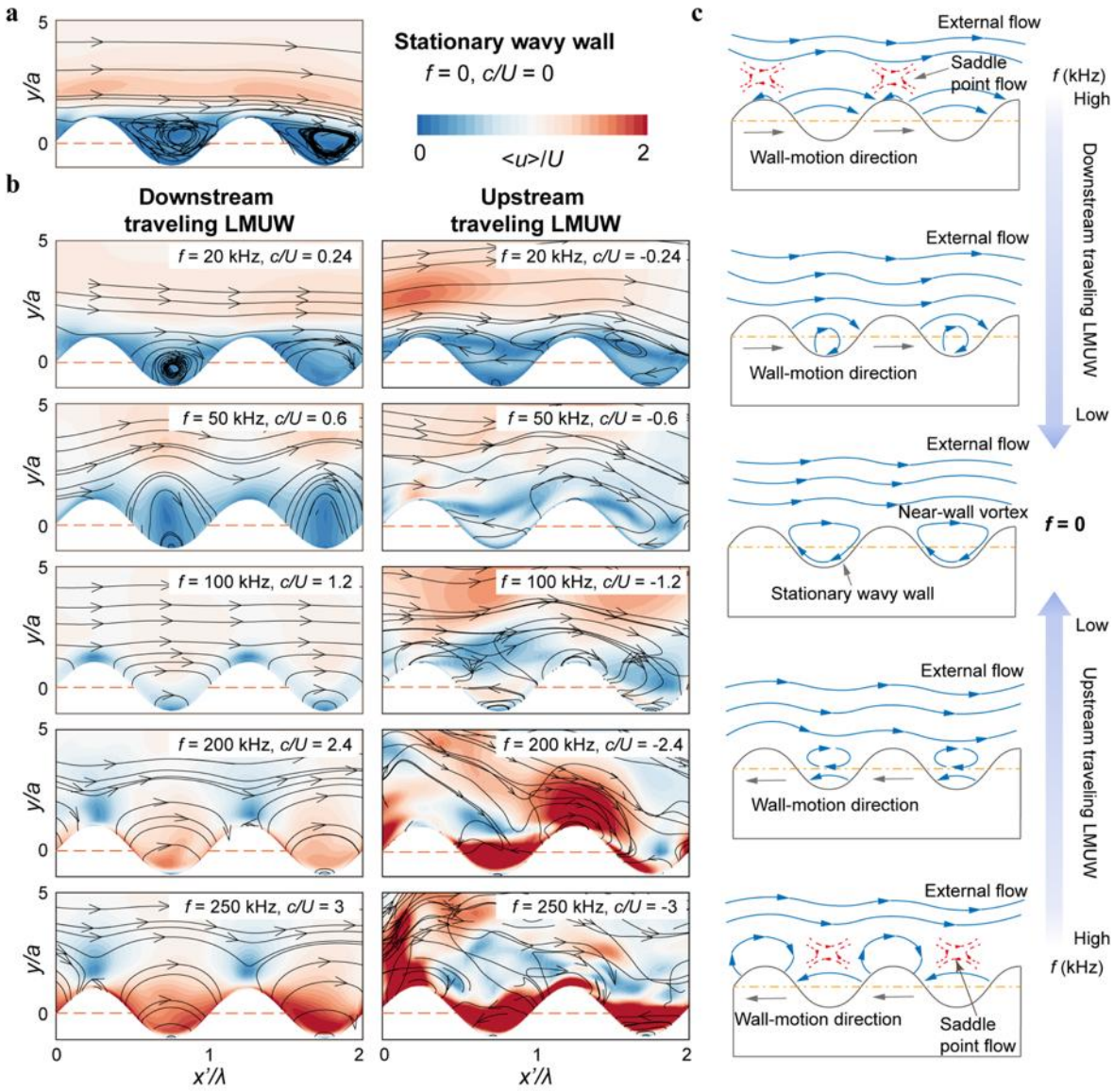

Figure 2-10 Dynamic boundary layer structures under traveling LMUWs

(a) Boundary flow near a stationary wavy wall; (b) Dynamic boundary flow structure; (c) Schematic of dynamic boundary layer variations

Figure 2-10(c) presents a schematic of the boundary flow variations as the oscillation frequency gradually approaches zero under different wave conditions. Notably, as the wavy

wall transitions from stationary to rapid oscillation driven by upstream LMUW, the reverse flow caused by wall motion occurs at the bottom of the trough, resulting in the near-wall vortex rising upward. Conversely, for downstream LMUW excitation, the motion-induced streamwise flow first appears at the entrance of the trough, causing the vortex to descend and become confined within the trough. As the frequency increases and the LMUW-induced directional flow strengthens, the near-wall vortex in upstream cases rises further into the external flow, introducing disturbances. In contrast, the vortex in downstream cases continues to be compressed until it eventually disappears, having no impact on the external flow. Therefore, as clearly shown in figure 2-10(b), the near-wall flow induced by upstream LMUW is more chaotic compared to the downstream LMUW excitation.

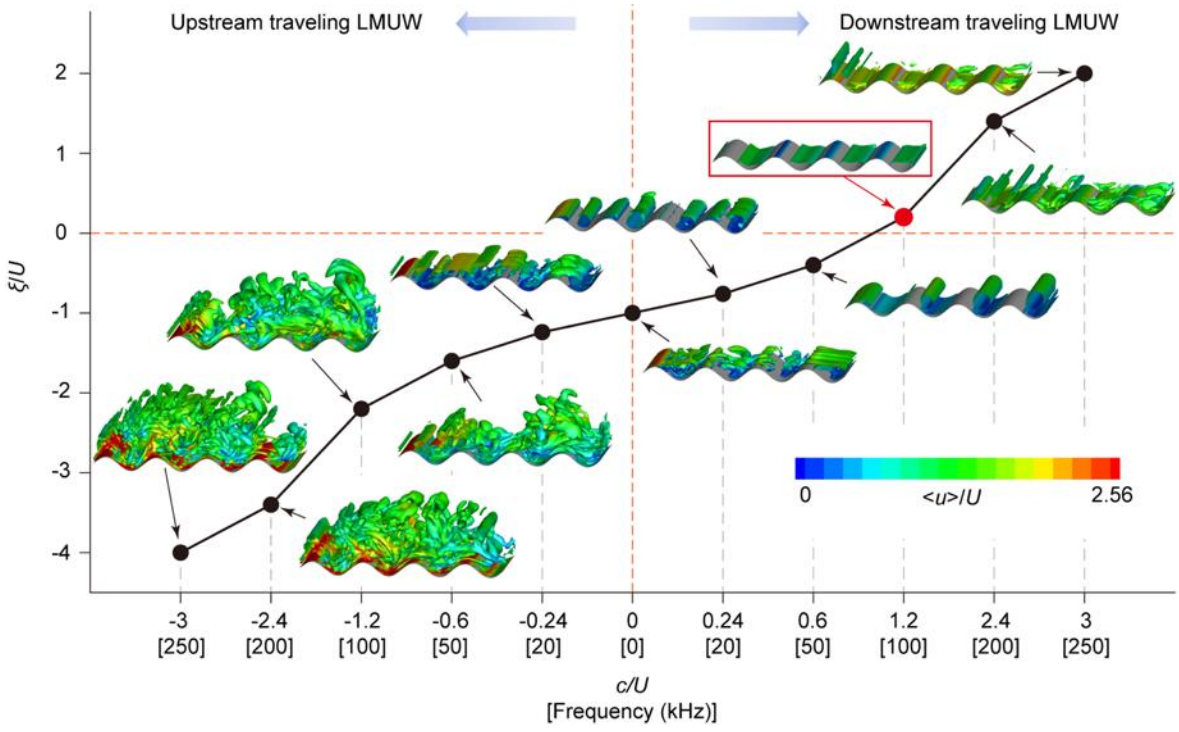

Figure 2-11 Vortices structure near the LMUW-motion wall surface

This observation is also reflected to the distribution of LMUW-induced vortical structures shown in figure 2-11, which is visualized by iso-surfaces of the Q-criterion of 1×10^9 with colors corresponding to the contours of velocity magnitude. In figure 2-11, the horizontal and vertical axes represent two key parameters: c and ξ, respectively. c is the wave speed, defined as $c=\lambda f$, with positive and negative values of c corresponding to downstream

and upstream LMUW, respectively. $\xi=c-U$ defines the relative velocity between wave propagation and external flow. Both parameters are normalized by the external flow velocity U. As illustrated in figure 2-11, vortical structure motion is most intense under upstream LMUW excitations, particularly when the oscillation frequency is higher, corresponding to larger absolute values of c and ξ. As the frequency decreases and c and ξ approach zero, the near-wall vortices gradually disappear, resulting in more stable flow. The most stable and orderly flow is observed when the oscillation frequency f is 100 kHz with downstream traveling LMUW oscillation, where vortical structures nearly vanish and ξ is closest to zero. As the relative velocity increases again in the positive direction (oscillation frequency increases to 200 kHz and 250 kHz for downstream LMUW), vortices reappear near the dynamic skin surface. The results in figure 2-11 highlight that the relative velocity ξ significantly affects LMUW-induced near-wall flow characteristics. When ξ approaches zero, the propagation speed of LMUW is nearly identical to the external flow velocity U, resulting in the most stable boundary flow. However, as the relative velocity increases in either direction, the speed difference between wall motion and external flow grows, intensifying their interaction and leading to more turbulent flow.

2.3.3 Dynamic boundary layer for standing LMUWs

Traveling LMUWs propagate without altering the shape of the wave, while standing LMUWs exhibit a different characteristic with no propagation but a time-vary wall configuration. We simulated the dynamic skin oscillation in the form of standing LMUWs and observed more complex near-wall flow structures due to the time-varying shape. At $0T$ and $0.5T$, the near-wall flow displays a vortex similar to that observed with a stational wavy wall when the shape of wavy wall is identical to the original static waveform. However, at $0.25T$ and $0.75T$, when the wall shape varies, the flow forms a distinctive dynamic boundary layer featuring a saddle point flow, streamwise flow, and reverse flow, as illustrated in figure 2-12. Unlike the high dependence on the frequency under traveling LMUWs, the near-wall flow induced by standing LMUW is independent of the skin oscillation frequency. The flow patterns observed in figure 2-12 are consistent across all frequency conditions, and the vortical structures are not significantly affected by frequency variations.

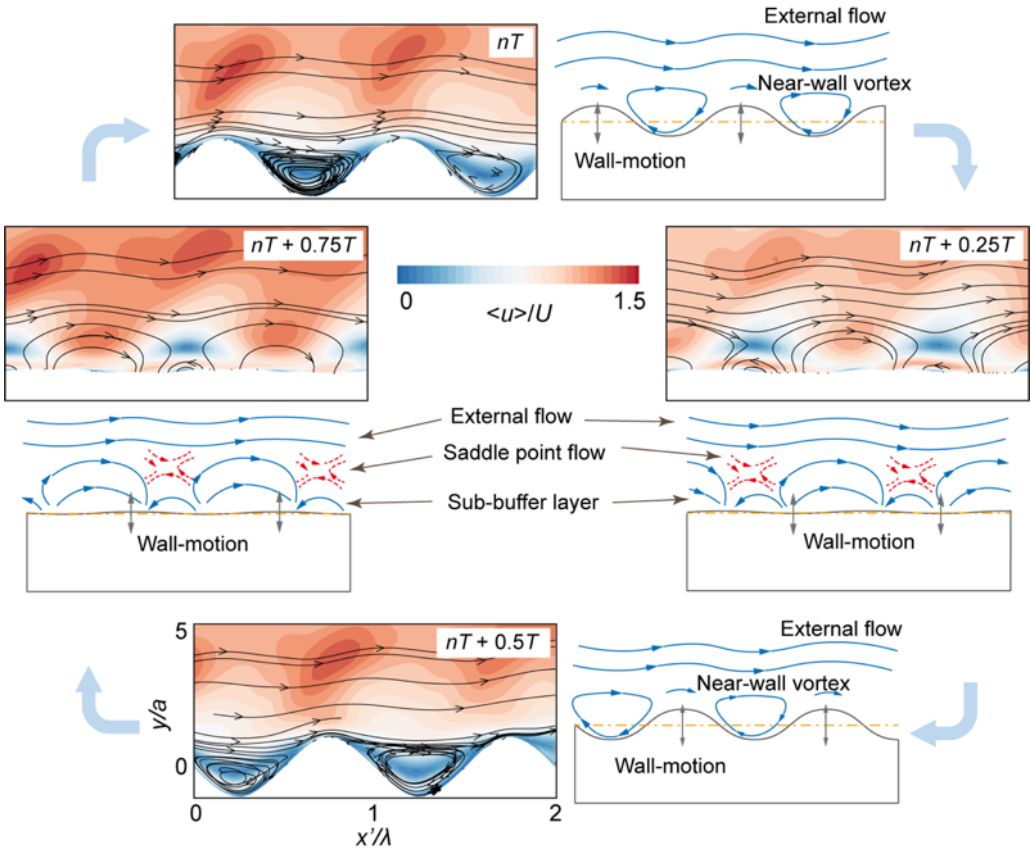

Figure 2-12 Dynamic boundary layer structures under the standing LMUWs

2.4 LMUW-INDUCED DRAG FORCE DISTRIBUTION

It should be noted that different modes of LMUW interact with the incoming flow at the inlet, creating a periodically varying high-speed region near the inlet (confined within a wavelength range close to the inlet), particularly for the upstream traveling and standing LMUWs. To eliminate the influence of this inlet effect on the force distribution, we only consider forces within the two wavelength ranges near the outlet for calculating the drag coefficients in subsequent analyses. Figure 2-13 demonstrates the drag forces under the traveling LMUW conditions. It can be found that the relationship between near-wall flow characteristics and the relative velocity can be precisely reflected in the distribution of pressure drag. As indicated in figure 2-13(a), zero pressure resistance occurs when the near-wall flow is most stable (near the relative velocity of ξ=0). As the absolute value of ξ

increases, the near-wall flow becomes more intense (figure 2-11), leading to an increase in pressure resistance. However, since the propagation directions of upstream and downstream traveling LMUWs are opposite, the interaction direction between wave motion and external flow is also reversed. Consequently, the direction of pressure drag is positive when $\xi<0$ and negative when $\xi>0$. The results in an overall monotonic decrease in pressure resistance as the wave speed c and relative velocity ξ increase. Notably, the pressure drag is negative, indicating a thrust effect in a significant portion of the region where $\xi>0$ [highlighted by the green shadow in figure 2-13(a).

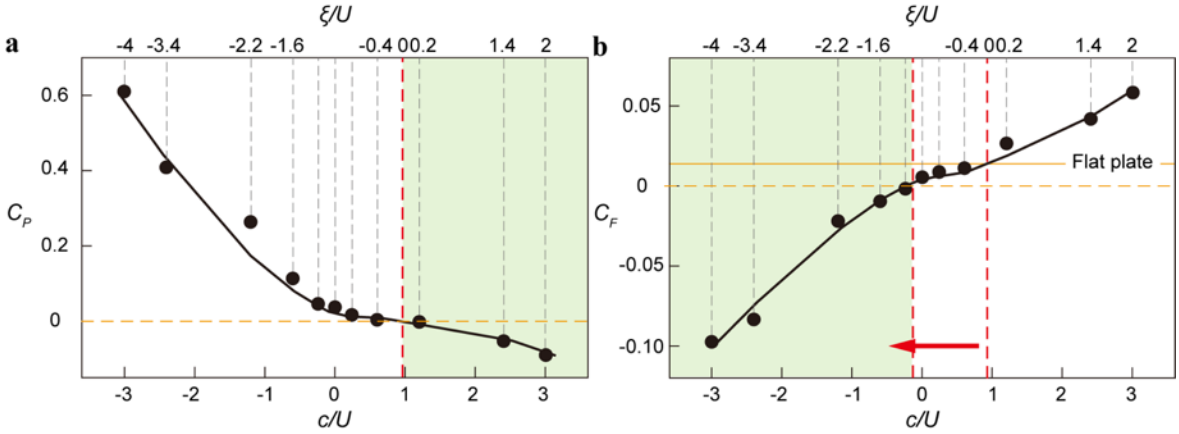

Figure 2-13 Drag coefficients distribution under traveling LMUWs

(a) Pressure drag; (b) Friction drag

In contrast to pressure drag, the direction of friction drag relies more on the near-wall flow direction and is thus primarily influenced by wave speed c. Zero friction drag occurs near $c=0$ [figure 2-13(b)]. Upstream LMUW (with $c<0$) induces a near-wall reverse flow, resulting in negative friction force, whereas downstream traveling waves (with $c>0$) align the induced flow with the external flow, resulting in positive friction resistance. This indicates that under upstream LMUW excitations, the friction drag consistently exhibits a thrust effect [highlighted by the green shadow in figure 2-13(b)]. Additionally, friction resistance is also observed when flowing over a stationary flat plate, indicated by the orange solid line in figure 2-13(b) under the same simulation conditions. Generally, if the friction resistance is less than that on the flat plate, it is considered to achieve the drag reduction. As shown in figure 2-13(b), the LMUW-induced friction drag is comparable to that of a flat

plate near ξ=0, indicating that the friction-based drag reduction due to dynamin skin oscillation occurs when ξ<0 (indicated by the red arrow).

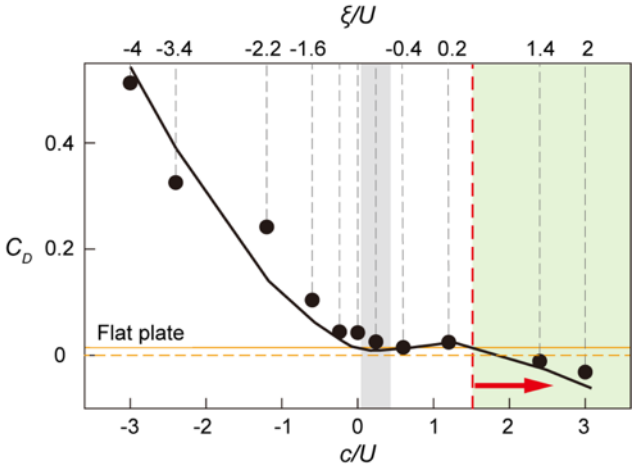

Figure 2-14 Total drag coefficients under the traveling LMUW conditions

The total drag is the combination of friction and pressure drag. As illustrated in figure 2-14, the linear superposition of these two components results in a complex fluctuation pattern in the relationship between total drag and velocity (c and ξ), rather than a simple monotonic variation. Specifically, the total drag exhibits a pattern of decreasing, then increasing, and decreasing again as c and ξ increase. By comparing the total drag acting on a flat plate (shown by the orange solid line), we identify two distinct regions of drag reduction induced by dynamic skin oscillation. The first drag reduction region, highlighted by the gray shading in figure 2-14, occurs when c/U>0 and ξ/U<0, and is primarily dominated by friction drag. In this region, the LMUW-induced drag reduction in friction can offset the pressure drag resulting from the wall shape, leading to an overall reduction in total drag. This mechanism of drag reduction through dolphin-inspired traveling wave surface morphology has been discussed in previous studies [18,65,72,103,111]. However, the range of wave speeds that achieve drag reduction in this region is very limited, highly dependent on the motion and shape parameters of the wall surface, and the overall drag reduction effect is quite constrained. The second drag reduction region, indicated by the green shading in figure 2-14, is dominated by pressure drag due to high-frequency dynamic skin micro-oscillations. In this region, the reduction in pressure contributes to the total drag reduction. This region

corresponds to most of the area where ξ>0. As ξ continues to increase positively, the total drag on the dynamic wall decreases, potentially even becoming negative and resulting in a thrust effect. The pressure-dominated drag reduction mechanism, inspired by the dynamic skin behaviors of dolphin, offers a broader range of wave speed options, greater design flexibility, and improved efficiency in drag reduction performance.

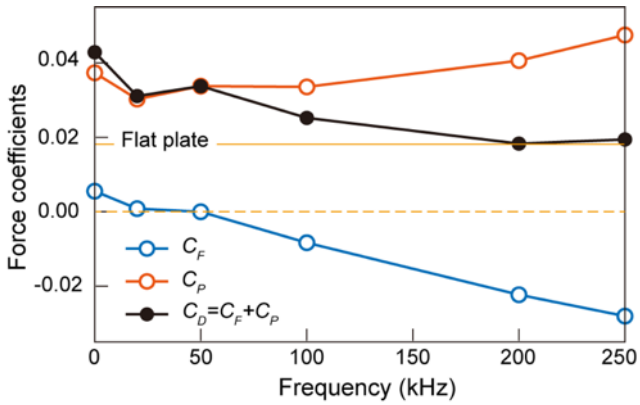

Figure 2-15 Total drag coefficients under the standing LMUW conditions

This consistency in near-wall flow also indicates that the drag distribution for standing LMUWs does not exhibit the significant variations observed in traveling LMUW cases. As shown in figure 2-15, while the drag forces induced by standing LMUWs display some monotonic trends with frequency—such as a decrease in friction drag and an increase in pressure drag as frequency rises—these variations are relatively limited. Consequently, the total drag remains close to that of a flat plate and does not approach the drag reduction observed with traveling LMUWs, where the total drag can even be eliminated. This underscores the importance of wave propagation characteristics in achieving effective drag reduction, particularly in methods dominated by pressure drag.

2.5 SUMMARY

In this chapter, we have proved that the dolphin-inspired near-wall ultrasonic microvibrations in the form of LMUWs enable active control of the wall-bounded turbulent flow while achieving effective drag reduction. A series of LES simulations were undertaken in association with LMUW-actuated turbulent flows in an open channel in terms of two

traveling waves in the streamwise direction and a standing wave. The main findings can be seen as follows:

(1) The LMUW excitation enables the creation of a novel dynamic boundary layer, effectively altering the multi-eddy motion in the viscous sublayer and achieving active manipulation of both direction and magnitude of the near-wall velocities. The dynamic boundary layer is significantly distinguished from the conventional boundary layer, consisting of LMUW-induced directional flow and saddle point flow. The downstream traveling LMUW induces an intense downstream flow while the upstream traveling waves create an upstream flow, i.e., a reversed velocity against the freestream incoming flow; and the standing wave produces more complicated velocity fluctuations actuated by the time-varying wall configuration. A transverse roller-like flow structure is observed in all three motion modes, indicating that the LMUW-excited wavy wall motions can actively regularize the near-wall dynamic boundary flow. Different from the conventional streamwise traveling wave wall-deformation approaches, the LMUW-based active flow control enables manipulation of the local microscale shear flow and velocity fluctuations without exerting any significant influence on the surrounding macroscale flow fields.

(2) The LMUW-based active flow control method was verified to be able to achieve a remarkable reduction and even extinguishment in friction or pressure drag while resolving the tradeoff between them. The wave propagation characteristics of traveling LMUWs are crucial in determining force variations. The upstream traveling LMUW creates a reversed wall shear, resulting in a negative friction drag in the range of $c<0$. And the friction drag reduction can be achieved when $\xi=c-U<0$. When the direction of the traveling LMUW aligns with the external flow ($c>0$), and the relative velocity $\xi>0$, the pressure drag becomes negative and increasingly exhibits a thrust effect as c and ξ increase. At this point, pressure drag dominates the total drag, creating a second drag reduction region that encompasses most of the area where $\xi>0$, potentially reducing or even eliminating total drag. This pressure-dominated drag reduction method offers a broader range of wave speed options, greater flexibility, and superior drag reduction capability, providing new design possibilities for drag reduction technology. The standing waves lack propagation characteristics, thus do not have as significant an impact on drag as traveling LMUWs.

(3) The pressure-dominated drag reduction induced by skin oscillations bears a striking resemblance to the pressure-based propulsion achieved by low-frequency, large-amplitude traveling waves generated by a fish's tail during swimming. However, the micro-scale oscillations on dolphin skin affect only the local flow near the skin without significantly impacting the macro flow. This allows dolphin skin to achieve effective drag reduction through dynamic oscillations without compromising overall propulsion and may even provide additional thrust. This pressure-dominated drag reduction approach offers new insights into understanding the Gray's paradox in relation to dolphin swimming.

Chapter 3 THEORETICAL ANALYSIS OF LMUW-EXCITED DYNAMIC BOUNDARY LAYER

3.1 INTRODUCTION

In 1904, Prandtl first proposed the concept of boundary layer. Due to the fluid viscosity, there exists a thin fluid layer near the object with a large velocity gradient, which is known as the boundary layer. In this layer, the flow at the object surface has a velocity of zero, while the fluid velocity increases to approach the value of external flow in a short distance away from the surface. For the boundary layer near a flat plate, the turbulence within it can generally be divided into four regions with different characteristics: viscous sublayer, buffer layer, log-law layer, and outer layer. The viscous sublayer is the fluid layer directly adjacent to the wall, with an extremely thin thickness, where the fluid largely maintains laminar flow characteristics. The buffer layer, as the name suggests, is the transition region between the viscous sublayer and the log-law layer. The log-law layer is a fully developed turbulent region, typically considered the core of turbulent boundary layer. As the fluid extends outwards, it reaches the outer layer, which is the transition from the boundary flow to the non-fluctuating external flow in my understanding. The velocity distribution in the outer layer is influenced by the main flow, while the inner layer of the boundary is more closely related to the condition of the wall [5,144]. Figure 3-1 shows the typically distribution (red line) of non-dimensional velocity (u^+) versus non-dimensional distance from the wall (y^+). The two blue lines represent the theoretical linear and logarithmic distributions of u^+ and y^+. It can be observed that in the viscous sublayer ($0 < y^+ < 5$), the relationship between u^+ and y^+ follows a linear pattern $u^+=y^+$, while in the log-law region ($y^+ > 30$~100), it follows the regularity of $u^+ = (1/\kappa)\ln(y^+) + B$, where κ and B are constants, called the additive constant (usually, $B = 5.5$) and von Kármán constant (usually, $\kappa = 0.41$), respectively [5,144].

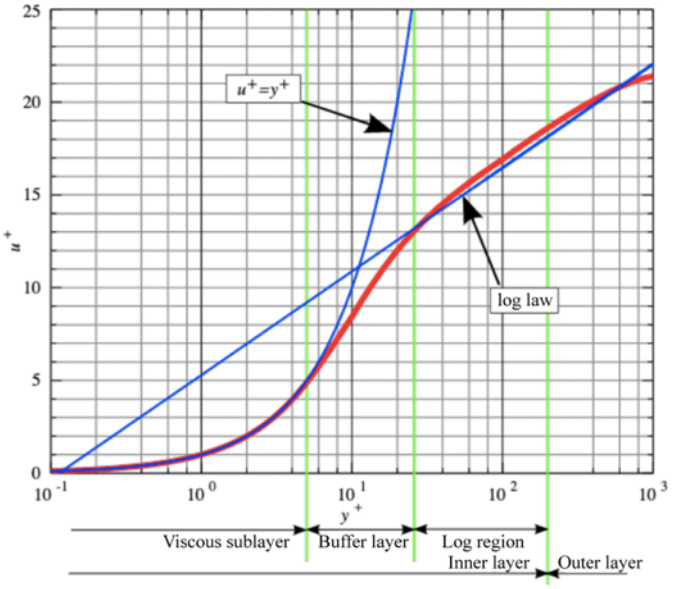

Figure 3-1 Plot of velocity u^+ near the wall against distance y^+ from the wall [5]

The velocity gradient in boundary layer directly affects the wall shear stress, thereby influencing frictional drag. The traditional velocity distribution in a turbulent boundary layer over a flat plate, as shown in figure 3-1, is based on a smooth and stable surface, where the velocity gradually increases from 0 at the wall to the free stream. However, when the local movement occurs on the wall, this velocity distribution changes, causing the flow within the boundary to no longer follow the conventional distribution pattern. As mentioned in chapter 2, a novel dynamic boundary layer is induced by the LMUW motion in the wall, resulting in a different drag distribution and thus introducing a new drag reduction mechanism. In this chapter, we focus on the LMUW-induced dynamic boundary layer, establish its velocity model, and conduct a theoretical analysis of the drag reduction mechanism under dynamic wall condition.

3.2 TWO-DIMENSIONAL LMUW MOTION MODEL

The results in chapter 2 suggest that the LMUW-excited dynamic boundary layer displays a typical 2D flow structure on the *x*-*y* plane with a marginal spanwise flow (only perturbations in spanwise direction). This means that the flow in only streamwise and

vertical directions is sufficient to capture most of the information about the LMUW-induced dynamic boundary. With the goal of exploring the drag-reduction mechanisms in dolphin swimming corresponding to the problem of external flow around a moving body, we consider a two-dimensional (2D) wavy plate model, as illustrated in figure 3-2, undergoing the same LMUW-excited wall motion and carries out a series of 2D Reynolds-averaged Navier-Stokes (RANS) [shear-stress transport (SST) *k*-*ω*]-based simulations.

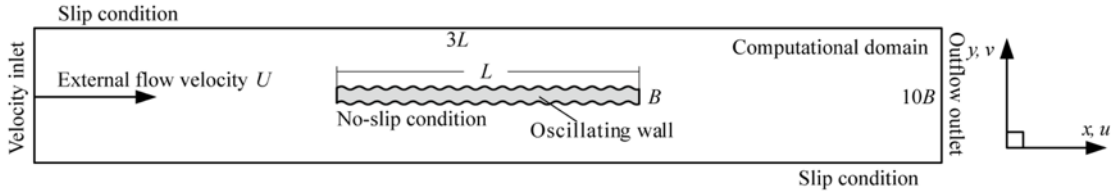

Figure 3-2 Computational domain of 2D LMUW motion model

3.2.1 RANS modeling

3.2.1.1 Introduction of RANS (SST *k*-*ω*) model

In Reynolds averaging method, the variables in the instantaneous (exact) N-S equations are decomposed into two parts: the time-averaged component and the fluctuating component. This decomposition is defined as:

$$u_i = \overline{u_\iota} + u_i', \tag{3-1}$$

where $\overline{u_\iota}$ and u_i' are the time-averaged and fluctuating velocity components. By substituting the decomposition of the flow variables into the governing equations and then taking a time average, the time-averaged momentum equation can be derived. In Cartesian coordinate, these equations are expressed as [137]:

$$\frac{\partial(\rho\overline{u_\iota})}{\partial x_i} = 0, \tag{3-2}$$

$$\frac{\partial(\rho\overline{u_\iota})}{\partial t} + \frac{\partial}{\partial x_j}\left(\rho\overline{u_\iota}\overline{u_j} + \rho\overline{u_\iota' u_j'}\right) = -\frac{\partial\bar{p}}{\partial x_i} + \frac{\partial\overline{\tau_{\iota J}}}{\partial x_j}, \tag{3-3}$$

where the $\overline{\tau_{\iota J}}$ are the mean viscous stress tensor components:

$$\overline{\tau_{\iota J}} = \mu\left(\frac{\partial\overline{u_\iota}}{\partial x_j} + \frac{\partial\overline{u_j}}{\partial x_i}\right). \tag{3-4}$$

The presence of the Reynolds stresses means that these equations are not closed. To close the equations, the turbulent model must be introduced. In laminar flows, the transport of

mass, momentum, energy, and energy dissipation, is governed by the viscosity, so in turbulent flows, it is reasonable to represent the effects of turbulence as an increased viscosity. This assumption leads to the concept of eddy-viscosity, which is used to model the Reynolds stress in turbulent flows [137]:

$$-\rho\overline{u_i'u_j'} = \mu_t\left(\frac{\partial\overline{u}_i}{\partial x_j}+\frac{\partial\overline{u}_j}{\partial x_i}\right)-\frac{2}{3}\rho\delta_{ij}k, \qquad (3-5)$$

where k and μ_t is the turbulent kinetic energy and the turbulent viscosity, respectively. These equations are still not closed, and these Reynolds stresses need to be modeled to close these equations. The SST k-ω model is a two-equation model that solves two modeled transport equations for k and the specific dissipation rate (ω). The k-ω model is initially proposed by Saffman but popularized by Wilcox [137,138]. The SST k-ω model developed by Menter is a popular variant of k-ω model and has the following transport equations for k and ω [138]:

$$\frac{\partial}{\partial t}(\rho k)+\frac{\partial}{\partial x_i}(\rho k\overline{u}_i)=\frac{\partial}{\partial x_j}\left(\Gamma_k\frac{\partial k}{\partial x_j}\right)+G_k-Y_k+S_k, \qquad (3-6)$$

and

$$\frac{\partial}{\partial t}(\rho\omega)+\frac{\partial}{\partial x_j}\left(\rho\omega\overline{u}_j\right)=\frac{\partial}{\partial x_j}\left(\Gamma_\omega\frac{\partial\omega}{\partial x_j}\right)+G_\omega-Y_\omega+D_\omega+S_\omega. \qquad (3-7)$$

In the two equations, the terms G_k and G_ω represent the production of k and the generation of ω, respectively. Γ_k and Γ_ω represent the effective diffusivity of k and ω, respectively. Y_k and Y_ω represent the dissipation of k and ω due to turbulence. D_ω represents the cross-diffusion term. S_k and S_ω are user-defined source terms. The turbulent viscosity μ_t in k-ω model is computed by the combination of k and ω as follows:

$$\mu_t=\alpha^*\frac{\rho k}{\omega}. \qquad (3-8)$$

The coefficient α^* is used for a low-Re correction by damping the turbulent viscosity. In SST k-ω model, the turbulent viscosity is refined to incorporate the transport of the turbulent shear stress, enhancing the predictive accuracy and reliability of the SST k-ω model for a wider range of flows (for example, adverse pressure gradient flows, airfoils, transonic shock waves). The use of RANS model is because, in many cases, researchers are only interested in just a few quantitative properties of a turbulent flow. Here, we focus on the mean velocity

distribution illustrated in figure 3-1. Considering the 2D state of this model, we chose the RANS (SST *k*-*ω*) model for CFD simulations to model the velocity of the dynamic boundary layer, aiming to conserve computational resources and improve efficiency.

3.2.1.2 Validation of RANS model

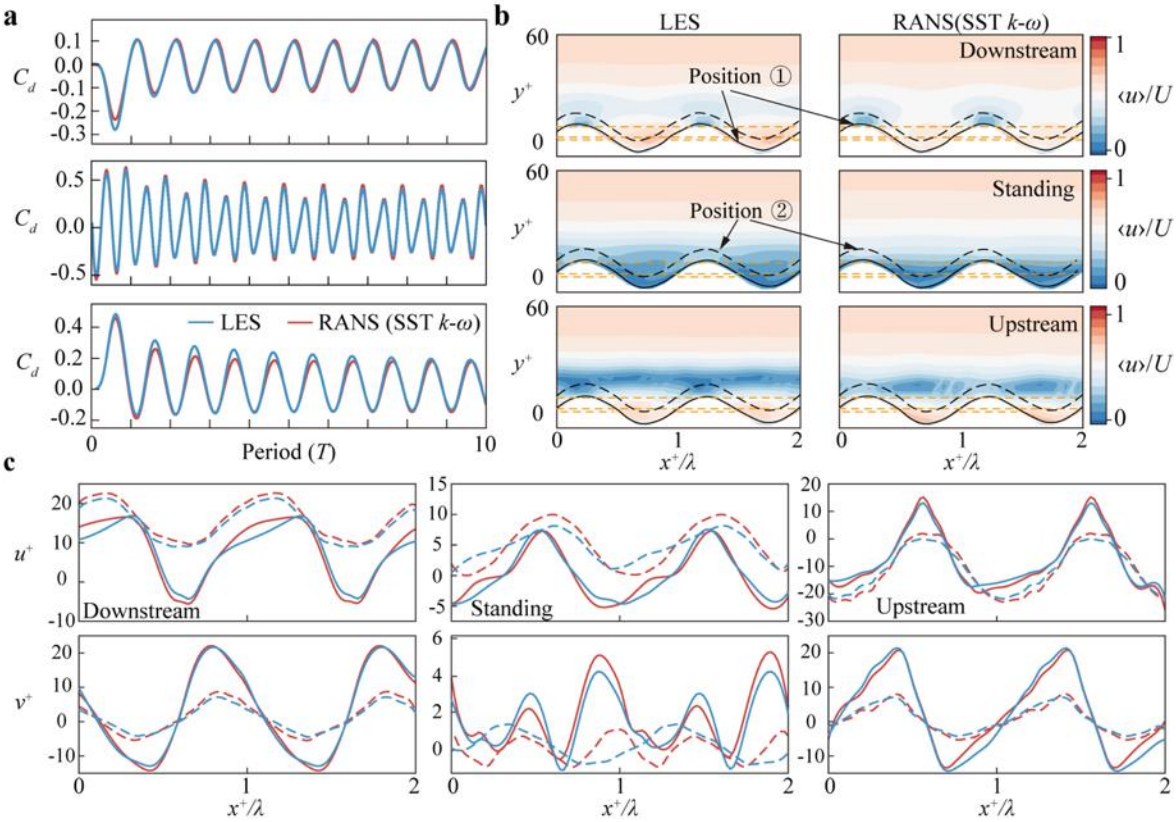

Figure 3-3 Validation of RANS (SST *k*-*ω*) model

(a) Comparation of total drag coefficients; (b) Near-wall flow structures; (c) Distributions of streamwise velocity and vertical velocity.

To confirm whether RANS-based simulations with SST *k*-*ω* turbulent model can reasonably simulate the LMUW-excited dynamic boundary flow, we construct 3D RANS (SST *k*-*ω*) simulations for three motion modes based on the computational domain shown in figure 2-3 and compared the results with those from the 3D LES scheme. Figure 3-3(a) and (b) show the total drag coefficients and near-wall flow structures in the streamwise direction, respectively. There is good agreement in both the near-wall flow structures and total drag

coefficients. In addition, the streamwise and vertical velocity distributions are compared to two positions with distances of 0.2a (very close to the wall) and a from the undulating wall, respectively. As illustrated in figure 3-3(c), the velocity distributions in the downstream and upstream traveling LMUWs are observed well consistent between LES and RANS (SST k-ω) models. However, there exist pronounced differences in the vertical velocities in association with the standing LMUW between the two models, which exert less effect on the total drag coefficients as illustrated in figure 3-3(a). This indicates that the RANS (SST k-ω) model is capable of predicting the LMUW-excited boundary layer and drag forces in a quantitative way comparable to the 3D LES scheme.

3.2.1.3 Mesh verification

The 2D RANS simulations are also performed in ANSYS Fluent 16.0. The pressure-velocity coupling algorithm (PISO) was used to solve the incompressible N-S equations, with the least-squares cell-based scheme for solving the gradient and the second order scheme for pressure. To improve the computational accuracy, the second-order upwind scheme was employed to discretize the momentum, turbulent kinetic energy and specific dissipation rate. The model constants were all set to the default values in Fluent. Fully developed turbulent flows around a 2D wavy plate (figure 3-2) undulating according to equations (2-1) and (2-2) throughout the upper and lower walls were simulated in a computational domain of $3L \times 4B$, where L=100 mm and B=4 mm are the length and width of the plate, respectively. The shape parameters of LMUW (λ= 150 μm; a=20 μm) keep consistent with the 3D simulations in chapter 2. Wall undulations occur throughout the plate model from the beginning of the simulation. Similar computational conditions to the 3D cases were employed for the boundary conditions (free-slip condition at upper and lower boundaries, velocity inlet with external flow U=12.5 m/s, outflow outlet and no-slip condition on the wall), time step (T/500), dynamic remeshing of the wavy wall with the mesh method of diffusion (boundary-distance), and up to 20 undulating cycles in every simulation. The height of the first mesh layer adjacent to the wall surface was set to 0.0004 mm (satisfying $y^+<1$) to capture more details in boundary flow. And an evenly spaced grid with 15059 nodes (basic grid) was used in the streamwise direction on the wall surface. Mesh independence was verified, as shown in figure 3-4, through a comparison of the total drag

coefficients, near-wall flow structures, and velocity distributions at different positions (the distance of 0.2a and a from the undulating wall) under the upstream traveling wave mode at 0T when f=100 kHz given by a basic grid and a refined grid (21294 nodes on the wall surface). The results indicate that the basic grid can accurately compute the flow fields and total drag coefficients. Therefore, with consideration of enough numerical accuracy and less computing time, a series of 2D RANS (SST k-ω)-based simulations in association with the 2D wavy plate model were undertaken to determine the theoretical velocity model for the LMUW-excited dynamic boundary layer.

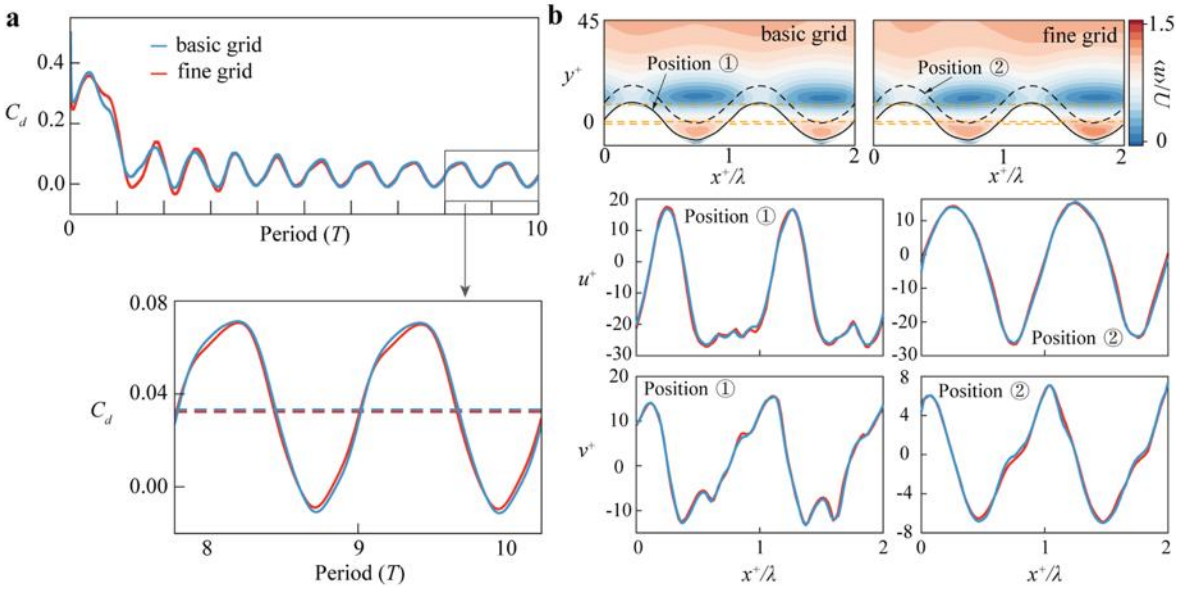

Figure 3-4 Mesh verification

(a) Total drag coefficients; (b) Near-wall flow distributions

3.2.2 Boundary velocity distribution

Due to the wavy wall surface, we first performed a coordinate transformation for clearer explanation. As illustrated in figure 3-5, in the transformed coordinate system, $\xi = x$, $\psi = y$-y_w, and $\tau = t$, where ψ is the vertical distance from the wall (with ψ=0 on the wall). Since the wall LMUW motion is a periodic function of position x and time t, the near-wall fluid retains the relevant characteristics of the wall motion due to the fluid viscosity, resulting in periodic velocity variations. Figure 3-6 displays the velocity data corresponding to different distances from the wall ψ, revealing that the velocity distribution near the wall also exhibit periodic

regularity with changes in position and time.

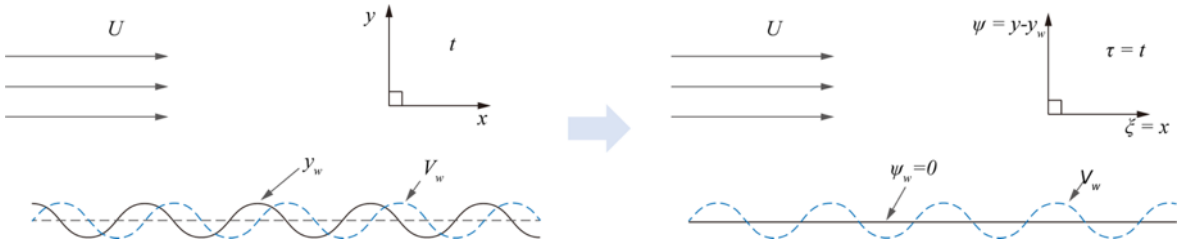

Figure 3-5 Coordinate transformation

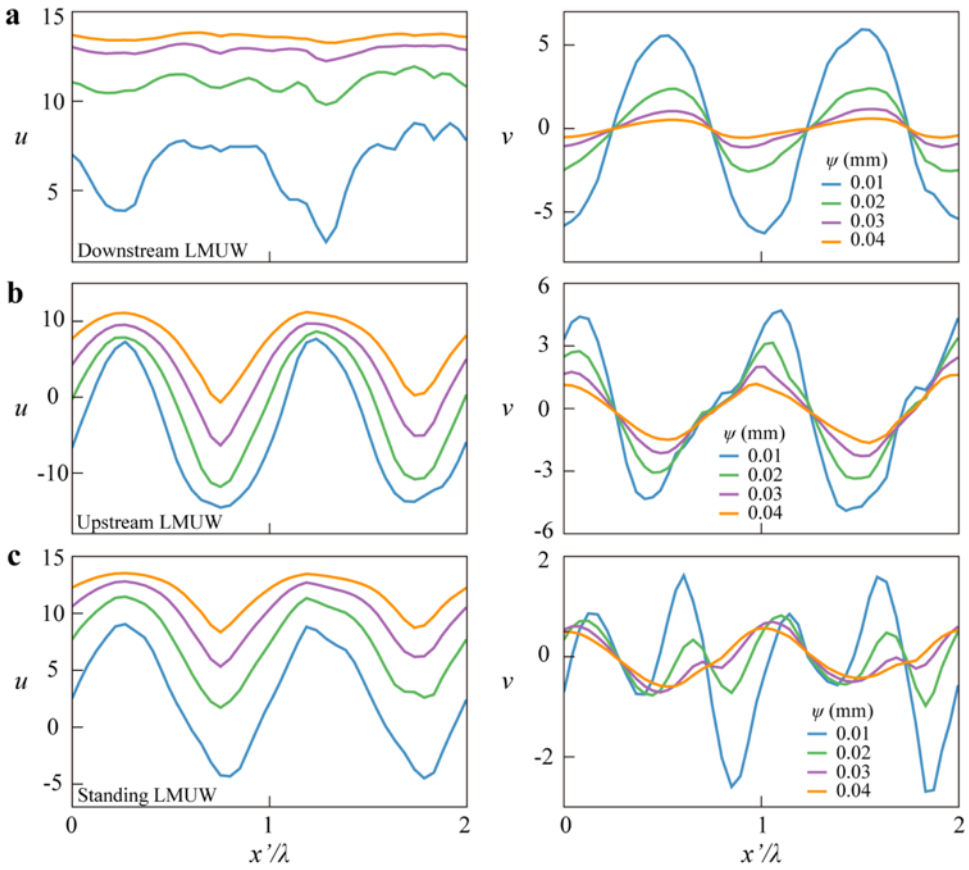

Figure 3-6 Near-wall velocity distribution

(a) Downstream traveling LMUW; (b) Upstream traveling LMUW; (c) Standing LMUW

However, as can be seen from figure 3-6, although the velocity data is periodic, it is evident that its distribution is more complex compared to the wall motion function [equations (2-1) and (2-2)], which cannot be expressed by a simple harmonic function like the wall motion. Therefore, we consider using a Fourier series to represent these periodic velocity distributions here. The Fourier series, named after the French mathematician Joseph Fourier,

proposes that any function can be expanded into a trigonometric series. In mathematics, the Fourier series is a way of expressing wave-like functions as simple harmonics, making it well-suited for addressing the periodic velocity distribution we observed here. Considering that there is a normal velocity on the wall, the vertical velocity v equals the wall motion velocity when ψ=0. As ψ increases, v gradually attenuates due to the influence of fluid viscosity, but the centerline of v at different positions remains near zero, as shown in figure 3-6. Thus, we assume that the mean value of the vertical velocity is always zero. However, the centerline of the streamwise velocity changes with ψ, making the mean velocity of u a function dependent on the distance. Therefore, the velocity profile for traveling LMUWs can be expressed by:

$$u = \sum_{b=1}^{n} h_b^i(\psi) \sin\left[bk(\xi - c\tau) + \varphi^i\right] + G(\psi), \qquad (3-9)$$

and

$$v = f(\psi)(-kca)\cos[k(\xi - c\tau)] + \sum_{m=1}^{n} h_m^i(\psi) \sin\left[mk(\xi - c\tau) + \varphi^i\right]. \qquad (3-10)$$

The velocity profile for standing LMUWs is given by:

$$u = \sum_{b=1}^{n} h_b^{ij}(\psi) \sin\left[b(2\pi f\tau) + \varphi^i\right] \sin\left[b(k\xi) + \varphi^j\right] + G(\psi), \qquad (3-11)$$

and

$$v = f(\psi)(-2\pi fa)\sin(2\pi f\tau)\sin(k\xi) + \sum_{m=1}^{n} h_m^{ij}(\psi) \sin\left[m(2\pi f\tau) + \varphi^i\right] \sin\left[m(k\xi) + \varphi^j\right]. \qquad (3-12)$$

It can be understood physically as a linear superposition of the freestream flow-induced and oscillating wall-excited components. The Fourier series terms including the first term in u and the second term in v represent the LMUW-excited perturbations to the streamwise and vertical velocity components. $h(\psi)$ (equal to 0 at ψ=0) are the perturbation coefficients and φ is the phase with $\varphi^1 = 0$, $\varphi^2 = \pi/2$, i=1, 2. The second term in u, namely the function $G(\psi)$, represents the centerline (mean velocity) of the streamwise velocity, which is only dependent on the distance from the wall ψ but independent on the periodic elements (position x and time t). This can be used to express the incoming flow-induced streamwise velocity component as seen in conventional boundary flow around a flat plate (red line in figure 3-1). The first term in v express the contribution of the wavy wall motion to the vertical velocity component with an attenuation coefficient $f(\psi)$, which is a function of the moving wall

velocity and fluid viscosity. Here, we use the Fourier series terms to describe the perturbations within boundary layer. Due to the inclusiveness of Fourier series, these perturbations not only include the periodic flow variations caused by the LMUW motion but also describe the chaotic turbulent fluctuations in turbulent boundary. During the discussion of 3D simulations in chapter 2, we realized that the velocity distributions in the spanwise direction are due to the turbulent disturbances caused by wall motion. Therefore, when this velocity model needs to be extended to three dimensions, we can also define the spanwise disturbances using Fourier series terms, express as for traveling LMUWs:

$$w = \sum_{g=1}^{n} h_g(\psi) \sin[gk(\xi - c\tau) + \varphi(\zeta)], \qquad (3-13)$$

and for standing LMUWs:

$$w = \sum_{9=1}^{n} h_g^{ij}(\psi) \sin\big[g(2\pi f\tau) + \varphi^i(\zeta)\big] \sin\big[g(k\xi) + \varphi^j(\zeta)\big]. \qquad (3-14)$$

However, it should be noted that these two equations are provided for reference only when considering spanwise flow. Most of the important information within the dynamic boundary layer is still concentrated in the *x*-*y* plane.

The velocity distribution for the LMUW-induced dynamic boundary layer was validated through the comparison with the simulation-based results, as shown in figure 3-7. The simulation-based velocity data were extracted for 70 groups of ψ values and applied the second-order Fourier series to the velocity profile model, which was used as a primary function for velocity data fitting (MATLAB R2022a, USA). Excellent consistency can be seen between the simulation and the model-based fitting results, indicating that the velocity profile model can provide an effective theoretical method for the novel dynamic boundary problem. Figures 3-8 and 3-9 display the coefficient function [$G(\psi)$, $f(\psi)$ and $h(\psi)$] distributions in the second-order velocity model when the frequency of wall oscillation is 100 kHz under different wall motion modes. It can be observed that, except $G(\psi)$ which is considered to be significantly influenced by the external flow, the coefficients of the trigonometric terms introduced by the periodic LMUW motion exhibit a noticeable distribution trend in the near-wall region. These coefficients gradually decay to zero as ψ increases, indicating that the wall motion-induced flow has a great influence on the near-wall flow, which diminishes or even disappears with increasing ψ. Although $G(\psi)$ gradually approaches the external flow with the increasing ψ, in the boundary region, the velocity

distributions resulting from different LMUW modes are quite distinct. The distribution of these coefficients aligns with our conclusion in chapter 2 that the effect of LMUW wall motion is limited to the near-wall region without exert significant effect on the overall macroscopic flow field. Furthermore, it is clear that the velocity distribution is predominantly controlled by the lower-order terms, with high-order terms having a minimal impact on the overall velocity distribution.

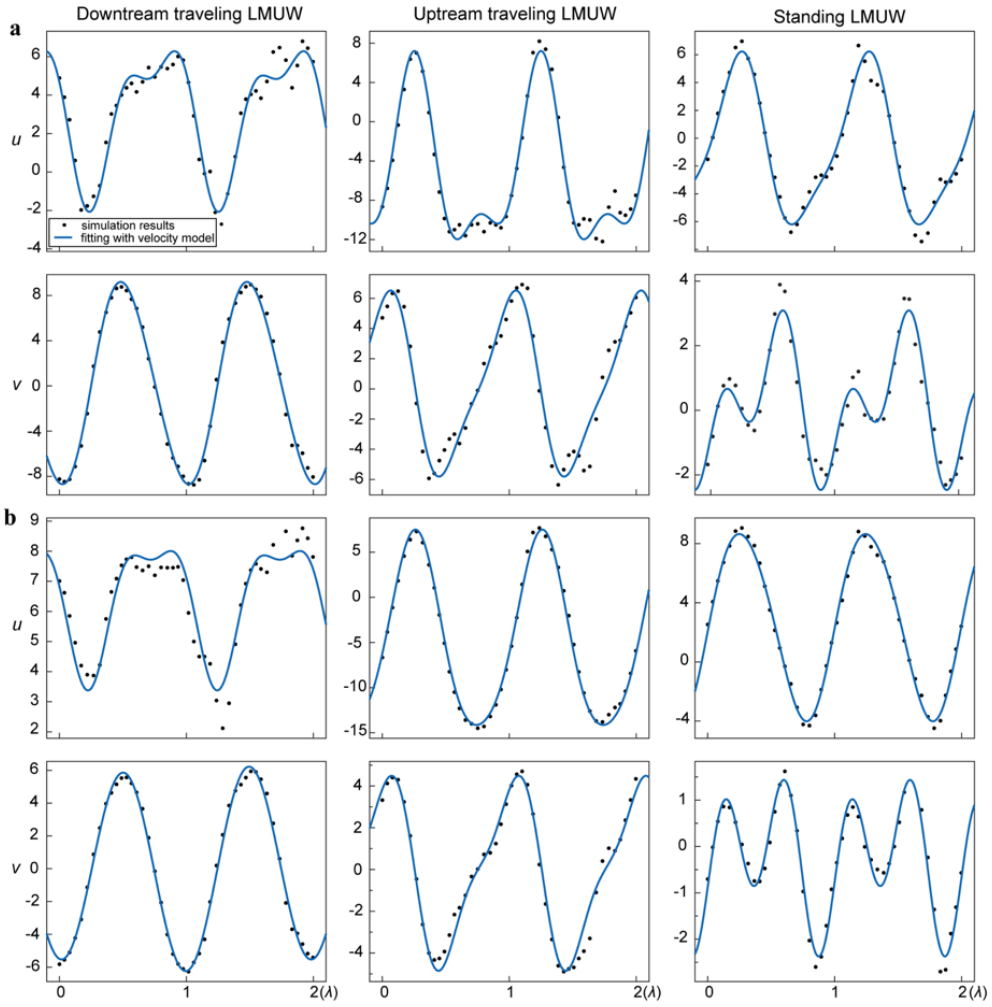

Figure 3-7 Validation of the velocity profile based on Fourier series

(a) ψ=0.004 mm at 0T when f=100 kHz; (b) ψ=0.01 mm at 0T when f=100 kHz

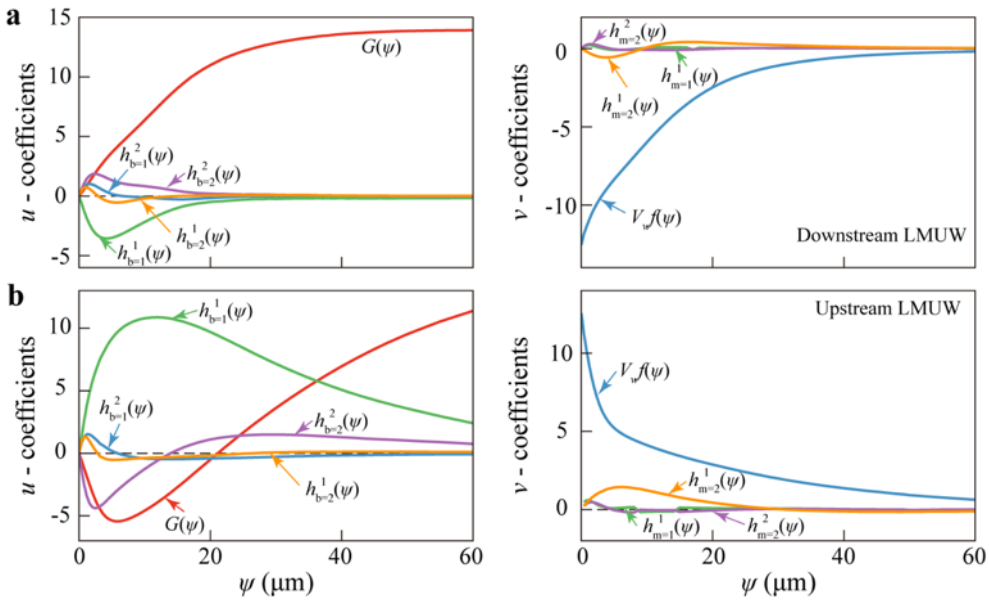

Figure 3-8 Coefficient functions of the velocity model for traveling LMUWs

(a) Downstream traveling LMUW; (b) Upstream traveling LMUW

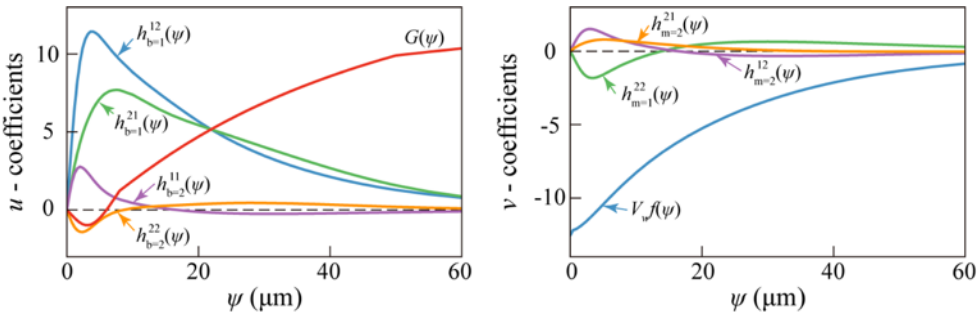

Figure 3-9 Coefficient functions of the velocity model for standing LMUWs

3.3 ESTABLISHMENT OF THEORETICAL MODEL

3.3.1 Traveling LMUWs

Given the coordinate transformation $\xi = x$, $\psi = y\text{-}y_w$, and $\tau = t$, where y_w is a function of position x and time t, the following relations can be obtained using the chain rule of partial differentiations:

$$\left.\begin{aligned}\frac{\partial}{\partial t} &= \frac{\partial}{\partial t} - \frac{\partial y_w}{\partial t}\frac{\partial}{\partial \psi} \\ \frac{\partial}{\partial x} &= \frac{\partial}{\partial \xi} - \frac{\partial y_w}{\partial x}\frac{\partial}{\partial \psi} \\ \frac{\partial}{\partial y} &= \frac{\partial}{\partial \psi}\end{aligned}\right\}. \qquad (3-15)$$

The continuity equation in the (x, y) coordinate system is

$$\frac{\partial u}{\partial x} + \frac{\partial v}{\partial y} = 0. \qquad (3-16)$$

Substituting equation (3-15) into (3-16) gives the following expression of continuity equation in the (ξ, ψ) coordinate system:

$$\frac{\partial u}{\partial \xi} - \frac{\partial y_w}{\partial x}\frac{\partial u}{\partial \psi} + \frac{\partial v}{\partial \psi} = 0\,. \qquad (3-17)$$

which will be used in the subsequent derivation process.

The first term of v in equation (3-10) expresses the attenuation of the normal wavy wall motion-induced vertical velocity due to fluid viscosity, as shown in figure 3-10(a). This has the same time-varying feature as the periodic wavy wall motion, although its amplitude decays rapidly with increasing vertical distance ψ [71]. Thus, the attenuation coefficient $f(\psi)$ shares the same profile as the vertical velocities within the undulation region and is solely a function of ψ. The attenuation of the vertical velocity amplitude V_w is defined by $V_w f(\psi)$, which is independent of the instantaneous wall variations, and is herein approximated by a simplified model, as shown in figure 3-10(b). A flow with a constant vertical velocity V_w is emitted from the flat lower boundary [$y_w = 0$, thus $\xi = x$, $\psi = y$ in the transformed coordinate system (ξ, ψ)]. Here, $v = V_w f(\psi)$ decays from V_w to 0 with increasing ψ. At this point, equation (3-17) can be reformulated as,

$$\frac{\partial u}{\partial \xi} + \frac{\partial v}{\partial \psi} = 0\,. \qquad (3-18)$$

Substitution of $v = V_w f(\psi)$ into the continuity equation leads to

$$\frac{\partial u}{\partial \xi} = -\frac{\partial v}{\partial \psi} = -V_w f'(\psi). \qquad (3-19)$$

Integrating this equation in the ξ direction, i.e.,

$$\int \frac{\partial u}{\partial \xi}\mathrm{d}\xi = \int -V_w f'(\psi)\mathrm{d}\xi\,, \qquad (3-20)$$

allows the u-component of velocity to be expressed by

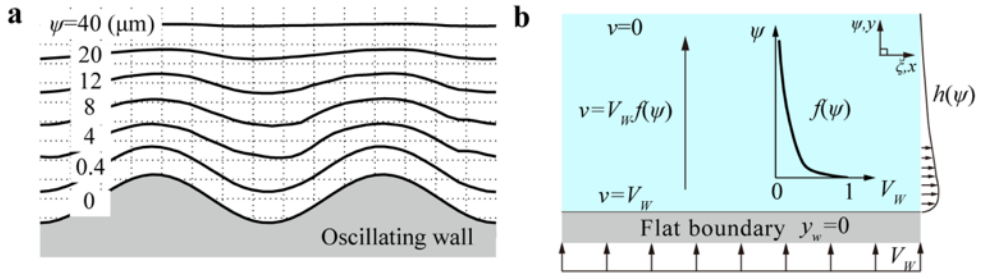

Figure 3-10 Determination of $f(\psi)$

(a) Sketch of attenuation in vertical velocity. (b) Simplified 2D model with attenuation coefficient function $f(\psi)$

$$u = -\xi V_w f'(\psi) + h(\psi), \qquad (3-21)$$

where $h(\psi)$ denotes an integration constant independent of ξ, representing the perturbation originating from the vertical velocity and fluid viscosity [figure 3-10(b)]. Then, substituting the u-components of velocity [equation (3-21)] and $v = V_w f(\psi)$ into the 2D incompressible, unsteady Navier–Stokes equation in the v-direction, i.e.,

$$\frac{\partial v}{\partial \tau} + u\frac{\partial v}{\partial \xi} + v\frac{\partial v}{\partial \psi} = -\frac{1}{\rho}\frac{\partial P}{\partial \psi} + \upsilon\left(\frac{\partial^2 v}{\partial \xi^2} + \frac{\partial^2 v}{\partial \psi^2}\right), \qquad (3-22)$$

we derive a differential equation associated with the pressure P:

$$\frac{\partial P}{\partial \psi} = \rho[\upsilon V_w f''(\psi) - V_w^2 f(\psi) f'(\psi)], \qquad (3-23)$$

And so

$$P = \int \rho[\upsilon V_w f''(\psi) - V_w^2 f(\psi) f'(\psi)]\mathrm{d}\psi + g(\xi), \qquad (3-24)$$

where $g(\xi)$ denotes an integration constant independent of ψ. Furthermore, substituting equation (3-21) and $v = V_w f(\psi)$ into the N–S equation in the u-direction, i.e.,

$$\frac{\partial u}{\partial \tau} + u\frac{\partial u}{\partial \xi} + v\frac{\partial u}{\partial \psi} = -\frac{1}{\rho}\frac{\partial P}{\partial \xi} + \upsilon\left(\frac{\partial^2 u}{\partial \xi^2} + \frac{\partial^2 u}{\partial \psi^2}\right), \qquad (3-25)$$

the following equation is obtained,

$$\xi V_w^2\left[\left(f'(\psi)\right)^2 - f(\psi)f''(\psi) + \frac{\upsilon}{V_w}f'''(\psi)\right]$$
$$-V_w\left[h(\psi)f'(\psi) - f(\psi)h'(\psi) + \frac{\upsilon}{V_w}h''(\psi)\right] + \frac{1}{\rho}g'(\xi) = 0. \qquad (3-26)$$

The first term in equation (3-26) is related to both ξ and ψ, while the second and third terms are only functions of ψ and ξ, respectively. To ensure that this equation holds at any location in the flow field under arbitrary V_w, each term must be equal to 0. Thus, an ordinary differential equation related to $f(\psi)$ can be derived as

$$[f'(\psi)]^2 - f(\psi)f''(\psi) + \frac{\upsilon}{V_w}f'''(\psi) = 0, \qquad (3-27)$$

Equation (3-27) only depends on the fluid viscosity υ and the vertical velocity V_w of the flat wall [figure 3-10(b)]; the attenuation coefficient function $f(\psi)$ always satisfies the conditions of $f(\psi) > 0$ and $f'(\psi) < 0$. The relationship between $f(\psi)$ and $h(\psi)$ can be written as

$$h(\psi)f'(\psi) - f(\psi)h'(\psi) + \frac{\upsilon}{V_w}h''(\psi) = 0, \qquad (3-28)$$

which provides a basic form for the first-order perturbation function $h_{b=1}^{1}(\psi)$ in equation (3-9).

The equation for $G(\psi)$, can also be derived by substituting the u- and v-components of velocity [equations (3-9) and (3-10)] in the (ξ, ψ) coordinate system and wall equation (2-1) into the continuity equation (3-17):

$$\begin{aligned}&\sum_{b=1}^{n} h_b^i(\psi)bk\cos\left[bk(\xi - c\tau) + \varphi^i\right] - kaG'(\psi)\cos[k(\xi - c\tau)]\\ &-ka\cos[k(x - c\tau)]\sum_{b=1}^{n} h_b^i{}'(\psi)\sin\left[bk(\xi - c\tau) + \varphi^i\right]\\ &+\sum_{m=1}^{n} h_m^i{}'(\psi)\sin\left[mk(\xi - c\tau) + \varphi^i\right] + (-kca)f'(\psi)\cos[k(\xi - c\tau)] = 0. \qquad (3-29)\end{aligned}$$

Combining the terms related to $\cos[k(\xi - c\tau)]$, we obtain

$$kh_{b=1}^{1}(\psi) - kaG'(\psi) + (-kca)f'(\psi) + h_{m=1}^{2}{}'(\psi) = 0, \qquad (3-30)$$

and thus,

$$G'(\psi) = -cf'(\psi) + \frac{1}{ka}\left[kh_{b=1}^{1}(\psi) + h_{m=1}^{2'}(\psi)\right]. \qquad (3-31)$$

which indicates that there exists a direct and explicit relationship between $G(\psi)$ and $f(\psi)$. The theoretical velocity model was validated through a comparison with the 2D RANS simulations. The distributions of coefficient functions [$h(\psi)$ and $f(\psi)$] shown in figure 3-8 for both upstream and downstream traveling LMUWs at f=100 kHz are used to calculate the theoretical wall-shear stresses according to equations (3-9) and (3-31). A comparison is presented in figure 3-11. The theorical model-based results (blue solid lines) are in excellent

agreement with the simulation results (orange dashed lines), thus verifying the validity of the established theoretical model for the LMUW-actuated dynamic boundary flow.

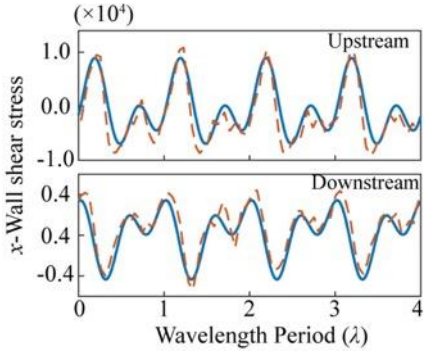

Figure 3-11 Validation of the theoretical model

3.3.2 Standing LMUW

Similar to the traveling LMUWs, we here also substitute the velocity profiles [equations (3-11) and (3-12)] of standing LMUWs into the continuity equation (3-17) in the (ξ, ψ) coordinate system. The following equation can be obtained:

$$\sum_{b=1}^{n} h_b^{ij}(\psi)\sin\left[b(2\pi f\tau)+\varphi^i\right](bk)\cos\left[b(k\xi)+\varphi^j\right]-kaG'(\psi)\cos(2\pi f\tau)\cos(k\xi)$$
$$+\sum_{m=1}^{n} h_m^{ij\prime}(\psi)\sin\left[m(2\pi f\tau)+\varphi^i\right]\sin\left[m(k\xi)+\varphi^j\right]+f'(\psi)(-2\pi fa)\sin(2\pi f\tau)\sin(k\xi)$$
$$-ka\cos(2\pi f\tau)\cos(k\xi)\sum_{b=1}^{n} h_b^{ij\prime}(\psi)\sin\left[b(2\pi f\tau)+\varphi^i\right](bk)\cos\left[b(k\xi)+\varphi^j\right]=0. \quad (3-32)$$

By combining the first-order terms including $[\cos(2\pi f\tau)\cos(k\xi)]$ and $[\sin(2\pi f\tau)\sin(k\xi)]$, the following equations are derived:

$$(-ka)G'(\psi)+kh_{b=1}^{21}(\psi)+h_{m=1}^{22'}(\psi)=0\,, \quad (3-33)$$

$$(-2\pi fa)f(\psi)-kh_{b=1}^{12}(\psi)+h_{m=1}^{11'}(\psi)=0. \quad (3-34)$$

Here, unlike the traveling waves, the terms of $G(\psi)$ and $f(\psi)$ under the standing wave condition do not exhibit a direct and explicit relationship. It can be inferred that the traveling LMUW-excited undulating wall motion generates an unchanged wavy wall configuration, inducing the near-wall dynamic boundary flow $G(\psi)$, which features wave propagation. However, in the absence of such propagation in standing waves, the near-wall flow is primarily driven by the normal motion, i.e., some disturbance due to the wavy wall

deformation.

3.4 THEORETICAL ANALYSIS OF DRAG REDUCITON

The second term $G(\psi)$ of u in equation (3-9) represents the incoming flow-induced, streamwise velocity components, and has the same physical meaning as the conventional boundary flow around a static flat plate [red line in figure (3-1)] [144]. According to Newton's friction law, the wall shear stress in the streamwise (x) direction can be written as:

$$\tau_w = \mu \frac{\partial u}{\partial \psi}\Big|_{\psi=0} = \mu \sum_{b=1}^{n} h_b^{i'}(\psi) \sin\left[bk(\xi - c\tau) + \varphi^i\right] + \mu G'(\psi)|_{\psi=0}. \qquad (3-35)$$

The periodic-averaged friction-drag coefficients is expressed as:

$$C_F = \frac{\int_0^T \int_0^L \tau_w \mathrm{d}\xi \mathrm{d}t}{0.5\rho U^2 LT} = \frac{\mu G'(\psi)}{0.5\rho U^2}\Big|_{\psi=0}, \qquad (3-36)$$

indicating that $G(\psi)$ is a crucial parameter that obviously dominates the wall friction force. As illustrated in equation (3-36), the wall friction force is highly correlated with $G'(\psi=0)$. In the near-wall region, when ψ approaches 0, $G(\psi)$ is dominated by the first term $-cf'(\psi)$ in equation (3-31), indicating that the wavy wall motion actuates a reversed flow [$G(\psi) < 0$], resulting in a negative friction drag, i.e., a thrust, under an upstream traveling wave ($c < 0$), or an enhanced streamwise flow [$G(\psi)>0$] under a downstream traveling wave ($c > 0$). This is completely consistent with the simulation results as shown in figure 2-6, verifying that this theoretical velocity model is capable of elucidating the underlying mechanisms associated with the LMUW-induced dynamic boundary flow and the relevant drag reduction.

According to equation (3-31), the wave-speed dependency of $G(\psi)$, $f(\psi)$, and $h_{b=1}^{1}(\psi)$ is now investigated by adjusting the wall undulation frequency (f = 10, 20, 50, 100, 200, 250 kHz) for the two traveling waves. We extracted the distributions of $G(\psi)$, $f(\psi)$, and $h_{b=1}^{1}(\psi)$ by fitting the simulation velocity data according to the theoretical velocity model [equations (3-9) and (3-10)] under different frequency conditions, as depicted in figure 3-12. Here, the distance from undulating wall ψ is normalized by by $\psi^+ = u_{ref}^* \psi/\upsilon$, where u_{ref}^* denotes the friction velocity of the flat plate wall. The distribution of $G(\psi)$, especially in the near-wall region, is quite different from the conventional flat plate boundary, and is highly sensitive to

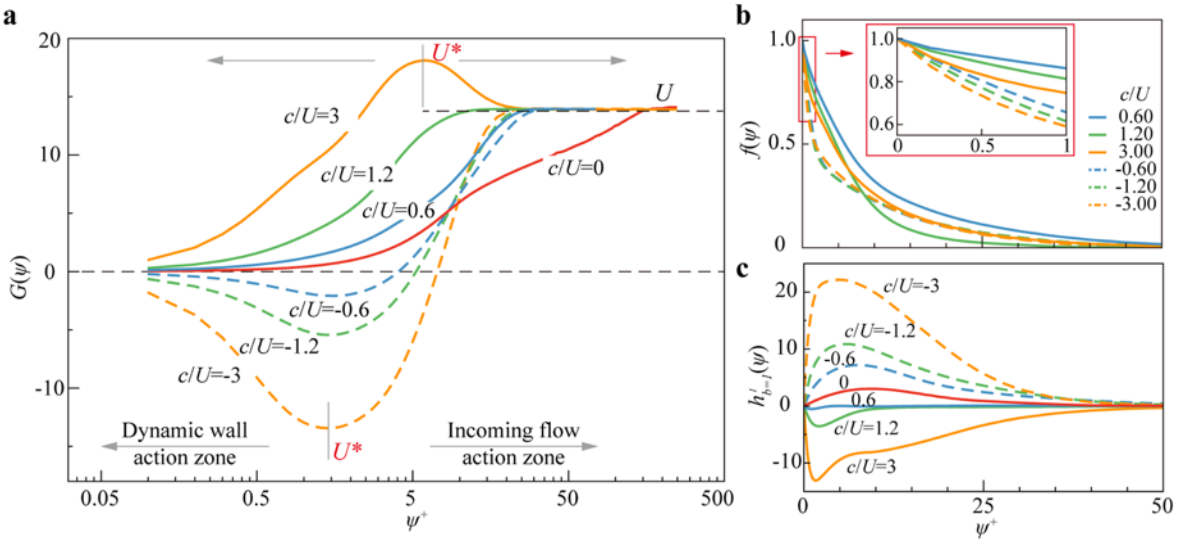

Figure 3-12 Coefficient function distributions under different wave speed

(a) $G(\psi)$; (b) $f(\psi)$; (c) $h_{b=1}^{1}(\psi)$

the wave speed. It can be observed that there exists a distinct turning point when $c/U < 0$ or $c/U > 1$, defined as U^*. U^* represents the wall motion-induced velocity peak, which varies with the wave speed, e.g., corresponding to different locations [for example, the gray lines at wave speeds of $c = 3$ or $c = -3$ in figure 3-12(a)]. Although no obvious turning point appears in the figure when c/U is between 0 and 1, the velocity U^* induced by the wall motion must exist. With U^* as boundary, the dynamic boundary layer can be divided into two regions: a dynamic wall action zone and an incoming flow action zone. In the dynamic wall action zone, the boundary velocity develops from 0 to U^*, primarily influenced by the wall oscillating motion. According to equation (3-36), the friction resistance is highly correlated with $G'(\psi=0)$, thus dominated by the velocity distribution in the dynamic wall action zone. $G'(\psi=0)$ is dominated by the first term, $-cf'(\psi=0)$ in equation (3-31). $f(\psi)$ is related to the vertical velocity amplitude $V_w(=-kca) \propto c$, which increases rapidly to 1.0 as ψ approaches 0. It exhibits significant wave-speed dependency, with the variation becoming more intense as $|c/U|$ increases shown in figure 3-12(b). Thus, $G'(\psi=0)$ varies monotonically from negative ($c < 0$) to positive ($c > 0$) with an increase in wave speed, corresponding to a monotonic increase in the friction-drag coefficient, as depicted in figure 3-13(a) and (b). As ψ increases, the wall motion (V_w)-induced flow attenuates, while the

streamwise incoming flow comes to exert a significant impact on the boundary flow. At this point, the boundary flow develops into the incoming flow action zone, in which the velocity varies from U^* to external flow velocity U. The variation in $G'(\psi)$ in the incoming flow action zone is consistent with the variation of $h_{b=1}^{1}(\psi)$ from positive to negative as c increases [figure 3-12(c)]. Interestingly, the pressure-drag coefficient also follows the same variation regularity, decreasing monotonically with increasing c [figure 3-13 (a) and (c)]. This indicates that the pressure drag is closely correlated with the variations of $G(\psi)$ in the incoming flow zone: a negative pressure drag is observed when $G'(\psi) < 0$ in this region.

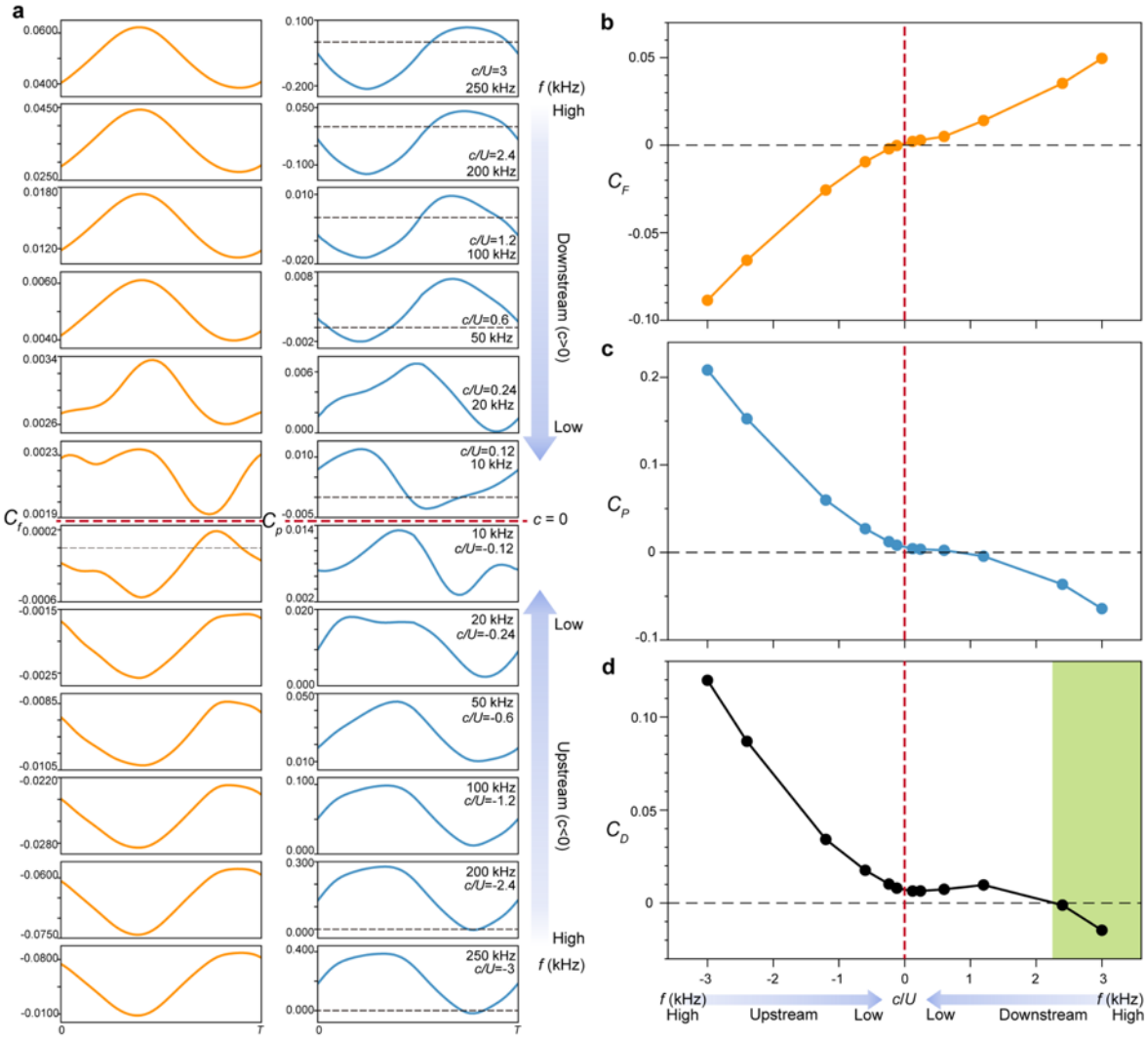

Figure 3-13 Distribution of drag forces under traveling LMUW conditions

(a) Instantaneous drag forces; (b) Time-averaged friction drag; (c) Time-averaged pressure drag; (d) Time-averaged total drag

From the above analysis, it is evident that $G'(\psi)$ plays a dominant role in determining both the friction- and pressure-based drag in terms of magnitude and direction. In the dynamic wall action zone, the friction drag is dominated by the LMUW motion-induced near-wall flow, while in the incoming flow action zone, the interplay between the wall motion-induced flow and the streamwise incoming flow determines the pressure drag, which is strongly associated with the multi-eddy motion in the sublayer of the LMUW-induced dynamic boundary layer. Unlike conventional methods of turbulent drag reduction, which aim to directly suppress the turbulent fluctuations as a means of reducing the drag magnitude, the LMUW-induced drag reduction strategy enables both the direction and magnitude of the friction- and pressure-based drag to be manipulated by tuning the wavy wall motion. The effect of this manipulation is to control the near-wall multi-eddy motions. Thus, the upstream LMUWs can produce a negative friction drag by inducing a near-wall reversed flow. Despite the upstream LMUWs having a significant advantage in reducing friction drag, it can be observed that pressure drag seems to dominate the total drag in the LMUW-induced flow, leading to an overall increase in total drag corresponding to the upstream flow. In contrast, the downstream LMUW has the ability to induce negative pressure drag, effectively reducing total drag and even converting it into thrust by propagating at a traveling wave-based downstream velocity (c) that is faster than the incoming flow velocity (U), as shown by the green shadow in figure 3-13(d).

The function $G(\psi)$ under the standing LMUWs in figure 3-14 displays a distinctly different distribution from that for the traveling LMUWs. The vortex in standing cases induce the reversed near-wall flow, leading to an obvious turning point U^*. With the U^* as

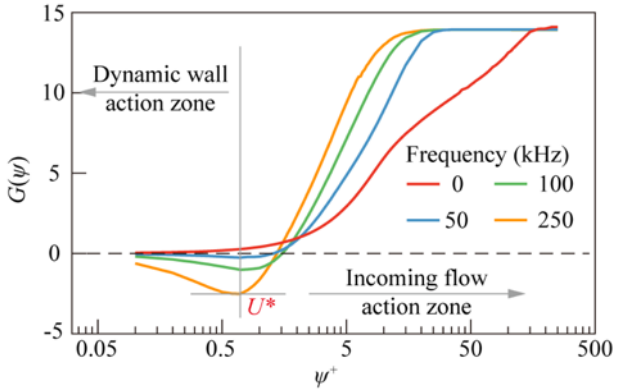

Figure 3-14 Variation of $G(\psi)$ in standing LMUW.

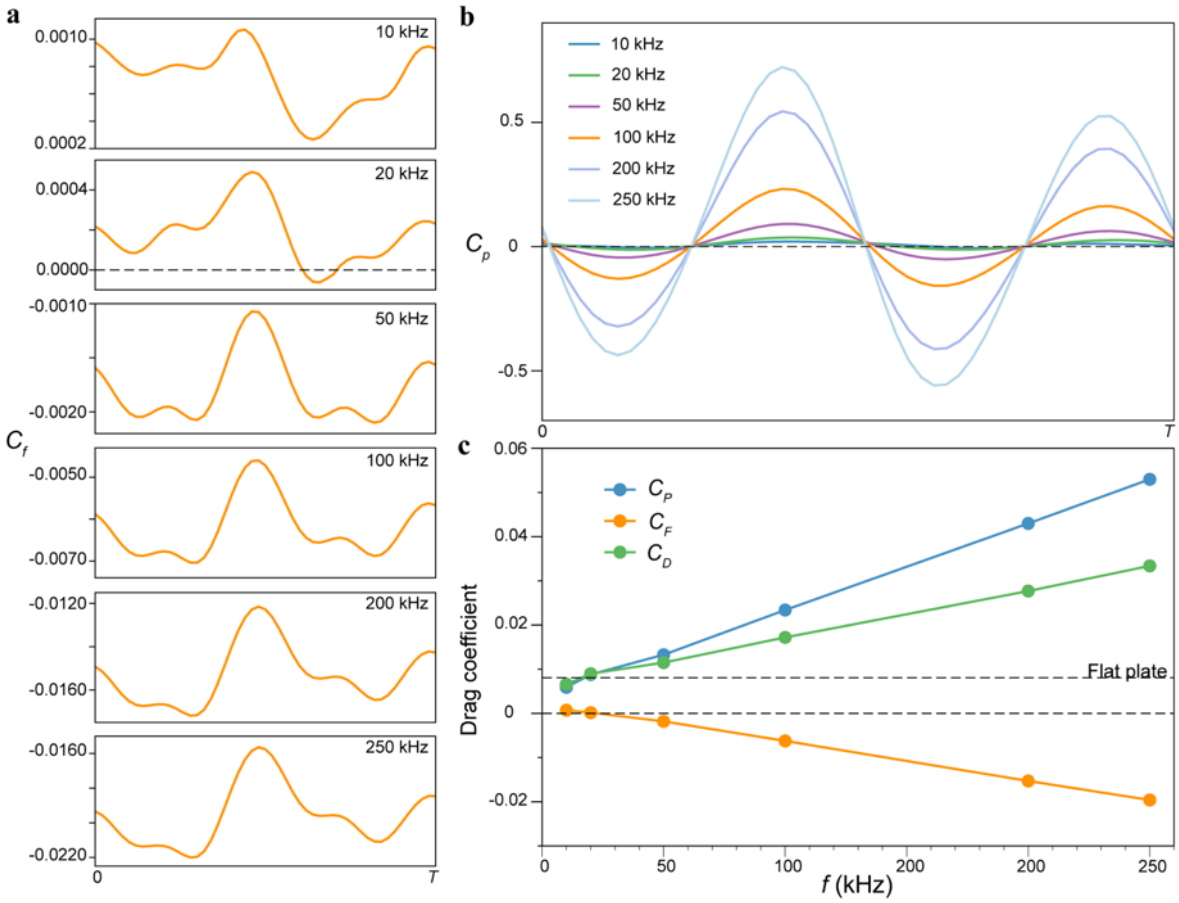

Figure 3-15 Distribution of drag forces under the standing LMUWs

(a) Instantaneous friction drag; (b) Instantaneous pressure drag; (c) Time-averaged drag forces

boundary, the velocity profile of standing LMUWs in the boundary layer can also be reasonably described in terms of the two-zone classification, dynamic wall action zone and incoming flow action zone, as in the case of traveling waves. The friction is determined by the velocity distribution in the dynamic wall action zone. Therefore, as the oscillation frequency increases, the reverse flow in the near-wall region becomes more intense, leading to the friction drag gradually decrease, as shown in figure 3-15 (a) and (c). Like the traveling waves, the incoming flow action zone still have a significant impact on the distribution of pressure. The pressure increases monotonically with frequency, which coincides with the behavior of function $G(\psi)$ in this region. But it is noteworthy that the peak of the instantaneous pressure drag fluctuations becomes more pronounced as f increases [figure 3-15(b)]. Despite this, the periodic fluctuations have little effect on the time-averaged pressure.

Thus, although the pressure drag shows a monotonic increasing trend, its degree of change is much smaller compared to the traveling waves. The small variations in both pressure and friction drag result in a limited change in the total drag, keeping it close to the drag acted on a flat plate, and the occurrence of negative drag seen in traveling cases does not appear here.

3.5 SUMMARY

In this chapter, inspired by the typical 2D periodic features on the *x*-*y* plane of the LMUW-induced dynamic boundary layer, we derived a theoretical model for the dynamic boundary layer based on a Fourier series expression of the velocities, which allow us to elucidate the underlying mechanisms in association with the LMUW-excited turbulent fluctuations and its correlations with friction and pressure drag reduction. A series of 2D RANS simulations based on *x*-*y* plane are used to support and validate the theoretical mode. And a theoretical analysis of the drag reduction mechanism under dynamic wall condition was conducted. The main findings are summarized as follows:

(1) A theoretical model for the velocity profile of the dynamic boundary flow was shown to be capable of reasonably capturing the essential fluid flows and analytically correlating the LMUW-excited near-wall turbulent flow with the friction- and pressure-drag reduction. The theoretical model reveals that variations in an analytical function $G(\psi)$ [also the mean velocity of u] plays a dominant role in determining both the friction and pressure drag. It highly correlated with wall motion modes, showing a significant difference from the traditional flat plate boundary layer. The LMUW-induced dynamic boundary can be divided into two regions according to the distribution of $G(\psi)$: dynamic wall action zone and incoming flow action zone, which separately control the friction drag and pressure drag. More importantly, both the direction and magnitude of $G(\psi)$ can be manipulated by tuning the wavy wall motion, allowing the variations on both the direction and magnitude of the friction- and pressure-based drag to achieve drag reduction. The mechanism induced by the LMUW drag reduction strategy is quite different from conventional drag-reduction methods that directly suppress turbulent fluctuations.

(2) As Fourier series are employed in the establishment of boundary velocity model, its extensive inclusiveness allows this velocity model to describe not only the high-frequency,

micro-amplitude wall motions mentioned here but also more complex wall movements. Additionally, by using Fourier series to describe the flow perturbations within the boundary layer, the model can capture both the periodic flow variations induced by the periodic motion of the wall and the chaotic turbulent fluctuations present in turbulent flows. This makes the theoretical model broadly applicable to boundary layer flows.

These results demonstrated that the LMUW-excitation provides a novel active flow control strategy for the effective manipulation of the multi-eddy motions and velocity profiles within a confined zone near the wall surface, hence resulting a remarkable reduction and possible extinguishment of the friction and pressure drag. The analytical model provides theoretical guidance for various LMUW-based active turbulent flow control approaches under conditions relevant to actual engineering systems and offers new insights into the sophisticated drag-reduction mechanisms in association with Gray's paradox in dolphin swimming.

Chapter 4 APPLICATION OF LMUW WALL MOTION ON STREAMLINED BODY

4.1 INTRODUCTION

We have known from the previous chapters that the LMUW-induced drag reduction strategy inspired by dolphin skin enables manipulating both direction and magnitude of both friction and pressure-based drag. This exploration offers a novel drag reduction mechanism and a new perspective, based on a dynamic boundary, on investigating the mystery of the excellent hydrodynamic performance of dolphins. Certainly, as a biological organism, the high-speed swimming and low resistance of dolphin is undoubtedly the result of the combined influence of multiple factors. Based on previous research [95,96], we also understand that the streamlined shape of dolphin contributes greatly to its excellent performance which can provide some advantages on delaying flow separation near the trailing edge and maintaining a laminar boundary flow. Therefore, we hope to combine the two factors of streamlined shape and the dynamic skin boundary driven by LMUWs to explore the synergistic effects on the drag reduction of dolphin.

In addition, the streamlined shape learned from biology is a highly efficient lifting shape, capable of generating more lift than similar sized flat plates of the same area with significantly less drag. And thus, the streamlined shape, which is called 'foil' in engineering, is widely used in the design of aircraft, watercraft, propellers, rotor blades and other applications. Due to the wide applications of airfoil, the enhancement of its dynamic performance is of great significance in improving efficiency and decreasing energy consumption and have a considerable engineering value [1,145–147]. And drag reduction, as an important way to enhance airfoil performance, has always been a popular research topic and attracts great interest in fluid mechanics research. Previous studies concentrate on the shape optimization, fabricating microstructure (grooves or riblets) on airfoil surface by learning from shark skin and use of oscillatory blowing/suction to delay flow separation and achieve

drag reduction [148–156]. Here, considering the great potential and new mechanism in drag reduction provided by LMUW inspired by dolphin, we are also greatly interested in how the dynamic boundary by adding the LMUW can affect the airfoil performance including drag, lift and lift-to-drag ratio.

Focus on the two key issues, in this chapter, we attempt to apply the LMUW to the airfoil surface. Through establishing a series of numerical simulations based on streamlined shape and surface LMUW addition, the airfoil performance, including lift, drag and lift-to-drag ratio, are investigated. Different combination forms are performed to provide some optimal design inspirations for the improvement of airfoil performance.

4.2 2D AIRFOIL MODEL WITH LMUW

4.2.1 Physical problem

Motivated by the results in chapter 2, which found that LMUW-actuated, wall-bounded turbulent boundary layers are characterized by 2D flow structures in the streamwise and vertical directions, with minimal spanwise flow, we employed a 2D airfoil model to investigate the essential flow physics and underlying mechanisms associated with LMUW-induced aerodynamic performance. We computationally studied turbulent flows around a typical NACA0012 airfoil with various combinations of LMUW actuations on the upper and/or lower surfaces of the airfoil at a constant Reynolds number, across a broad range of angles of attack (AoAs). The region where the wall oscillation occurs is defined as vibration region, as shown in figure 4-1. In these simulations, the vibration region on the airfoil surface undergoes vertical oscillations in the form of a traveling wave, such as:

$$y_{w-tr} = y + a\sin[k(x - ct)], \qquad (4-1)$$

or a standing wave, expressed by:

$$y_{w-st} = y + a\sin(kx)\cos(2\pi ft), \qquad (4-2)$$

where y is the original coordinates of the airfoil surface, the oscillation parameters of LMUW is consistent with the 3D simulations in chapter 2 (λ= 150 μm; a=20 μm; f=100 kHz). Substantially, the wavy wall surface of the vibration region performs an up-down oscillation with the velocity components (u and v) in x- and y-directions as,

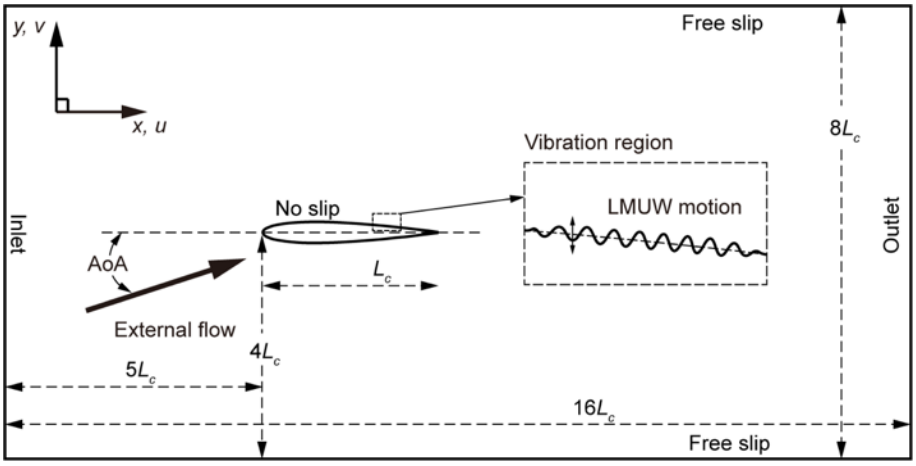

Figure 4-1 Sketch of the airfoil model with LMUW

$$\left.\begin{aligned} u_w &= 0 \\ v_{w-tr} &= (-kca)\cos[k(x-ct)] \\ v_{w-st} &= (-2\pi fa)\sin(kx)\sin(2\pi ft) \end{aligned}\right\}. \qquad (4-3)$$

The external flow, as in the 3D simulation, has a velocity of 12.5 m/s. Therefore, as verified in chapter 2, despite the ultrasonic frequency of LMUW, the flow is still considered incompressible since the Mach number is much less than 0.3. The chord length of the airfoil L_c is 100 mm. And the *Re* of the overall flow field defined as $Re=UL_c/\upsilon$ with υ the kinematic viscosity of water is calculated as 1.24×10^6.

4.2.2 Numerical settings

The CFD modeling of turbulent flows around the airfoil was performed using ANSYS Fluent 16.0. As indicated in figure 4-1, the computational domain is $16L_c$ long and $8L_c$ wide, with the inlet, outlet and side boundaries located $5L_c$, $10L_c$ and roughly $4L_c$ away from the airfoil, respectively. This domain was confirmed to be sufficiently large for accurate turbulence simulations. While both LES-based and RANS (SST *k*-*ω*)-based modeling were considered for turbulence simulations, RANS modeling was ultimately employed for all simulations, balancing numerical accuracy with computational time. As extensively validated in chapter 3, RANS (SST *k*-*ω*) modeling effectively simulates turbulent flows over LMUW-actuated oscillating wavy surfaces, accurately capturing near-wall flow structures and estimating forces of pressure and shear stress, in terms of a 3D open channel model at the same Reynolds number. Here, considering the differences in the shapes of flat plate and

airfoil, we further investigated whether these findings hold true for the airfoil model, with a $0.1L_c$ vibration unit deployed at [$0.8L_c$, $0.9L_c$] on the upper surface. As shown in figure 4-2(a), we introduce a thickness ($0.05L_c$, half the length of the basic vibration unit $0.1L_c$) in the spanwise direction to the 2D computational domain to conduct the comparison simulations. The near-wall velocity distributions [figure 4-2(b)] were consistent between the LES and RANS (SST $k-\omega$) models, and the instantaneous lift and drag forces [figure 4-2(c)] were quantitatively comparable to those predicted by the LES model.

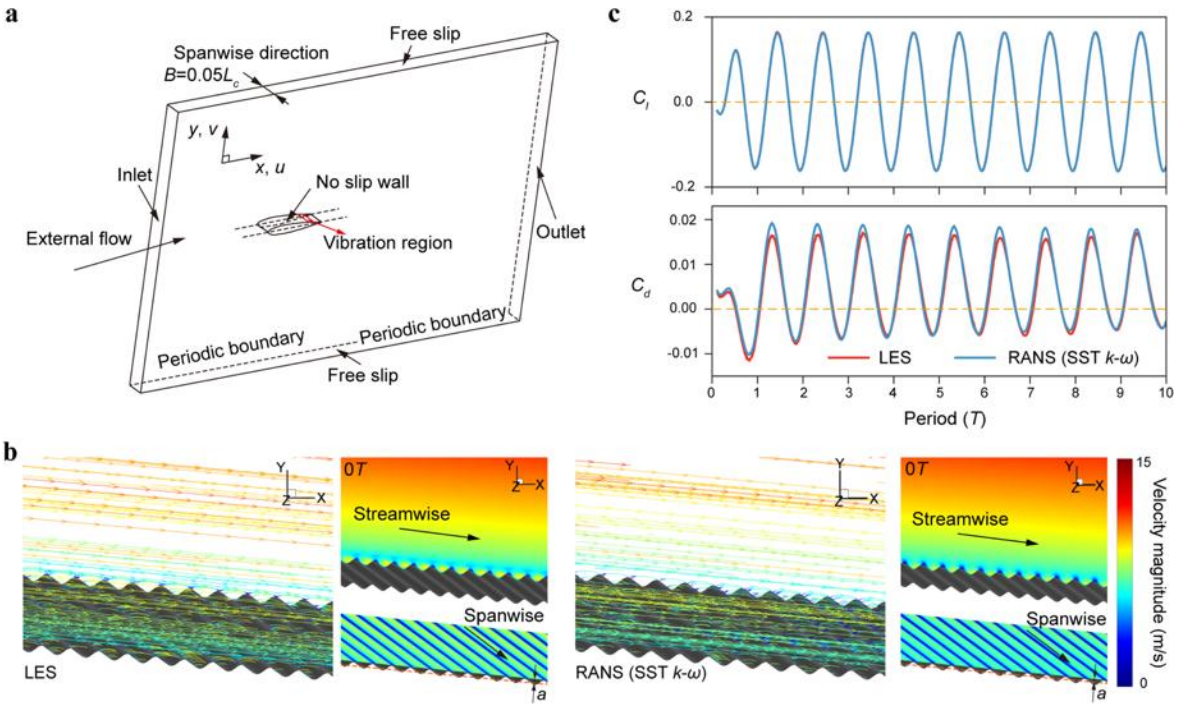

Figure 4-2 Validation of RANS (SST k-ω) model

(a) Sketch of computational domain; (b) Near-wall flow structures; (c) Distribution of lift and total drag

The boundary conditions are imposed including a freestream inflow velocity at the inlet, free outflow condition at the outlet, no-slip boundary condition on the airfoil surface and free-slip condition at the top and bottom boundary. Simulations were initially conducted on the airfoil model without an oscillating wall surface to ensure a fully developed turbulent flow across the entire flow field. Once this baseline was established, single or multiple vibration regions were then subjected to LMUW actuations, applied in the following form:

$$\left.\begin{aligned} y_{w-tr} &= y + a\sin[k(x-ct)]G(t)F(x) \\ y_{w-st} &= y + a\sin(kx)\cos(2\pi ft)G(t)F(x) \end{aligned}\right\}, \quad (4-4)$$

Here the definition of $F(x)$ and $G(t)$ is same as that mentioned in chapter 2. The dynamic mesh model in Fluent was employed to update the computational grids in response to the wavy wall motion, with a time step of $T/100$, which was confirmed to be sufficient for smooth dynamic remeshing of the computational domain. All simulations were run for up to 20 vibration cycles, allowing the flow to converge to a stable, fully developed turbulence.

4.2.3 Verification and validation

A C-type mesh was employed with more than 100 grids clustered to the airfoil surface. The height of the first mesh layer adjacent to the wall surface was set to 0.002 mm to guarantee $y^+ \approx 1$. An evenly spaced grid with 4140 nodes (Grid 1 in table 4-1) was initially used in the streamwise direction along the airfoil surface. In order to ensure an adequate mesh and effective computational methods, we initially utilize this mesh and boundary settings to compute the lift coefficient C_L and drag coefficient C_D acting on the airfoil under the condition with a Reynolds number of 1.0×10^6. Here, the overall lift and drag coefficients can be expressed as:

$$C_L = \frac{F_L}{0.5\rho U^2 L_c} \text{ and } C_D = \frac{F_D}{0.5\rho U^2 L_c}, \quad (4-5)$$

where F_L and F_D are the overall lift and drag acting on the airfoil. And then, a refined evenly spaced grid with 5856 nodes on airfoil surface (Grid 2) is also provided. Force results under the two grids presented in table 4-2 have been compared and the difference is found to be negligible, indicating that Grid 1 is sufficiently effective in monitoring the overall forces acting on the foil. Simulations of the turbulent flows around the airfoil without vibration were also validated by comparing the lift (C_L) and drag (C_D) coefficients from the current simulations using Grid 1 with previous CFD results [157] and NASA measurements [158,159] across AoAs from 0° to 18°. As shown in figure 4-3(a), a favorable consistency can be obtained, especially under small AoAs. Additionally, local pressure distributions on the airfoil surface were compared between the current simulations (Grid 1) and experimental results [160,161] at AoAs of 0°, 10°, and 15°, shown in figure 4-3(b). Excellent agreement was obtained in both comparisons. It is important to note that while a stall was observed in the experiments at AoA = 12°, it was not captured in the simulations, indicating that the

simulations may not accurately represent large-scale flow separations during airfoil stall. Therefore, the simulation results at AoAs ≤ 10° are used in the subsequent analysis and discussion.

Table 4-1 Grid information for verification of mesh independence

	Grid	Nodes on foil surface (on the oscillation region $0.1L_c$)	Grid quantity
Evenly spaced grid on airfoil surface	Grid 1	4140	2249043
	Grid 2	5856	2864433
Locally refined grid in vibration region	Grid 3	5450 (600)	2678274
	Grid 4	6340 (900)	2984879

Table 4-2 Comparison of C_L and C_D under different AoAs in the case of Grid 1 and Grid 2

AoA(°)	C_L			C_D		
	Grid 1	Grid 2	Differ	Grid 1	Grid 2	Differ
0	0	0	0	0.010671	0.010718	0.44%
7.5	0.805498	0.806071	0.07%	0.014371	0.014498	0.88%
17	1.468810	1.479038	0.70%	0.054724	0.054823	0.18%

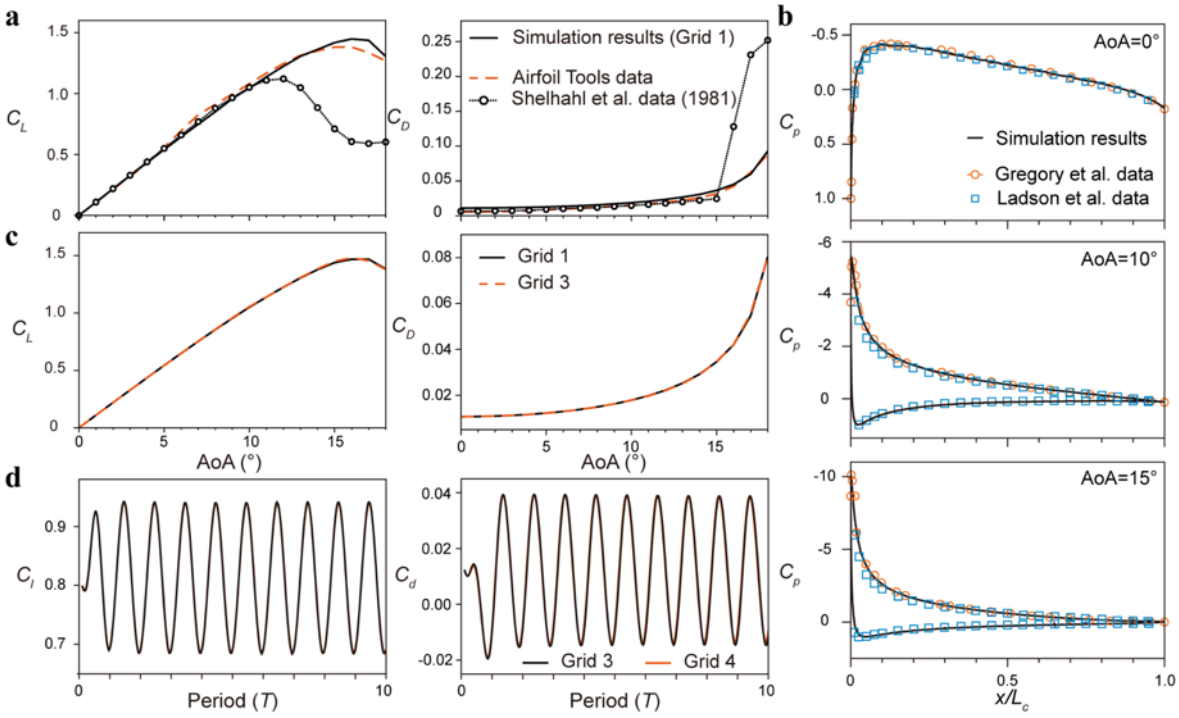

Figure 4-3 Validation and verification

(a) Distributions of overall lift and drag coefficients; (b) Local pressure distributions; (c) Mesh independence between Grid 1 and Grid 3; (d) Instantaneous lift and drag coefficients corresponding to Grid 3 and Grid 4

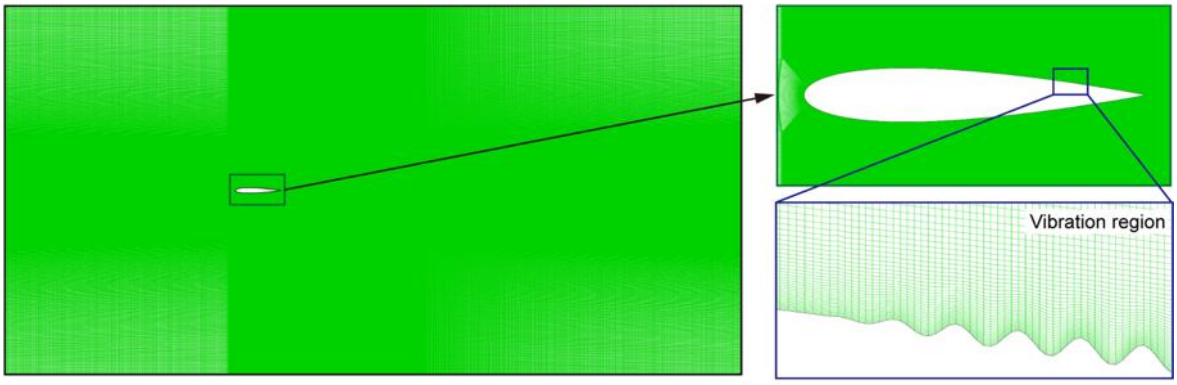

Figure 4-4 Grid system

Furthermore, when the wall LMUW motion is added on the airfoil surface, the grid in the vibration region must be refined due to the small oscillation wavelength. Thus, we perform Grid 3 based on Grid 1 to locally refine the mesh in vibration region and compare C_L and C_D with the results of Grid 1 in figure 4-3(c). And a more refined Grid 4 within the vibration region is also established to verify the mesh independence in capturing instantaneous forces (C_l and C_d) when adding wall oscillation on the airfoil surface at [$0.8L_c$, $0.9L_c$] at AoA=7.5° [figure 4-3(d)]. All the difference in the comparison cases is small and it can be concluded that Grid 3, as shown in figure 4-4, is sufficiently effective to provide a grid-independent solution and thus used in the following simulation work.

4.3 IMPACT OF LMUW FORMS ON AIRFOIL PERFORMANCE

We take $0.1L_c$ as a motion unit and firstly set the position of vibration region [x_s, x_e] is [$0.8L_c$, $0.9L_c$] on the upper surface of the airfoil, shown in figure 4-5. Figure 4-6 displays the contours of pressure and velocity magnitude corresponding to different cases of no-vibration,

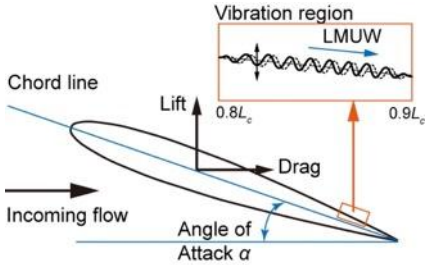

Figure 4-5 Vibration region

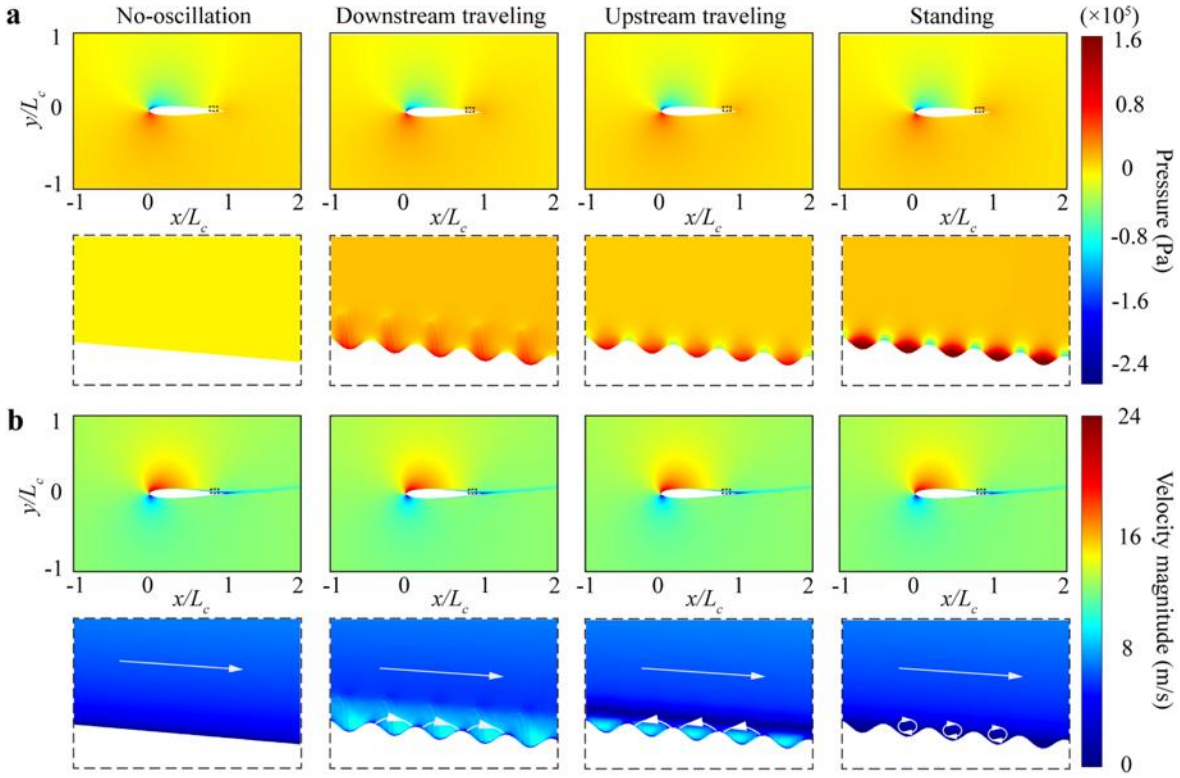

Figure 4-6 Color plot of flow field distribution at 0T

(a) Pressure distribution; (b) Velocity magnitude distribution

downstream traveling, upstream traveling and standing LMUWs when AoA is 7.5º. Compared to the non-oscillating condition, the addition of wall LMUW results in significant pressure changes along the wall and in the nearby flow field. The pressure variations near the wall radiate into the flow field around the vibration region, causing certain pressure fluctuations, as illustrated in figure 4-6(a). The near-wall pressure distribution strongly depends on the wall LMUW motion forms. We extract the pressure force (normalized by $0.5\rho U^2$) acted on the oscillating surface under different LMUW conditions, as depicted in figure 4-7(a). It is observed that the pressure fluctuation corresponding to the downstream traveling LMUW is smallest in the three LMUW forms, and the pressure peak in standing LMUW is significantly higher than that of traveling waves. Although the pressure variations inevitably bring about lift fluctuations on the foil, the overall pressure distribution trend of the flow field around the foil is not altered by wall motion. And the high- and low-pressure regions near the leading edge of the foil, mainly responsible for providing lift, remain

unaffected. Thus, the lift fluctuations introduced by adding wall LMUW motions are nearly symmetrical about the lift under the original non-oscillating conditions [figure 4-7(c)]. The periodic averaged lift shown in figure 4-8(a) can also verify that the overall lift on the airfoil is relatively unchanged before and after adding the wall LMUW motion. However, the impact of pressure fluctuation on the pressure drag cannot be ignored. As shown in figure 4-8(b), the addition of LMUW results in a significant change in pressure drag compared to the no-oscillation condition, and this change is highly correlated with the form of wall motion. The pressure drag can be reduced in the case of downstream LMUW but increase under upstream traveling LMUW. And although the standing LMUW has the strongest pressure fluctuation, the corresponding time-averaged pressure resistance is very close to the no-oscillation case due to the periodicity of the fluctuations.

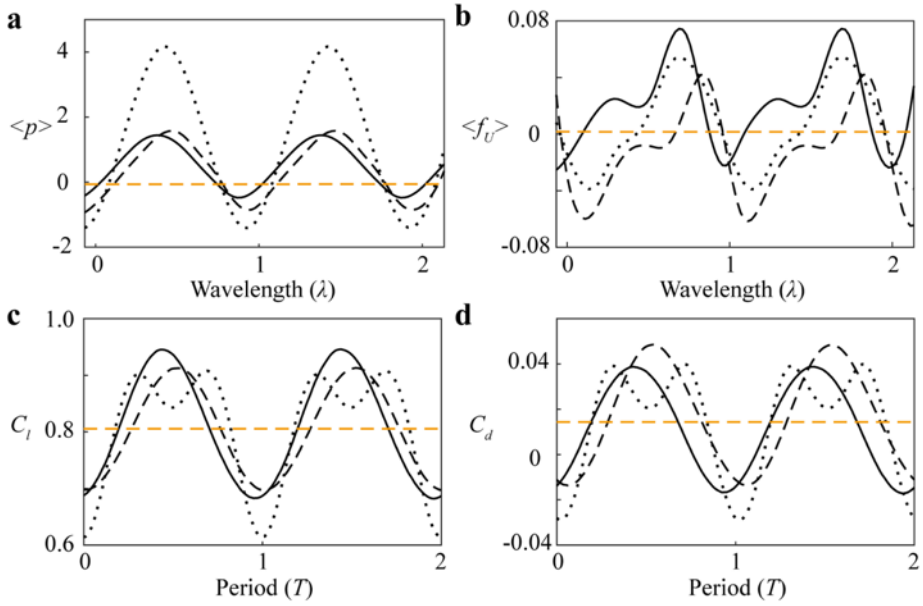

Figure 4-7 Force distributions

(a) Local pressure; (b) *U*-direction friction force; (c) Instantaneous lift; (d) Instantaneous drag

As mentioned in previous chapter, due to the high-frequency and micro-amplitude characteristics of LMUW, its influence on boundary flow is confined to the near-wall region, especially in the viscous sublayer of turbulent boundary layers, without significantly affecting the overall flow field. This result can also be verified here, as shown in figure 4-

6(b), where the global flow velocity distribution in the four cases is nearly identical. However, there are noticeable differences in the boundary flow structures due to the different forms of wall motion. For the cases of traveling LMUWs, due to their propagative nature, the near-wall fluid can be induced to move as the waves propagate, resulting in the formation of downstream high-speed flow (same direction as external flow) and reversed high-speed flow (opposite direction to external flow) at the wave trough region under the condition of downstream and upstream traveling LMUW, respectively. The flow direction of the fluid near the wall determines the direction of wall shear stress. Figure 4-7(b) plots the U-direction wall shear stress (normalized by $0.5\rho U^2$) on the oscillating surface for different cases, revealing that the negative shear stress dominates most of the wavelength period under upstream LMUW conditions. This is helpful to induce negative friction force which shows the thrust effect, thereby reducing friction resistance. In contrast, the downstream flow induced by the oscillating wall in form of downstream traveling LMUW plays a more significant role and leads to a higher velocity gradient and larger friction drag. We also calculate the time-averaged friction force acting on the entire foil shown in figure 4-8(c). It can be seen more clearly that the friction drag always decreases in the case of upstream traveling LMUW but increases in downstream LMUW due to the different wave propagation direction. The near-wall flow in standing LMUW is more complex than traveling cases due

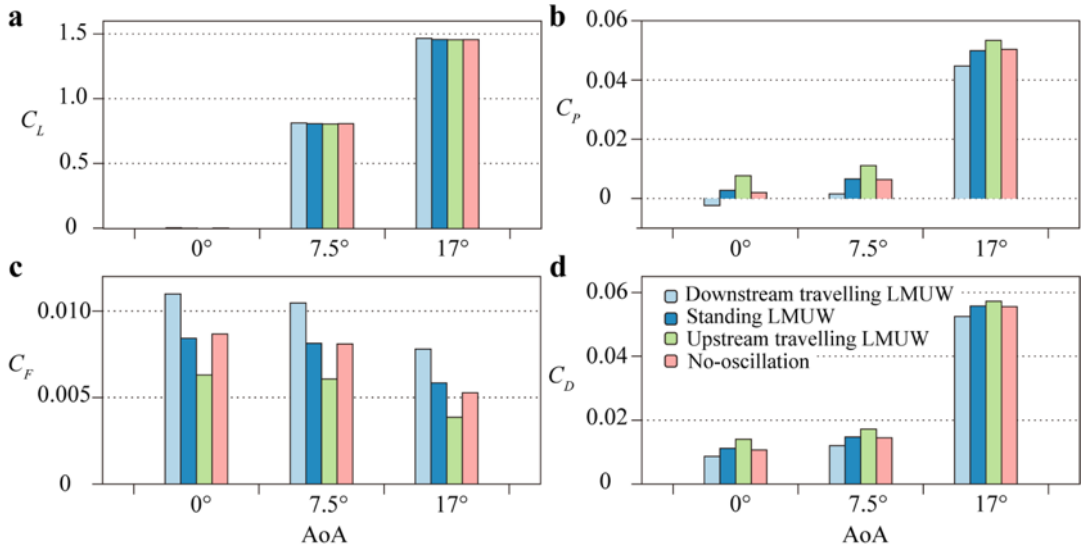

Figure 4-8 Overall forces acting on the airfoil

(a) Lift; (b) Pressure drag; (c) Friction drag; (d) Total drag

to the variation of wall shape in a period. But because standing waves lack propagative characteristic, they cannot drive near-wall fluid to move with wave propagation as traveling cases. Therefore, the flow at the trough does not exhibit clear directionality; instead, it features near-wall vortex [figure 4-6(b)], similar to the flow near a stationary wavy surface. Although the presence of these near-wall vortex can induce reverse flow close to the wall, generating a certain negative stress indicated in figure 4-7(b), this effect is significantly smaller than that induced by upstream LMUW. Consequently, in comparison to traveling LMUW, the impact of standing LMUW on the overall time-averaged friction drag is very limited [figure 4-8(c)].

Different forms of wall LMUW motion have varying manipulation effects on the distribution of forces on the wall, either reducing pressure resistance or friction resistance. In figure 4-7(d), the distribution of total drag over one cycle is presented, taking into account the combined effects of pressure and friction force and revealing that the downstream traveling LMUW (DTLMUW) have a greater advantage in reducing total drag compared to the other two cases [figure 4-8(d)]. Based on this advantage, we also extracted the local pressure and wall shear stress acting on the whole airfoil over one vibration period at AoA=7.5º under downstream traveling LMUW (figure 4-9). The presence of wall vibration causes substantial changes in forces on the airfoil surface, which, however, are confined within the vibration region. The DTLMUW-induced C_p distribution in the vibration region generates a local pressure-based forward force, i.e., a thrust on the time-varying wavy vibration region while having a minimal impact on the vertical force (lift) production. This phenomenon is analogous to the undulating swimming motion in fish, where a downstream traveling wave with large amplitude and low frequency is typically recognized for generating a pressure-based thrust that primarily counters friction-based drag [121], which however is observed here in terms of the microscale undulating strategy capable of effectively reducing drag acting on the airfoil. Additionally, the DTLMUW-induced C_f distributions in the vibration region result in an increase in local friction-based drag due to the enhanced streamwise flows, which also has little effect on lift production. Consequently, compared to the non-vibration case, a significant reduction (-15.88%) in the time-averaged total drag coefficient (C_D), which includes both pressure (C_P) and friction (C_F) drag components, is achieved by adding downstream traveling LMUW with only a minor increase (+0.56%) in

the time-averaged lift coefficient (C_L). This leads to a substantial improvement (+19.54%) in the time-averaged lift-to-drag ratio (C_L/C_D) (figure 4-10). Here, these percentages represent the variation rate in force, which is defined as:

$$\text{Variation Rate} = \frac{C_{vib} - C_{novib}}{C_{novib}} \times 100\%, \qquad (4-6)$$

where C_{vib} and C_{novib} represent time-averaged drag (C_D) or lift (C_L) coefficient or lift-to-drag ratio (C_L/C_D) with and without the vibration, respectively.

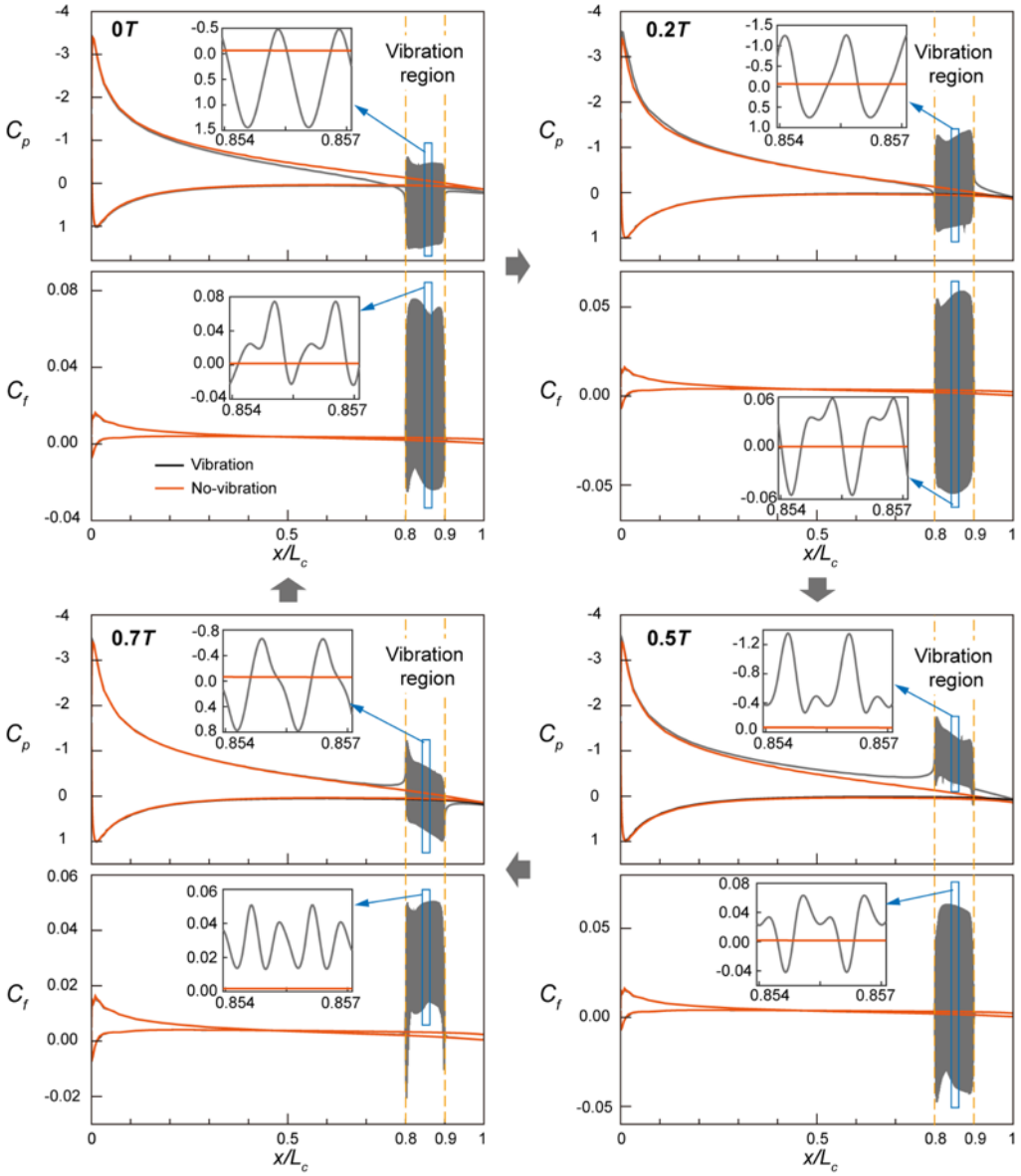

Figure 4-9 Local pressure and wall shear stress distributions under DTLMUW at AoA = 7.5°

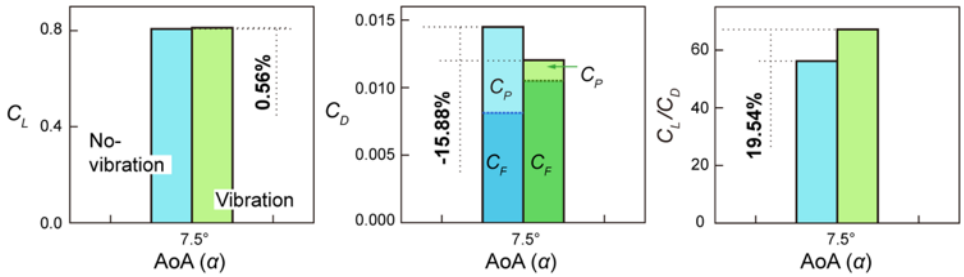

Figure 4-10 Variation rate of drag forces

The pattern of lift ang drag variations caused by wall motion remains applicable under different AoAs, such as when AoA are 0º and 17º shown in figure 4-8, indicating that the influence of wall motion forms on forces is independent of AoA. Downstream traveling LMUW can effectively achieve total drag reduction under various AoA conditions. And thus, we focus on applying the downstream traveling LMUW (DTLMUW) as the wall oscillation method to do the further research in the following content.

4.4 EFFECT OF AOA ON AIRFOIL MODEL WITH DTLMUW

The addition of wall oscillation in the form of DTLMUW is helpful to achieve a reduction in total drag on the airfoil. A change of AoA in a small range will not alter this conclusion but will affect the strength of drag reduction. In this section, we present the results with a focus on the impact of AoA variation on the drag reduction effect. Here, we also take $0.1L_c$ as a motion unit and set the vibration region $[x_s, x_e]$ is $[0.8L_c, 0.9L_c]$. And we define the single vibration when the DTLMUW only occurs on the upper surface and double vibration when there exist the same wall DTLMUW motions on both upper and lower surfaces of airfoil, as indicated in figure 4-11. As mentioned in figure 4-3(a), the experiment detected that stall occurs at AoA=12°, but this phenomenon was not captured in the simulations, indicating that the simulations may not accurately represent large-scale flow separations during airfoil stall. However, under small AoA conditions (AoAs ≤ 10°), the simulation results can match well with the experimental results, showing high accuracy. In this section, we calculated the force data for an AoA range 0° to 18° at 1° intervals. Although we will provide data for all AoAs in this section, considering the limitations of simulations

at high AoAs, we believe that the results are accurate when AoAs ≤ 10°. This region is indicated with a green shade in the subsequent figures in this section.

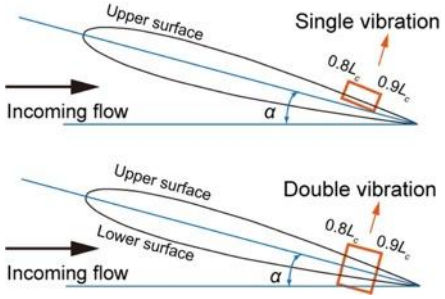

Figure 4-11 Schematic of two vibration arrangements

As analyzed above, although wall LMUW motion induces a force fluctuation, the symmetry of the fluctuation with respect to the non-oscillating lift minimizes their impact on the overall time-averaged lift. Thus, the lifts corresponding to single and double vibration are both basically consistent with the force in the case of no-oscillation [figure 4-12(a)] for all the AoAs shown here. However, the drag always decreases. As illustrated in figure 4-12(b), the drag in the two vibration cases remains consistently lower than the original non-oscillating state, and the extent of drag reduction increases with the expansion of the vibrating area. This implies that the increase of oscillation area enables more drag reduction effect without compromising the overall lift, which provides significant inspiration for the design of reducing drag and improving performance of airfoil. Additionally, due to the unchanged lift but decreased drag, the corresponding lift-to-drag ratio also increase after adding the DTLMUW motion. But the AoA at which the maximum lift-to-drag ratio occurs tends to decrease with the increase of the oscillation area (figure 4-13).

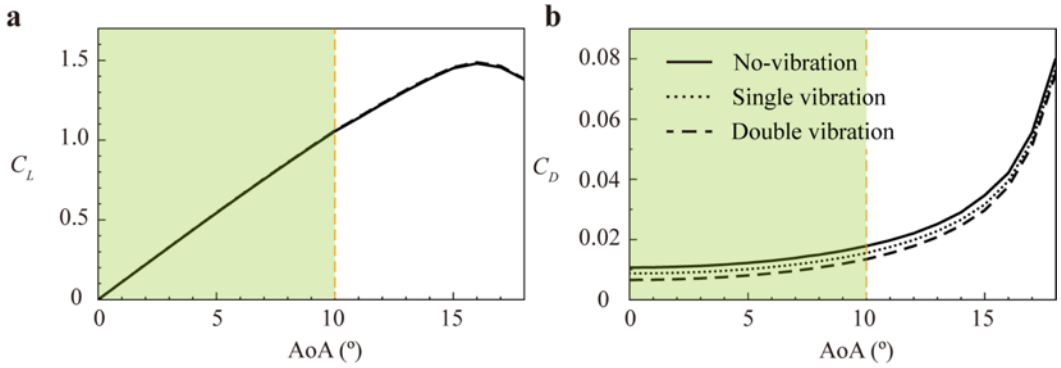

Figure 4-12 Variation of overall forces acting on the airfoil as a function of AoA

(a) Lift (C_L); (b) Total drag (C_D)

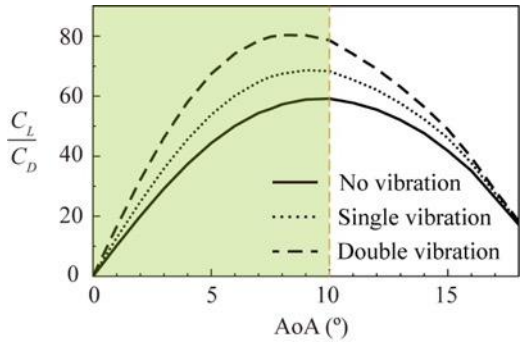

Figure 4-13 Variation of lift-to-drag ratio (C_L/C_D) as a function of AoA

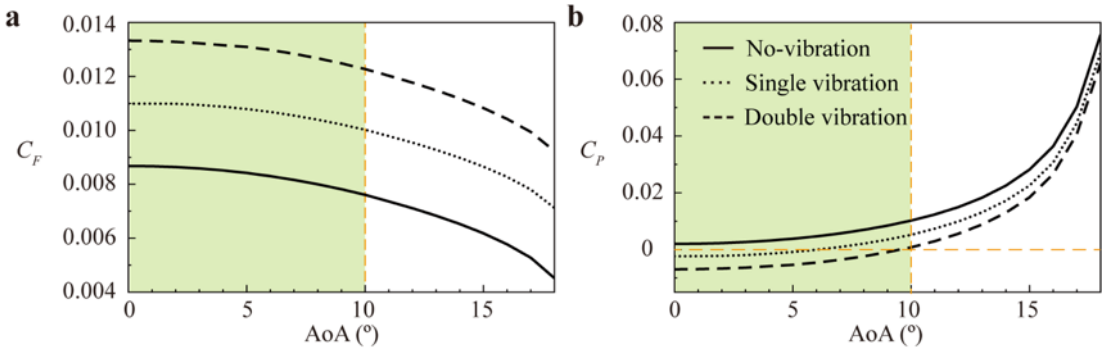

Figure 4-14 Variation of pressure and friction elements in total drag as a function of AoA

(a) Friction drag (C_F); (b) Pressure drag (C_P)

Figure 4-14 displays the variation of pressure and friction elements in total drag with respect to the AoA. Friction drag keeps decreasing when AoA increases, and from figure 4-14(a), it can be observed that the friction force curves for the three cases of no-, single and double vibration are nearly parallel. This indicates that the variation pattern of friction force with AoA has no dependence on wall oscillation. But the addition of wall DTLMUW will induce a high-speed downstream flow in near-wall region, leading to an increase in friction resistance. And the influence of increasing friction will be superimposed with the expansion of the vibration area. Different from the friction, the relationship between pressure and AoA shown in figure 4-14(b) exhibits the same monotonically increasing characteristic as depicted in figure 4-12(b) since pressure plays a dominate role in total drag. When the AoA is small, less than 6 degree for single vibration and 10 degree for double vibration, negative pressure drag appears, enabling the achievement of excellent pressure resistance reduction within a small AoA range. As the AoA increases, the differences resulting from changes in

the vibration area gradually diminish and the forces tend to converge toward the case without surface oscillation. And it is precisely due to the presence of this convergence that the drag reduction effect caused by wall oscillation gradually decreases as the AoA increases. As shown in figure 4-15 and 4-16, the large force and lift-to-drag ratio change occurs when the AoA is small. We can obtain about 18% drag reduction for single vibration and 38% for double vibration when AoA is 0º, but when the AoA reaches 15º, the drag reduction effect is almost halved. The variation rate of lift is negligible compared to drag, typically ranging from 0 to 1 percent. Thus, a significant improvement in time-averaged lift-to-drag ratios (C_L/C_D) can be observed, beyond 60% enhancement under double vibration when AoA=0º. Simultaneously, the drag reduction advantage caused by increasing the vibrating area on the airfoil surface also gradually diminishes with the increasing AoA. Here, it is worth noting that dolphins typically maintain small AoA during their cruising, coinciding with the small AoA range where the drag reduction effect induced by dynamic LMUW motion is more pronounced. This may provide some support for the idea that the dynamic skin boundary driven by DTLMUW of dolphins contributes to their low-drag characteristics.

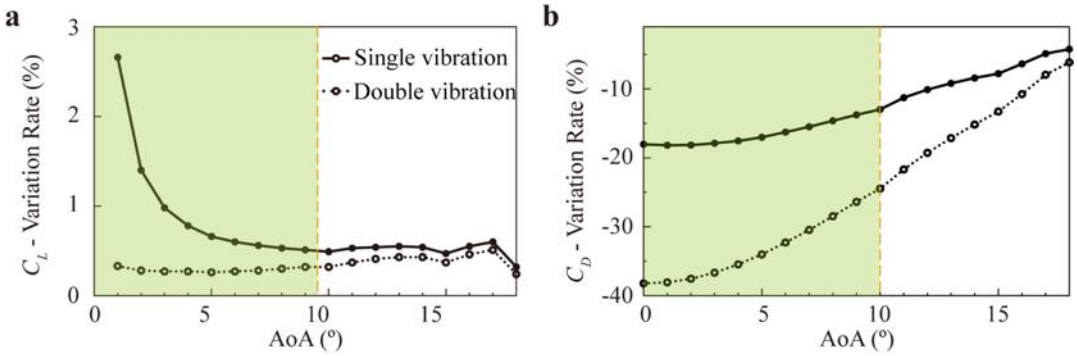

Figure 4-15 Variation rate versus AoAs

(a) Lift (C_L); (b) Total drag (C_D)

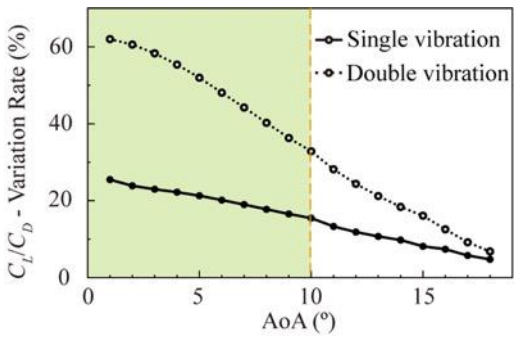

Figure 4-16 Variation rate of lift-to-drag ratio (C_L/C_D) as a function of AoA

4.5 EFFECT OF LOCATION ON AIRFOIL PERFORMANCE

4.5.1 Single vibration region

In the absence of wall oscillation, the force distribution varies with the location on the airfoil surface influenced by the streamlined shape. When we add the vibration region on the airfoil surface, the position where the wall DTLMUW motion occurs will also have an impact on its drag reduction effect. To explore this impact, we firstly take $0.1L_c$ as a motion unit and set the single vibration on the upper and lower surface when AoA is 0º. The vibration region moves from the side of leading edge (LE) to the tailing edge (TE). And the variation of drag with different vibration region positions can be found in figure 4-17. The addition of wall DTLMUW motion can reduce the total drag no matter where the oscillation occurs, but the drag reduction effect is highly dependent on the motion locations. As shown in figure 4-17(a), the total drag increases first and then decreases as the vibration region moves towards the tail of foil. There exists a special position, the maximum thickness of the foil, where the

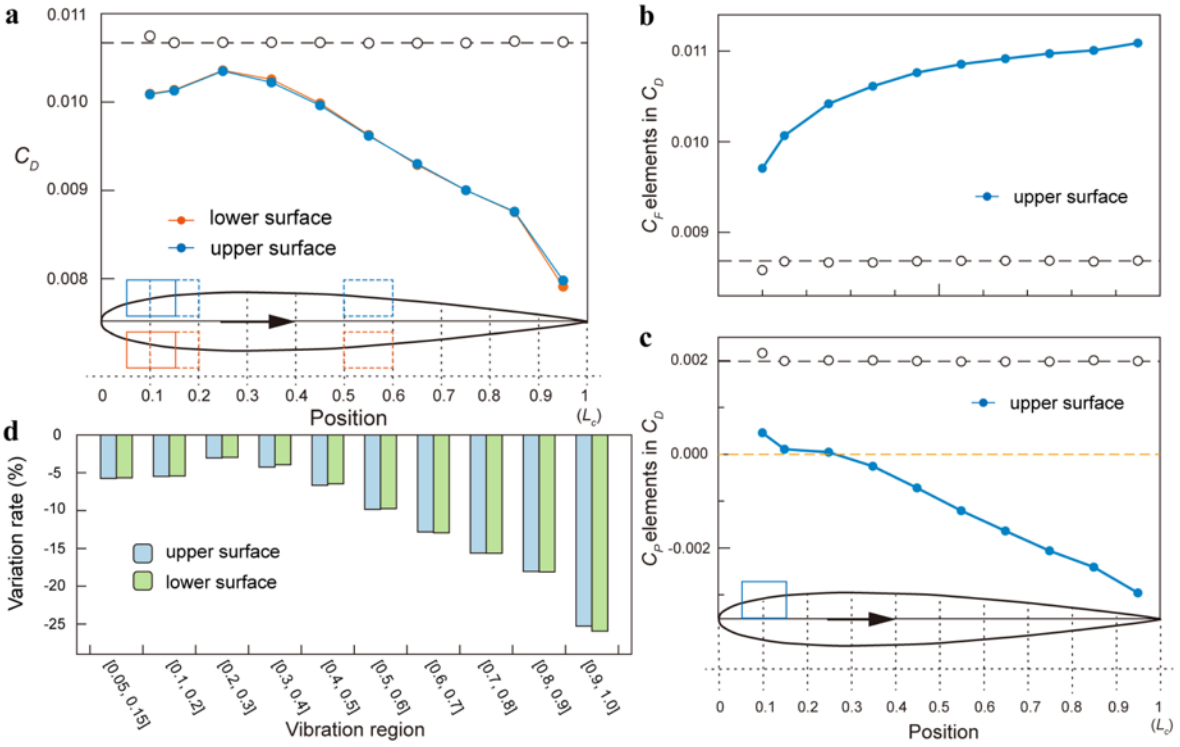

Figure 4-17 Drag force corresponding to different locations when AoA=0º

(a) Total drag; (b) Friction elements in total drag; (c) Pressure elements in total drag; (d) Variation rate of total drag after adding DTLMUW

corresponding drag is maximum in all the oscillation cases, consequently resulting in the minimum drag reduction effect. The less resistance can be obtained when the vibration region is farther away from this position, resulting in remarkable drag reduction rate on both surface beyond 25% at the position of [0.9L_c, 1.0L_c].

Different from the total drag, both friction and pressure force in figure 4-17(b) exhibit a monotonic variation with the change in vibration position. Friction drag gradually increases as the vibration position moves backwards. As pointed out earlier, the wall DTLMUW motion will not affect the overall velocity distribution but exerts a significant influence on the near-wall flow within the vibration region. A high-speed downstream boundary flow will be induced by the high-speed wave propagation of DTLMUW, leading to a higher near-wall velocity gradient. This is only related with the form of wall motion and independent of the position. Here, we maintain the oscillation form on the airfoil surface as DTLMUW and assume that the near-wall velocity gradient caused by wall motion remains consistent at all positions. And thus, the smaller the original no-vibration local shear stress, the larger the increase of velocity gradient caused by placing the vibration region at that position, resulting in a greater friction resistance. According to the distribution of near-wall velocity and wall shear stress under the no-vibration condition in figure 4-18, we can find that the original local velocity gradient gradually decreases from the front to the tail of foil except the small range near the LE. Therefore, the friction under wall motion will gradually increase as the vibration region moves to the tail.

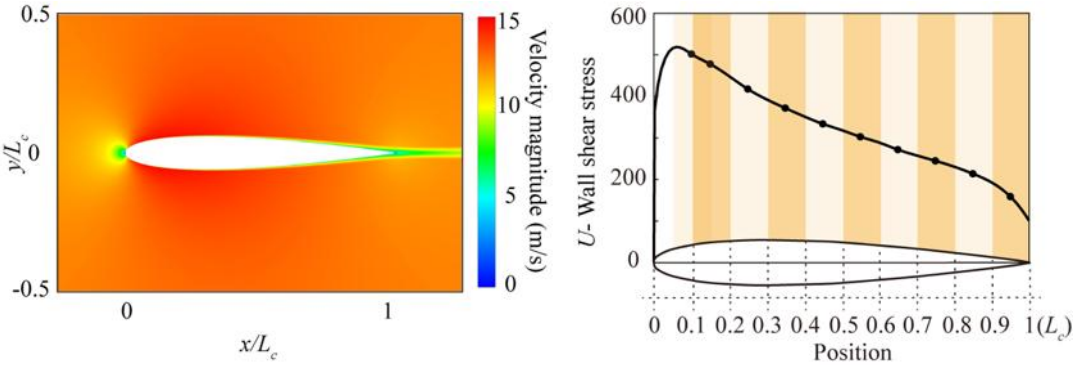

Figure 4-18 Wall shear stress on the upper surface under no-vibration condition

Contrary to the friction force, as depicted in figure 4-17(c), pressure drag keeps decreasing when the vibration region is shifted backward. Interestingly, the negative pressure

force appears when the wall motion is arranged behind the maximum thickness position. Figure 4-19 compares the pressure field distribution around the airfoil without and with DTLMUW motion in different positions shown by red frame in figure 4-19(a). When there is no vibration on airfoil surface, the pressure on the upper and lower surface is symmetric, with an obvious negative pressure region existing on the front half of the airfoil shown in figure 4-19(b). The addition of wall motion will break the symmetry and induce a periodic pressure fluctuation which is the alteration process of high and low pressure near the vibration region. The high pressure caused by the dynamic wall will bring a counteracting effect on the non-vibrating negative pressure region. When the wall vibration occurs in the range of original negative pressure region, for [$0.05L_c$, $0.15L_c$] and [$0.2L_c$, $0.3L_c$] in figure 4-19(c), the motion-induced high pressure can offset the original negative pressure on the upper surface completely. And as the vibration region gradually moves away from the front low-pressure area to the tail, although the high pressure brought by the dynamic wall gradually becomes stronger, its counteracting effect on the original negative pressure zone will be weakened but still present. The oscillation low pressure will strengthen the negative pressure effect on the upper surface. When the LMUW motion occurs in the rear half of the airfoil, the low pressure generated by wall motion will be connected to the original negative region. And thus, the area of negative pressure on the upper surface will increase, even cover the entire upper surface when the vibration region is [$0.9L_c$, $1.0L_c$]. The different pressure distributions result in the pressure resistance varying with vibration position. And the increase of the negative pressure area and enhancement of the motion-induced high pressure as the vibration region moves to the tail may both provide some contributions to the reduction of pressure drag.

We also notice here another specific unit position [$0.9L_c$, $1.0L_c$] which is directly connected to the tail end of foil. As shown in figure 4-19(c), when the vibration region is not directly contact with the TE, although wall motion causes a noticeable pressure variation on the upper surface, it does not affect the force distribution on the lower surface. This situation changes when the DTLMUW is arranged in this specific region. The results indicate that the pressure fluctuation range induced by wall vibration in the specific region is far beyond the vibration region itself, simultaneously exerting a significant impact on the pressure distribution on the lower surface. The original negative pressure region on both the upper

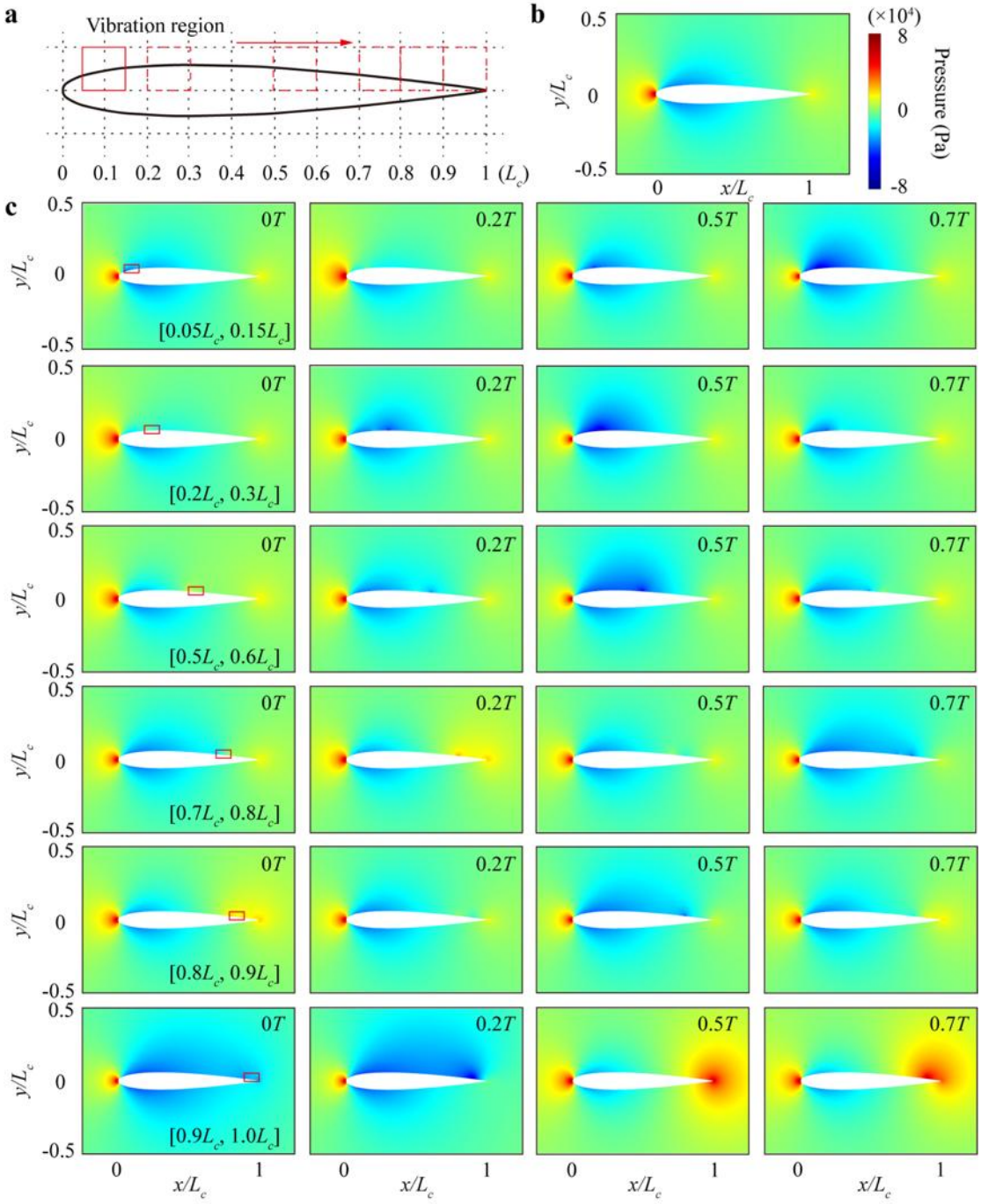

Figure 4-19 Pressure distribution corresponding to different location of DTLMUW when AoA=0º

(a) Vibration region; (b) No vibration; (c) Pressure distributions under different location conditions

and lower surface will be counteracted and expanded with the occurrence of high pressure and low pressure induced by wall vibration respectively. And the strength of pressure

fluctuation is also much greater than other cases. Thus, although arranging the DTLMUW motion in this region can achieve a great drag reduction, the special effects brought about by the direct connection between the vibration region and the airfoil tail cannot be ignored.

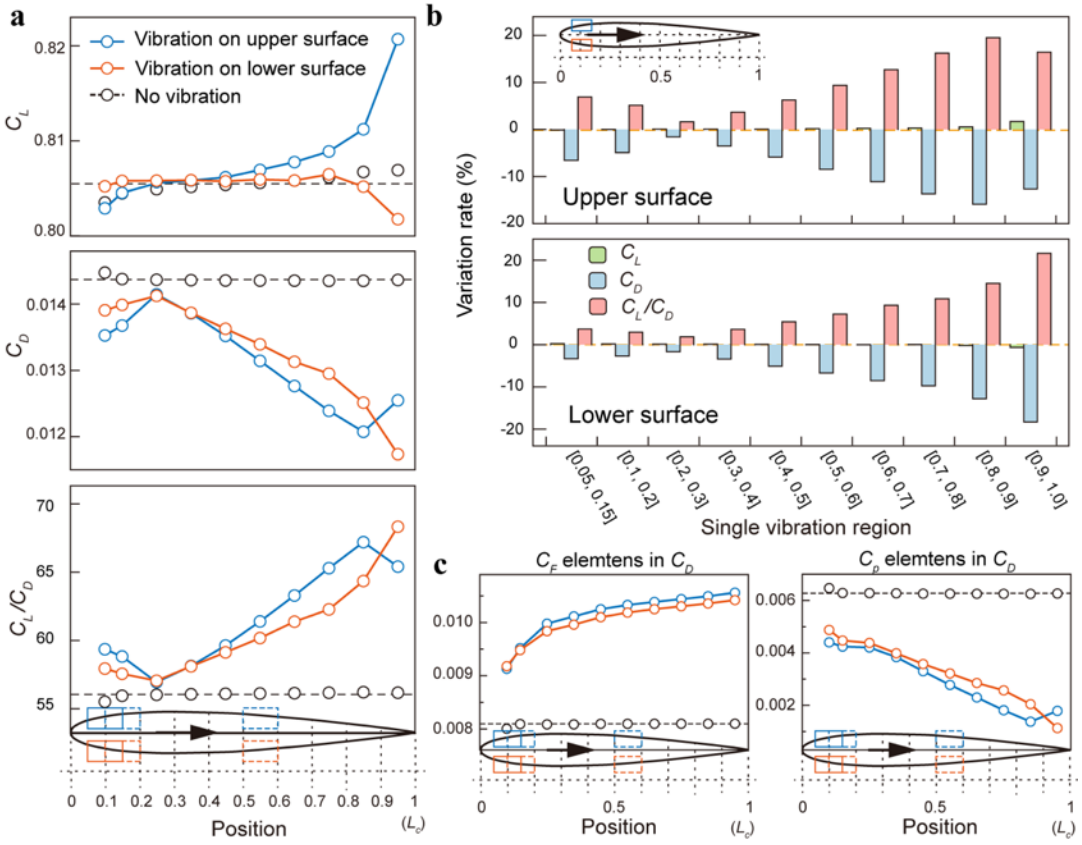

Figure 4-20 Drag forces corresponding to different locations when AoA=7.5º

(a) Lift (C_L), drag (C_D) and lift-to-drag ratio (C_L/C_D); (b) Variation rates against different locations; (c) Location-dependent friction-drag (C_F) and pressure-drag (C_P) elements in C_D

The flow over the upper and lower airfoil surfaces is symmetrical when AoA is 0º, leading to the DTLMUW-induced drag variations placed at the same locations on both surfaces remain largely consistent, as indicated in figure 4-17(d). However, as AoA increases, the flow distribution on the two surfaces gradually changes and no longer shows a symmetrical trend. The effect of this overall asymmetry in the flow field on vibration-induced drag is also investigated here. Figure 4-20 displays the distribution of DTLMUW-induced drag at different positions when AoA=7.5º. As shown in figure 4-20(a) and (b), the

time-averaged lift coefficients (C_L) remain robust to the localization of the vibration unit, exhibiting only slight variations from the LE to TE. In contrast, the total drag coefficients (C_D) display a pronounced dependency on the localization of the vibration unit, with the maximum reduction observed at the TE and the minimum reduction at near the position of maximum thickness, consistent with the regularity when AoA=0º. This results in a noticeable localization dependency in the lift-to-drag ratio (C_L/C_D). Additionally, due to the asymmetry of flow, placing the vibration unit on the upper surface proved to be more effective than on the lower surface, except at [$0.9L_c$, $1.0L_c$] at the TE, where flow separation occurs and significantly impacts the pressure-based drag but has minimal effect on the friction-based drag [figure 4-20(c)]. The drag reduction effect will be greatly reduced when DTLMUW is arranged in the region of flow separation. Consequently, the time-averaged lift-to-drag ratio (C_L/C_D) is most improved when the single vibration unit was localized at [$0.8L_c$, $0.9L_c$] on the upper surface and at [$0.9L_c$, $1.0L_c$] on the lower surface, resulting in remarkable improvements of 19.54% and 21.63%, respectively.

4.5.2 Multiple vibration regions

On the actual surface of dolphin skin, Shoemaker and Ridgway [99] discovered the presence of shadow, regular cutaneous ridges over much of their bodies, indicating that the actual dynamic skin oscillation region of dolphin may also be larger than the motion unit we defined here. Thus, we try to arrange multiple motion units, which may be discontinuous or continuous, on the airfoil surface to explore the influence of large wall motion area on the drag reduction. In this section, the AoA condition is kept equal to 0º or 7.5º and the wall motion modes on each vibration unit are maintained as DTLMUW, with the wall equation consistent with equation (4-1). As illustrated in the following four tables, all combinations of the vibration units demonstrate a synergistic effect in reducing drag, with the greatest reduction observed when all the vibration units are closed to the TE, while maintaining lift (when AoA=7.5º) with a maximum variation in C_L of less than +1.71%. This results in a substantial improvement in the lift-to-drag ratio (C_L/C_D) shown in table 4-6.

Table 4-3 Total drag (C_D) under various vibration combinations when AoA=0º

Vibration regions (L_c)			C_D No-vibration	Variation Rate	C_D Vibration	Variation Rate
-			(0.0106710)	-	-	-
Single vibration (upper surface)		[0.2, 0.3]	0.0106759	(0.05%)	0.01035019	-3.05%
		[0.5, 0.6]	0.0106672	(-0.04%)	0.00965210	-9.52%
		[0.6, 0.7]	0.0106673	(-0.04%)	0.00928038	-13.00%
		[0.7, 0.8]	0.0106692	(-0.02%)	0.00891243	-16.47%
		[0.8, 0.9]	0.0106881	(0.16%)	0.00875953	-18.04%
		[0.9, 1.0]	0.0106797	(0.08%)	0.00797993	-25.28%
Single vibration (lower surface)		[0.8, 0.9]	0.0106881	(0.16%)	0.00875364	-18.10%
Multiple vibration regions	Discontinuous (upper and lower surface)	[0.8, 0.9]	0.0106881	(0.16%)	0.00660195	-38.23%
	Discontinuous (upper surface)	[0.2, 0.3] & [0.8, 0.9]	0.0106730	(0.02%)	0.00815812	-23.56%
		[0.2, 0.3] & [0.5, 0.6] & [0.8, 0.9]	0.0106762	(0.05%)	0.00703159	-34.14%
	Continuous (upper surface)	[0.7, 0.9]	0.0106761	(0.05%)	0.00673418	-36.92%
		[0.6, 0.9]	0.0106786	(0.07%)	0.00534213	-49.97%
	Specific region (upper surface)	[0.2, 0.3] & [0.9, 1.0]	0.0106803	(0.09%)	0.00761933	-28.66%
		[0.7, 1.0]	0.0106880	(0.16%)	0.00406313	-61.98%

Table 4-4 Lift coefficients (C_L) under various vibration combinations at AoA=7.5º

Vibration regions (L_c)			C_L No-vibration	Variation Rate	C_L Vibration	Variation Rate
-			(0.80549831)	-	-	-
Single vibration (upper surface)		[0.2, 0.3]	0.80492088	(-0.07%)	0.80554409	0.08%
		[0.7, 0.8]	0.80617670	(0.08%)	0.80888824	0.33%
		[0.8, 0.9]	0.80672744	(0.16%)	0.81122260	0.56%
		[0.9, 1.0]	0.80692139	(0.18%)	0.82069304	1.71%
Single vibration (lower surface)		[0.8, 0.9]	0.80672744	(0.16%)	0.80518518	-0.19%
Multiple vibration regions	Discontinuous (upper and lower surface)	[0.8, 0.9]	0.80672744	(0.16%)	0.80922064	0.31%
	Discontinuous (upper surface)	[0.2, 0.3] & [0.8, 0.9]	0.80551020	(0.00%)	0.81000469	0.56%
	Continuous (upper surface)	[0.7, 0.9]	0.80747430	(0.25%)	0.81430776	0.85%
	Specific region (upper surface)	[0.2, 0.3] & [0.9, 1.0]	0.80558530	(0.01%)	0.81939876	1.71%

Table 4-5 Drag coefficients (C_D) under various vibration combinations at AoA=7.5º

Vibration regions (L_c)			C_D No-vibration	Variation Rate	C_D Vibration	Variation Rate
-			(0.01437138)	-	-	-
Single vibration (upper surface)		[0.2, 0.3]	0.01436747	(-0.03%)	0.01414588	-1.54%
		[0.7, 0.8]	0.01435155	(-0.14%)	0.01238919	-13.67%
		[0.8, 0.9]	0.01435134	(-0.14%)	0.01207265	-15.88%
		[0.9, 1.0]	0.01436447	(-0.05%)	0.01254823	-12.64%
Single vibration (lower surface)		[0.8, 0.9]	0.01435134	(-0.14%)	0.01251250	-12.81%
Multiple vibration regions	Discontinuous (upper and lower surface)	[0.8, 0.9]	0.01435134	(-0.14%)	0.01003367	-30.09%
	Discontinuous (upper surface)	[0.2, 0.3] & [0.8, 0.9]	0.01442660	(0.38%)	0.01167772	-19.05%
	Continuous (upper surface)	[0.7, 0.9]	0.01435536	(-0.11%)	0.00970850	-32.37%
	Specific region (upper surface)	[0.2, 0.3] & [0.9, 1.0]	0.01444607	(0.52%)	0.01217145	-15.75%

Table 4-6 Lift-to-drag ratio (C_L/C_D) under various vibration combinations at AoA=7.5º

Vibration regions (L_c)			C_L/C_D No-vibration	Variation Rate	C_L/C_D Vibration	Variation Rate
-			(56.0488)	-	-	-
Single vibration (upper surface)		[0.2, 0.3]	56.0238	(-0.04%)	56.9455	1.65%
		[0.7, 0.8]	56.1735	(0.22%)	65.2899	16.23%
		[0.8, 0.9]	56.2127	(0.29%)	67.1951	19.54%
		[0.9, 1.0]	56.1748	(0.22%)	65.4031	16.43%
Single vibration (lower surface)		[0.8, 0.9]	56.2127	(0.29%)	64.3505	14.48%
Multiple vibration regions	Discontinuous (upper and lower surface)	[0.8, 0.9]	56.2170	(0.29%)	80.6505	43.47%
	Discontinuous (upper surface)	[0.2, 0.3] & [0.8, 0.9]	55.8351	(-0.38%)	69.3632	24.23%
	Continuous (upper surface)	[0.7, 0.9]	56.2490	(0.36%)	83.8758	49.12%
	Specific region (upper surface)	[0.2, 0.3] & [0.9, 1.0]	55.7650	(-0.52%)	67.3214	20.72%

4.5.2.1 Discontinuous combinations of vibration unit

We firstly consider a discontinuous scenario, where the motion units are simultaneously placed on both upper and lower surfaces of the foil, with the location of the wall vibration at the two surfaces both chosen to be [$0.8L_c$, $0.9L_c$]. Figure 4-21(a) displays the pressure

distribution in one period when the wall oscillation only occurs on the upper and lower surface respectively. Due to the symmetry in the flow on the two surfaces of airfoil under the condition of AoA=0º, the pressure variations corresponding the two single cases are nearly identical except for the phase difference. The difference in phase does not affect the overall time-averaged drag on the airfoil. Thus, the drag reduction effect is almost the same when wall oscillation occurs at the same position on either the upper or lower surface, as shown in table 4-3. When vibration unit is simultaneously arranged on both surfaces, the pressure changes induced by wall motion on the two surfaces will not mutually affect each other. And the overall flow field shown in figure 4-21(b) exhibits a simple combination effect of the two single cases. This linear superposition features can also be reflected on the force distribution. Here, we firstly define a reference force, given by:

$$F_{ref} = \sum_{i=1}^{n} F_{m_i} - (n-1)F_{nm}\,, \qquad (4-7)$$

which denotes the sum of forces in the single cases (F_{m_i}), subtracted by the force under the condition of no wall motion (F_{nm}) to eliminate the force repetition caused by the superposition of multiple vibration cases, and n represents the number of oscillation units. As shown in figure 4-22, the actual force distribution for the multi-unit case is nearly consistent with the reference force. The linear superposition property causes the lift fluctuations acting on the airfoil become more pronounced. But as mentioned in section 4.3, the lift force exhibits a symmetrical distribution about the no-vibration case (here is 0 when AoA=0º), and thus the overall periodic-averaged lift will not be obviously affected by dynamic boundary despite the increasing wall motion area. Contrary to the lift, the total drag will be reduced, moreover, the offsetting effect caused by the phase difference under the two single cases in linear superposition process also contributes to a reduction in total force fluctuations. We only consider the situation where wall motion is the same for all vibration units here. However, based on this linear superposition property, the different combination effects can be achieved by modulating the wall motion forms and phases within different vibration units, which allows for a more extensive research in drag reduction design, aiming at achieving various objectives such as reducing drag and minimizing force fluctuations. The pressure drag dominates the total drag and thus have the similar regularity as the total drag. But the friction, which is only related with the wall motion area and form, always increase

after increasing the vibrating area. When AoA is 7.5º, the situation is similar to the case of AoA=0º. The distribution of pressure filed or forces acting on the airfoil both satisfy the linear superposition features, as shown in figure 4-23.

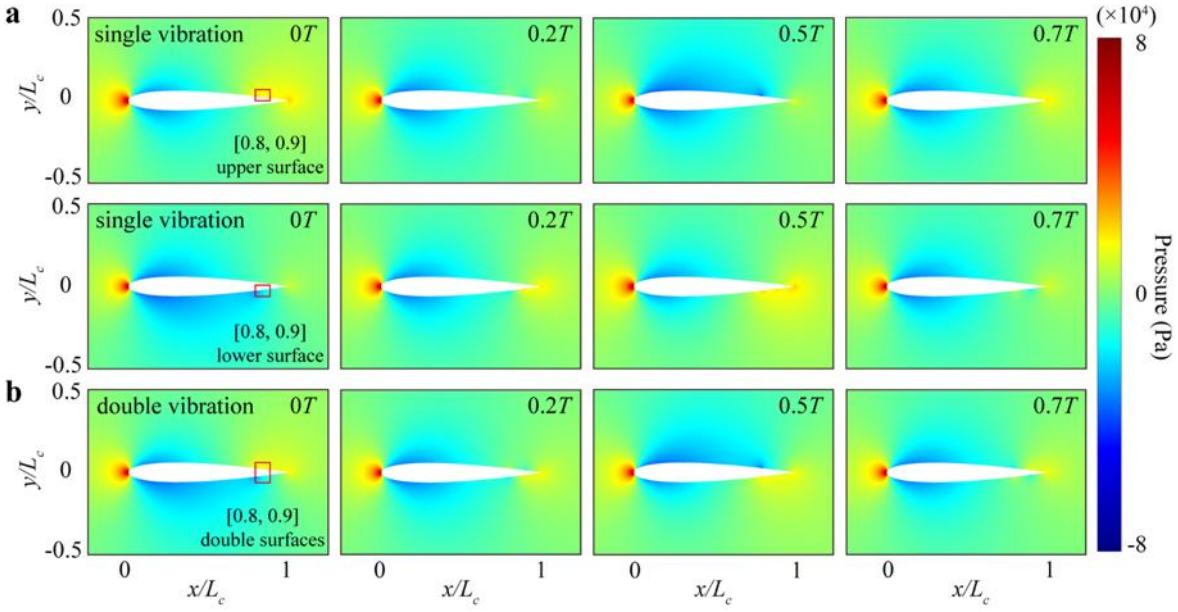

Figure 4-21 Pressure distribution under double vibration when AoA=0º

(a) Single vibration; (b) Double vibration

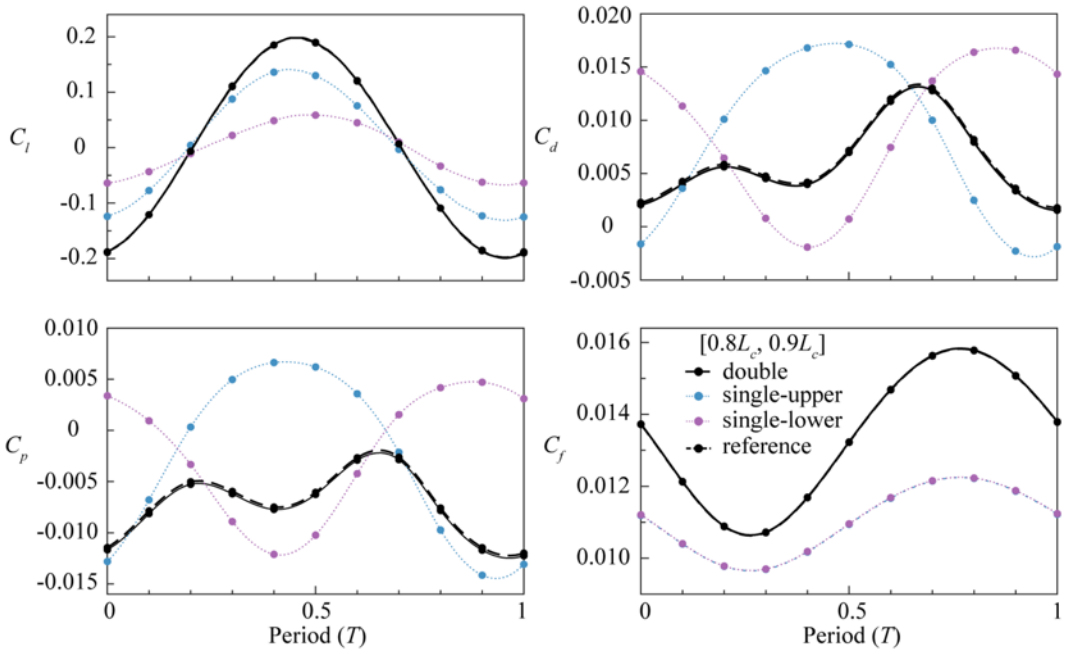

Figure 4-22 Time-varying force distributions under double vibration when AoA=0º

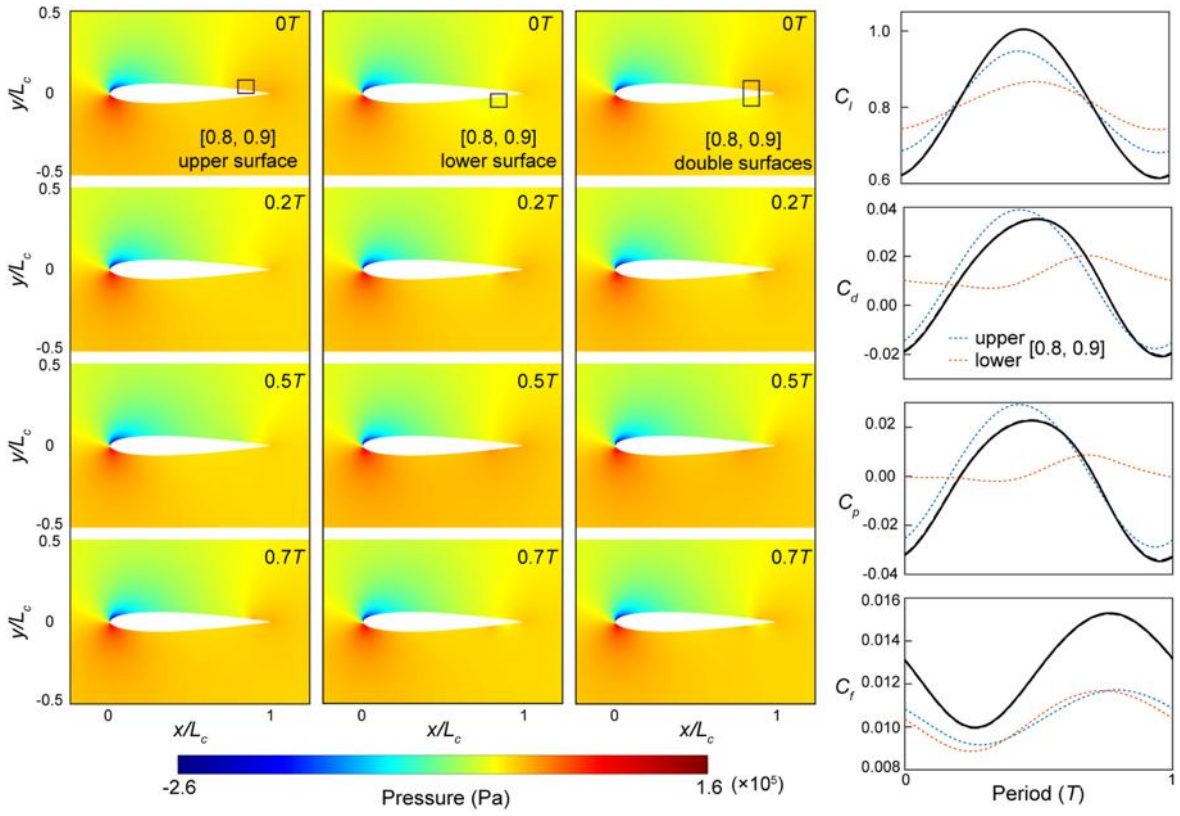

Figure 4-23 Double vibration when AoA=7.5º

The second case we considered is to arrange both two motion units on the same surface, the upper surface of airfoil here. The vibration regions are chosen as [0.2L_c, 0.3L_c] and [0.8L_c, 0.9L_c]. Consistent with the first scenario, the total drag after combing two motion units on the same surface can also be significantly decreases (table 4-3). And the pressure distribution in figure 4-24(a) and figure 4-25 can also be viewed as the simple linear combination of the two single cases (see figure 4-19 for AoA=0º) for both conditions of AoA=0º and 7.5º. But there exists a slight difference that the pressure variation caused by wall motion will interact with each other when the vibration unit are placed on the same surface, especially obvious when AoA=0º. When AoA=0º, the oscillation-induced low pressure can obviously expand and strengthen the negative pressure region on the upper surface, and thus induce a larger lift fluctuation shown in figure 4-26. Although multi-unit wall oscillation on the same surface slightly affects the pressure distribution, the linear superposition feature of force is still maintained. As analyzed before, the pressure and total drag can be reduced, with a weakening

of the force fluctuations in a period due to the combination of vibration units, but the friction drag increases (figure 4-26).

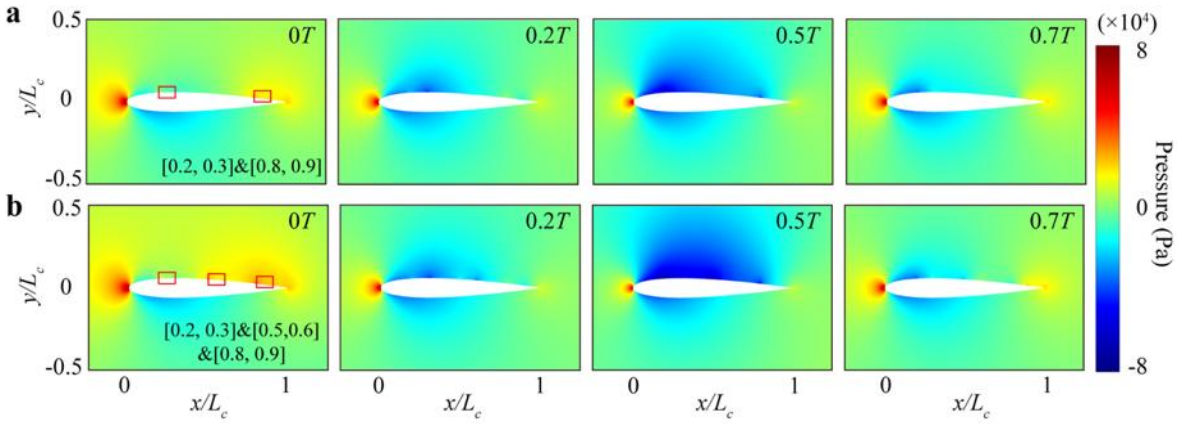

Figure 4-24 Pressure under discontinuous arrangement on the upper surface when AoA=0º

(a) Vibration regions: [0.2L_c, 0.3L_c] & [0.8L_c, 0.9L_c]; (b) [0.2L_c, 0.3L_c] & [0.5L_c, 0.6L_c] & [0.8L_c, 0.9L_c]

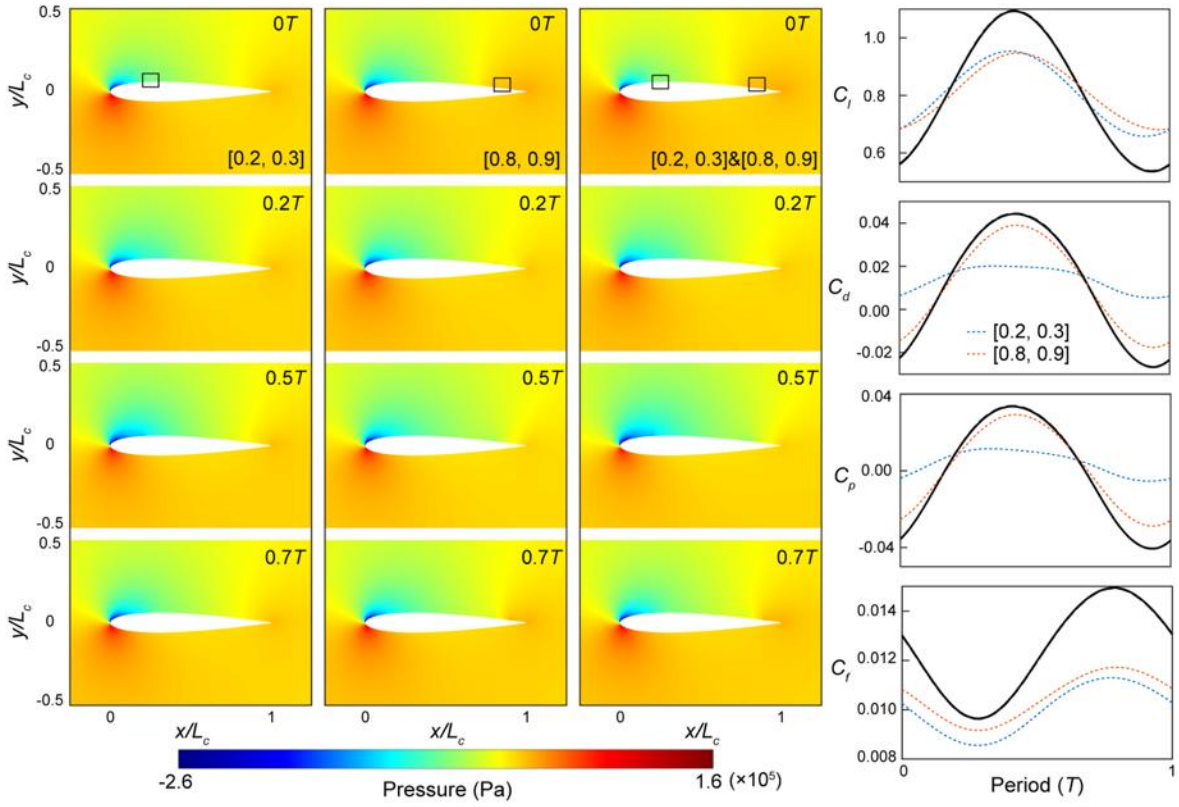

Figure 4-25 Discontinuous arrangement on the upper surface when AoA=7.5º

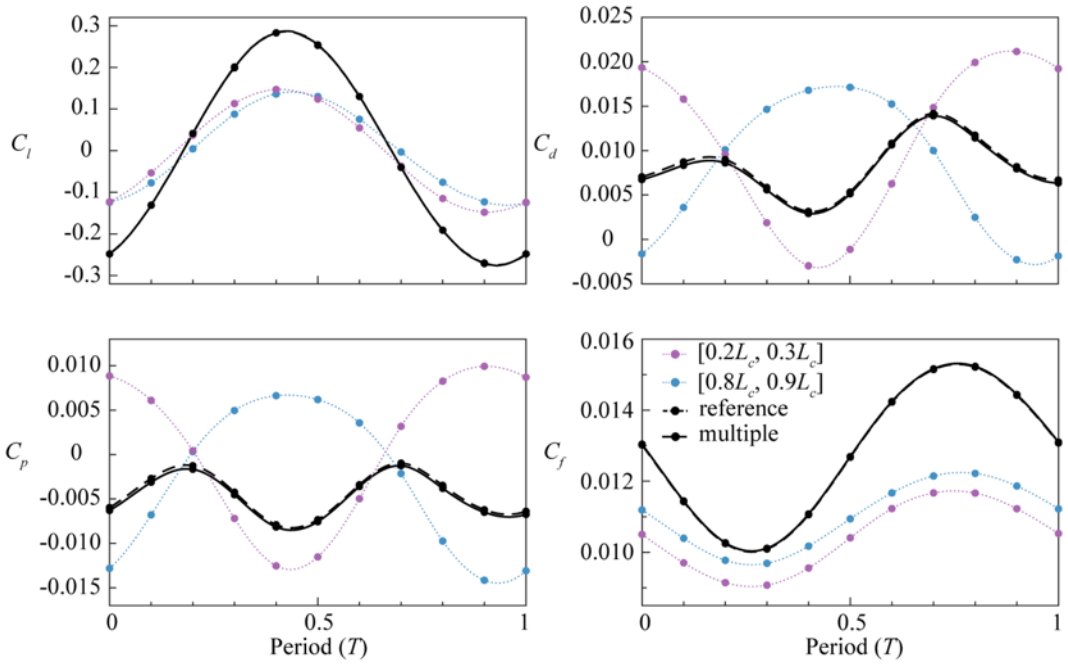

Figure 4-26 Time-varying forces under discontinuous two vibration units on the upper surface when AoA=0º

We also continue to add the vibration region [0.5L_c, 0.6L_c] on the upper surface when AoA=0º. As the increase of the vibration region, the total drag is further reduced (table 4-3). And the interaction between motion units becomes stronger than the combination of two units. We can find from figure 4-24(b) that the high- and low- pressure induced by wall motion are both greatly enhanced. According to the pressure field in figure 4-24(b) and force distribution in figure 4-27, it can still be satisfied that the characteristic of multiple discontinuous vibration regions can be regarded as a linear superposition of the single cases, but the enhancement of pressure fluctuation due to the addition of more motion units cannot be ignored which can be directly reflected on the force distribution. The discontinuous arrangement of multiple vibration regions under the same motion state increases lift fluctuations within the cycle but particularly suppresses the pressure drag fluctuations. However, the periodic fluctuating state of these forces will not affect the overall effectiveness of this arrangement on the time-averaged force acting on the airfoil, maintaining a reduction in total drag while having no impact on lift. Considering that the phase difference of force distribution between different vibration units will have a great impact on the multi-unit

combined force in the linear superposition process, it can be achieved to manipulate the force fluctuations by adjusting the motion phases within different vibration units, in order to achieve a reduction in overall resistance while minimizing force fluctuations, thereby obtaining a better performance optimization design.

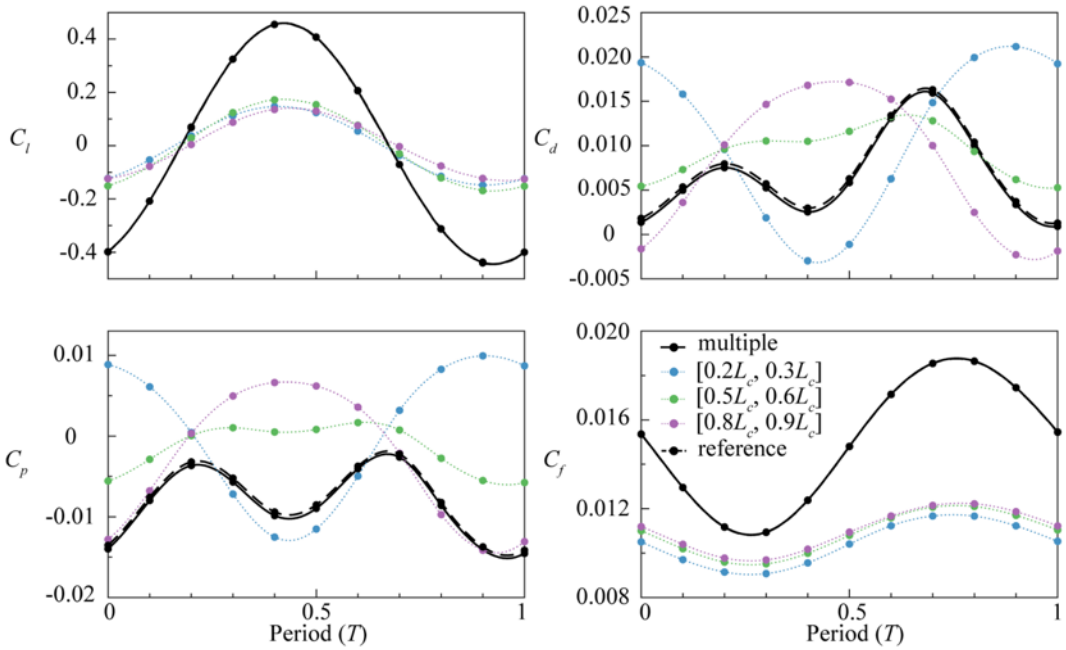

Figure 4-27 Time-varying forces under discontinuous three vibration units on the upper surface when AoA=0º

4.5.2.2 Continuous combinations of vibration unit

The situation of the continuous arrangement of wall motion units is also considered here. We firstly set the vibration region as [0.7L_c, 0.9L_c] on the upper surface of airfoil under both two AoA conditions (0º and 7.5º). According to tables 4-3 and 4-5, whether the motion units are arranged continuously or discontinuously, the total drag will be obviously reduced after extending the vibration area. But there are significant differences in the flow field and force distribution corresponding to the continuous and discontinuous cases. As shown in figures 4-28(a) and 4-29, the continuous vibration region [0.7L_c, 0.9L_c] can be viewed as a larger motion unit, thereby inducing a stronger motion-induced high and low pressure, forming a pressure distribution completely unrelated to the original single unit. Thus, the linear superposition characteristic observed in discontinuous cases, especially concerning lift, total drag and pressure drag, is no longer satisfied here. It can also be observed from

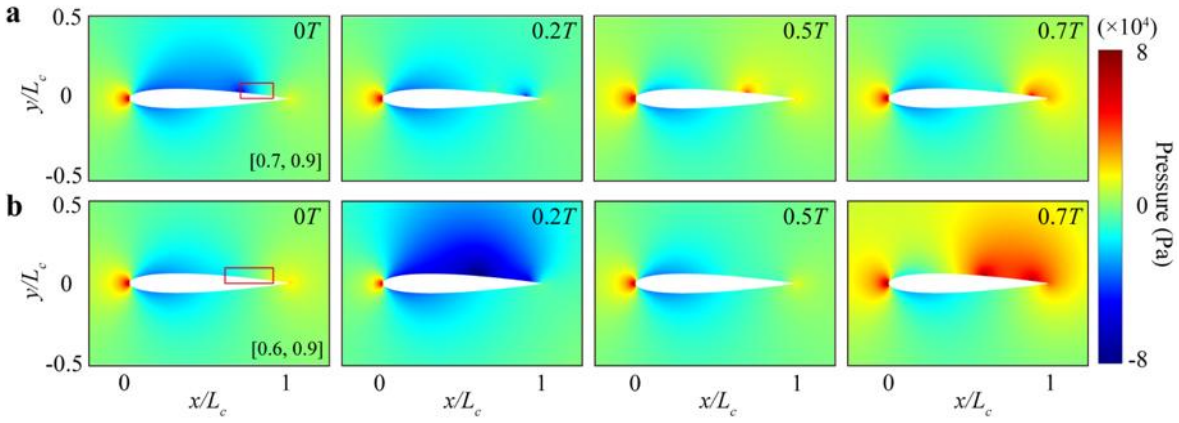

Figure 4-28 Pressure under continuous arrangement on the upper surface when AoA=0º

(a) Vibration regions: [0.7L_c, 0.9L_c]; (b) Vibration regions: [0.6L_c, 0.9L_c]

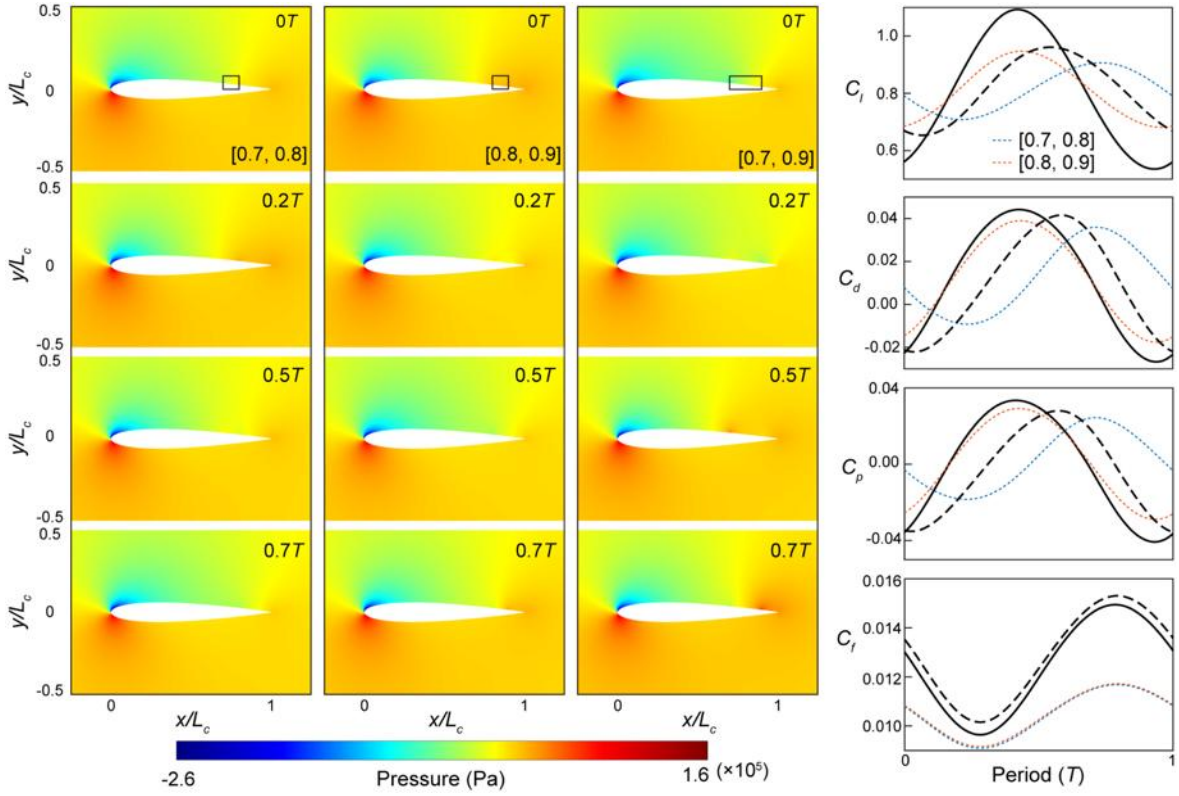

Figure 4-29 Continuous arrangement on the upper surface when AoA=7.5º

figures 4-29 and 4-30 that the actual lift and drag on the airfoil differ in magnitude, fluctuation and phase compared to the calculated reference forces. Moreover, when AoA=0º, we notice that the arrangement of two continuous units results in a better drag reduction

effect with lift and drag (pressure and total drag) fluctuations smaller than the reference forces. The friction resistance component due to its dependence only on the form and area of wall motion, can still be considered as an approximate summation of the single units. Therefore, when designing the arrangement of two single units in the small AoA condition of 0º, the reduction in force fluctuation due to the continuous placement is an advantage worth considering. But as the vibrating area increases to three original single units when AoA=0º, the pressure distribution induced by the larger motion unit displays a noticeable variation. Comparing the flow field in figure 4-28(a) and (b), the high and low pressure induced by the wall motion in a large region [0.6L_c, 0.9L_c] are strongly strengthen than the two-continuous cases [0.7L_c, 0.9L_c], which will result in a larger fluctuation in force. Nevertheless, a less drag and better drag reduction effect can also be induced due to a larger oscillating area (tables 4-3 and 4-5), which is consistent with the discontinuous cases.

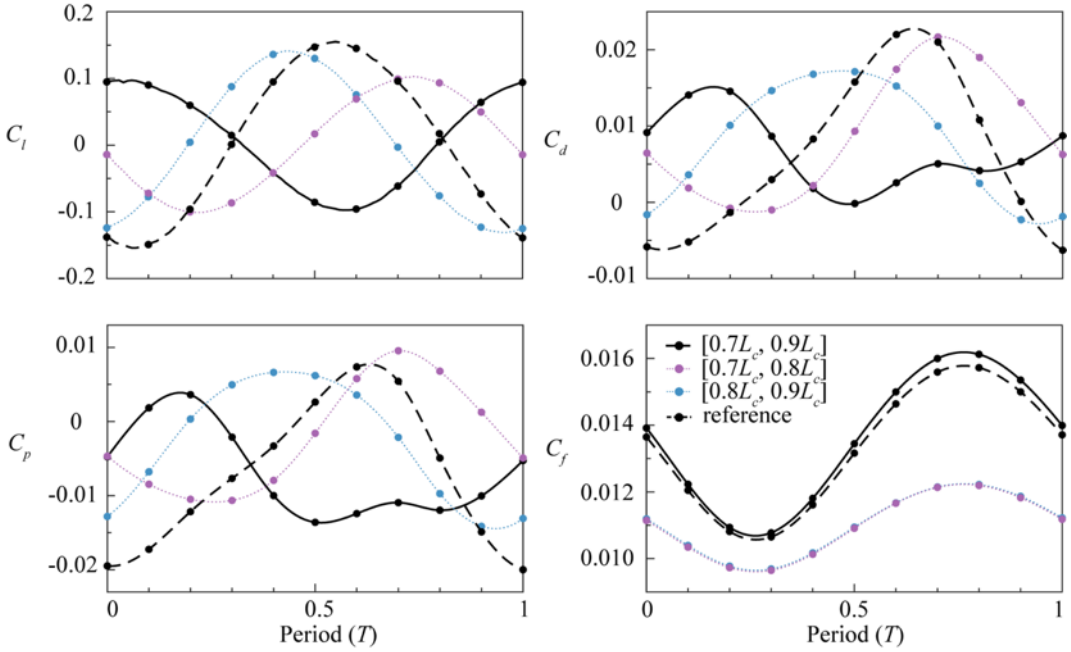

Figure 4-30 Time-varying forces under continuous two vibration units on upper surface when AoA=0º

4.5.2.3 Multiple combinations including the special region at TE

A specific motion unit [0.9L_c, 1.0L_c] directly connected to the TE of the airfoil has been mentioned in section 4.4. When the wall DTLMUW motion occurs in this region when AoA=0º, the pressure variations in a period are dramatic compared to other positions. But it is interesting to notice that the strong pressure fluctuations are suppressed when the wall

oscillation occurs simultaneously in the specific region and other regions. Figure 4-31(a) displays the pressure field when the wall motions units are discontinuously arranged at [0.2L_c, 0.3L_c] and [0.9L_c, 1.0L_c]. The pressure variations near the tail end are significantly weaker than the single cases [0.9L_c, 1.0L_c] in figure 4-19. And thus, although the motion units are discontinuous, the linear superposition principle of lift, pressure and total drag shown in figure 4-32 is not satisfied due to the suppression effect. And the actual force fluctuations acting on the airfoil are also obviously smaller than the reference forces. But the friction resistance, which is only related with the wall vibration form and area, always keep the superposition regularity and independent to the vibration position arrangement.

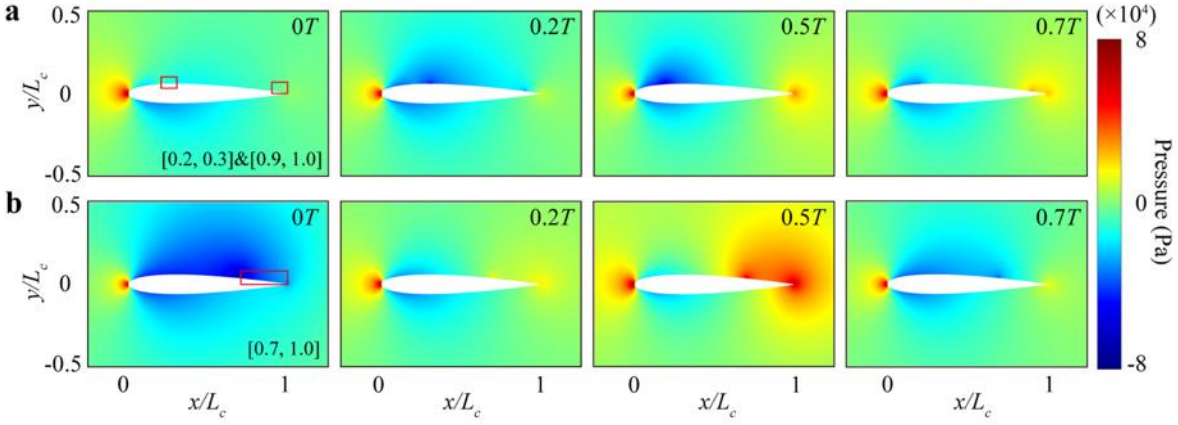

Figure 4-31 Pressure distributions under the arrangement including special region at TE when AoA=0º

(a) Vibration regions: [0.2L_c, 0.3L_c] & [0.9L_c, 1.0L_c]; (b) Vibration regions: [0.7L_c, 1.0L_c]

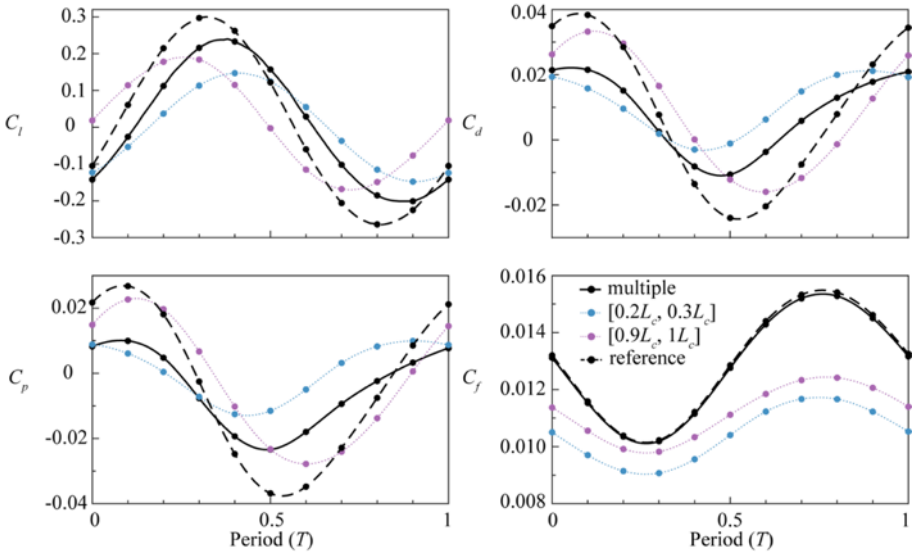

Figure 4-32 Time-varying forces under the arrangement including special region at TE when AoA=0º

The suppression effect can also be found in the continuous situation. From figure 4-28(b), we learn that the three-unit continuous motion arrangement induces a very intense pressure variation near the oscillating region, leading to a significant lift fluctuation. Figure 4-33(a) and (b) represent the lift distribution on the airfoil when the vibration region is [0.1L_c, 0.4L_c] and [0.6L_c, 0.9L_c], respectively, where the fluctuations far exceed the single cases and the reference values. However, when the large continuous motion region is positioned at the airfoil trailing edge, we observe that the intensity of pressure variations of [0.7L_c, 1.0L_c] in figure 4-31(b) are slightly weaker than the case of [0.6L_c, 0.9L_c] in figure 4-28(b). And the peak value of lift under the condition of [0.7L_c, 1.0L_c] shown in figure 4-33(c) are not much different from the reference value. Despite variations in pressure distribution with different vibration regions design, the periodic force fluctuations do not significantly affect the time-averaged force acting on the airfoil. Therefore, when extending the motion area, the achieved drag reduction effect will continue to increase based on the arrangement of the vibration positions (table 4-3). This also suggests that for the specific region, although the isolated placement of vibration in this region leads to an obvious pressure fluctuation, this disadvantage will be eliminated when the vibration is arranged in multiple or larger regions. As a result, the drag reduction effect is increased while reducing force fluctuations within the cycle, which shows a great advantage in improving the airfoil performance when do some optimization designs.

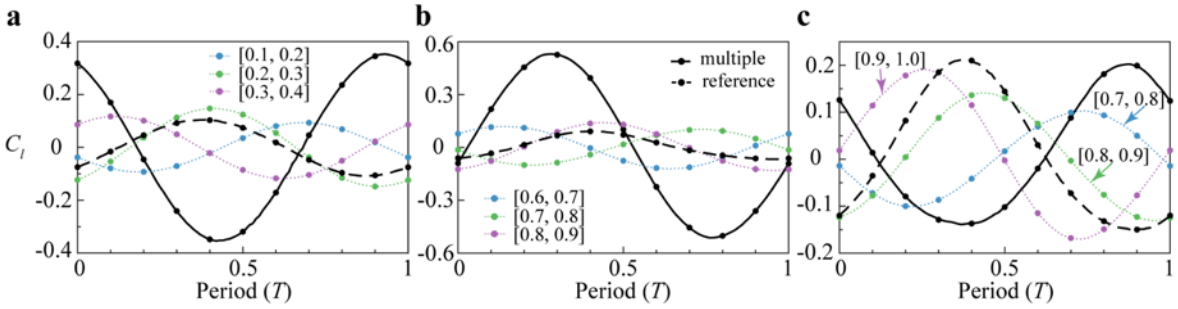

Figure 4-33 The suppression effect of lift fluctuation induced by the special region at TE when AoA=0º

When AoA=7.5º, the placement of vibrations at the TE of airfoil [0.9L_c, 1.0L_c] does not results in significant and intense pressure fluctuations as it does under the condition of AoA=0º, as depicted in figure 4-34. Therefore, the suppression effect brought about by the

multi-region arrangement at the specific positions under AoA=0º naturally does not exist. However, it is important to note that flow separation occurs at the TE on the upper surface of airfoil when the angle of attack is 7.5º. The presence of flow separation will also break the law of linear superposition when the motion units are arranged discontinuously, as shown in figure 4-34. But we mentioned above that placing the vibration unit in the region of flow separation is not a good choice because the drag reduction effect will be reduced. Thus, although the region near the TE without flow separation can induce a great drag reduction effect, more attention needs to be focused on the specific flow characteristics corresponding to this special tail region.

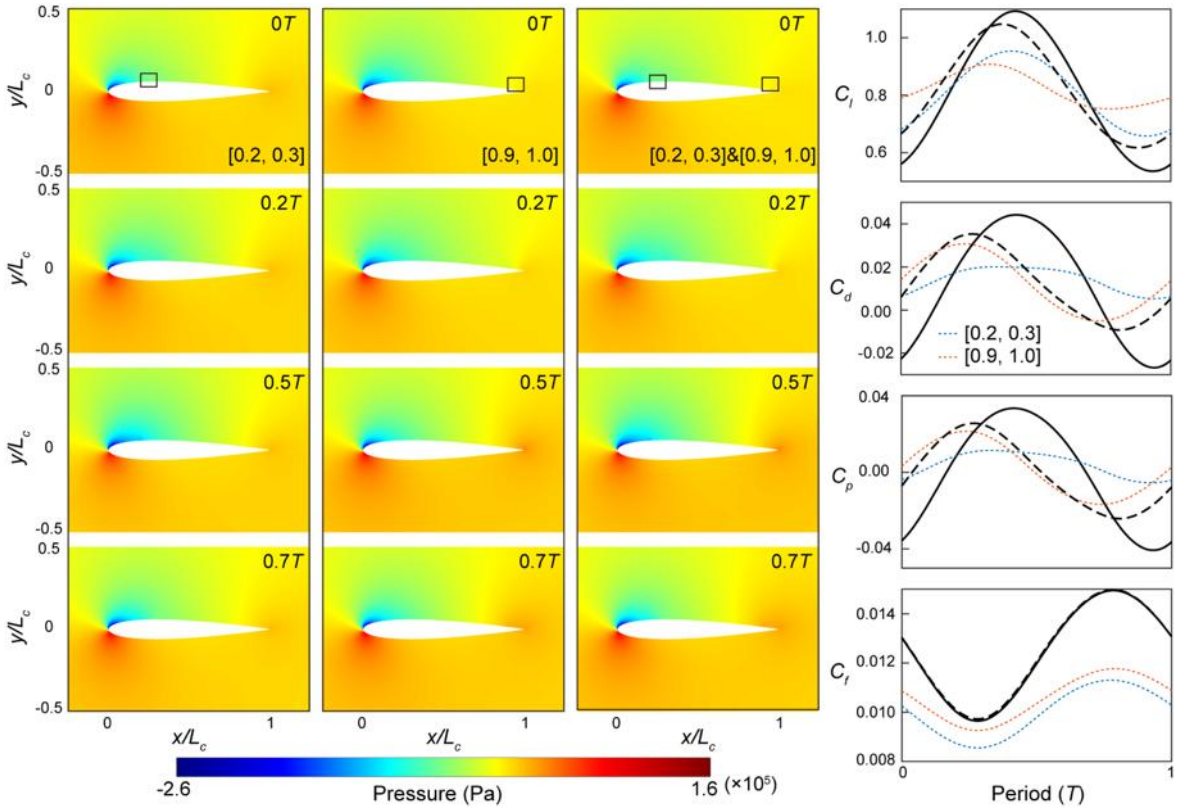

Figure 4-34 Arrangement including special region at TE on the upper surface when AoA=7.5º

4.6 PHASE EFFECT OF DTLMUW ON AIRFOIL PERFORMANCE

Based on the simulation results in the above sections, we have concluded that the combination of the streamlined shape and dynamic wall boundary with DTLMUW motion

can effectively reduce drag without compromising lift. And the drag reduction effect will be enhanced under the conditions of small AoA and large vibration area. In addition, we know that the periodic wall motion inevitably introduces periodic fluctuations on the flow and force distributions. Although these fluctuations do not impact the ultimate drag reduction effect, we aim to minimize the force fluctuations as much as possible to achieve optimal airfoil performance. Due to the linear superposition effect of multi-unit vibrations shown in section 4.5, we find that the combined force fluctuations can be decreased through adjusting the phase difference of force distribution between the different single units, which can be achieved by adjusting the motion phase within each unit. We have previously kept the motion state in the motion unit unchanged as equation (4-1). But according to the cutaneous ridge distribution during dolphin cruising, the skin oscillation motion on the upper and lower surfaces should be symmetric about the centerline of airfoil when reflected to our 2D model, indicating that there exists a phase difference of π in the wall motion of the two surfaces at the same position. Thus, in this section, we extend the area of vibration region and designate the vibration region $[x_s, x_e]$ on both upper and lower surfaces of foil as $[0.7L_c, 1.0L_c]$ when AoA is 0º, 7.5º and 10º. Two scenarios of same motion and symmetric motion (figure 4-35) are considered here simultaneously. In the same motion cases, the wall motion on both surfaces is identical with the form represented by equation (4-1). But in symmetric motion cases, inspired by the symmetry of dolphin skin ridges, we maintain the vibration motion on the upper surface unchanged as equation (4-1), while the motion of the lower surface is symmetric to the upper surface with respect to the airfoil centerline, expressed in the form of motion equation as

$$y_{w_{lower}} = y_{lower} + a\sin[k(x - ct) + \pi], \qquad (4-8)$$

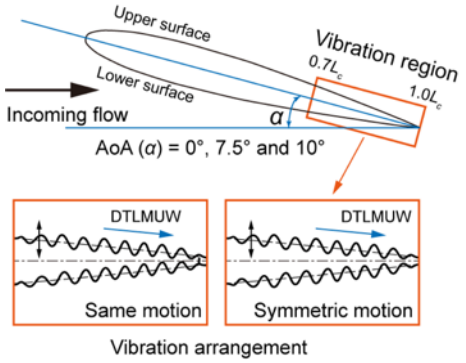

Figure 4-35 Schematic of two double vibration system undergoing the same and symmetric motion

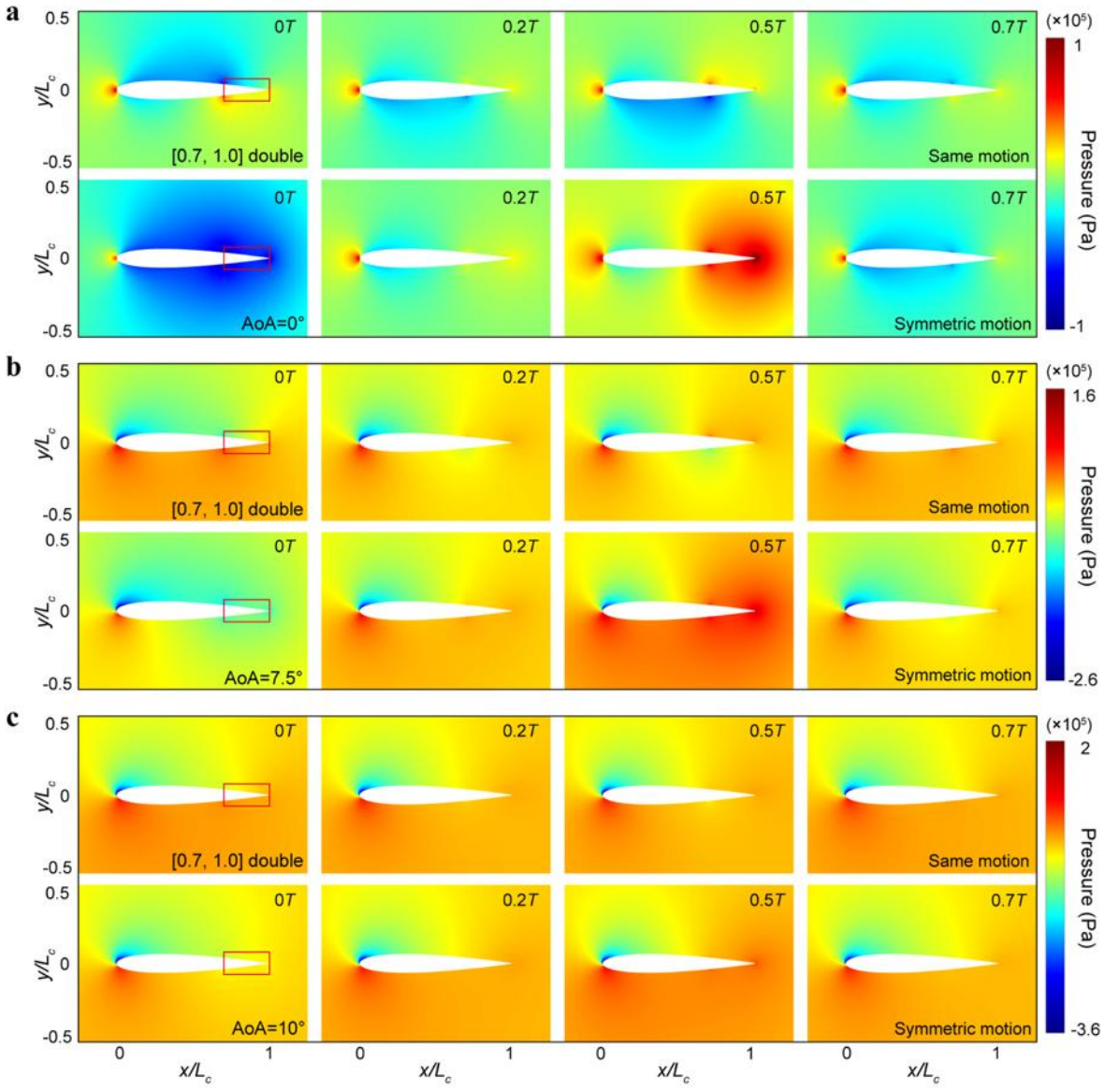

Figure 4-36 Comparison of pressure distributions between same and symmetric vibration motion (a) AoA=0º; (b) AoA=7.5º; (c) AoA=10º

Figure 4-36(a) illustrates a significant pressure difference between the upper and lower surfaces due to the modulation of motion within the vibration regions on both surfaces when AoA is 0º. Due to directly connecting the vibration region with the TE of the airfoil, the pressure distributions on the upper and lower surfaces mutually influence each other and are highly correlated with the pressure phase difference between the two surfaces. When the

motion is same, the pressure phase difference is 0, leading to a mutual cancellation of pressure between the two surfaces, reducing the intensity of pressure variations induced by the wall vibration. Conversely, the pressure phase difference is π under symmetric motion, resulting in identical distributions on the two surfaces, thereby enhancing the overall intensity of vibration-induced pressure variations. However, despite the increased pressure intensity in the symmetric motion cases, the symmetry of the pressure distribution between the upper and lower surfaces maintains the pressure difference near zero, greatly reducing the fluctuation of instantaneous lift but leading to an increase in drag fluctuation in a cycle compared to the same motion case when AoA=0º in figure 4-37. As AoA increases, the overall pressure distribution around the airfoil is no longer symmetric, and the pressure difference at the leading edge becomes more pronounced [figure 36(b) and (c)]. At this point, the pressure variations caused by wall vibration gradually weaken in the overall pressure field. But due to the symmetric motion arrangement, the vibration-induced pressure phase difference between the two surfaces remains close to zero, significantly reducing the instantaneous lift fluctuation. Moreover, as illustrated in figure 4-37, it is fascinating to note that the drag fluctuation under symmetric motion conditions gradually decreases compared to the same motion conditions with the increased AoA. Both lift and drag fluctuations in symmetric motion are smaller than in same motion under the large AoA conditions of 7.5º and 10º.

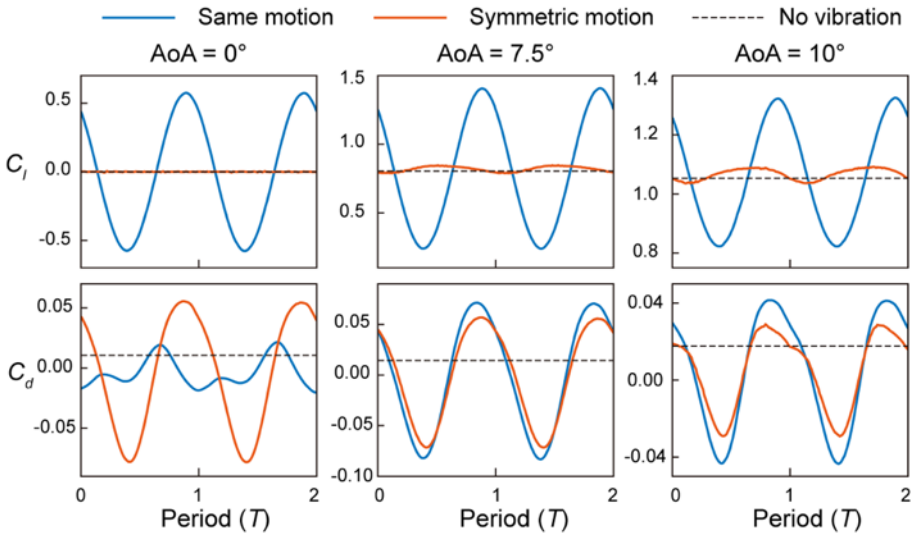

Figure 4-37 Time-varying lift (C_l) and drag (C_d) coefficients under different motion and AoA conditions

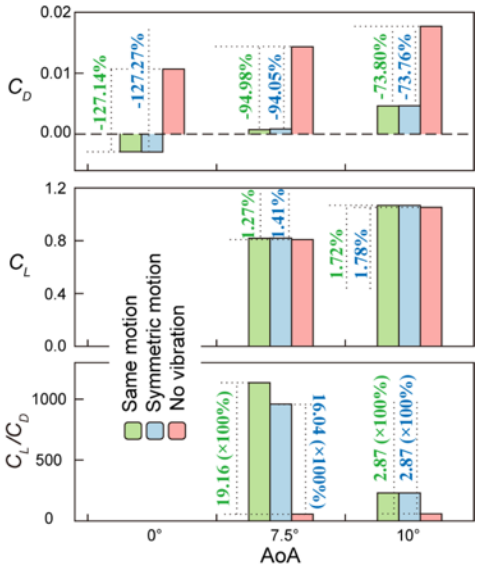

Figure 4-38 Improvement of airfoil performance

Although different arrangement of motion phases can lead to significant variations in the motion-induced pressure phase difference between two surfaces of airfoil, resulting in considerable changes in force fluctuations over a cycle, it will not affect the overall time-averaged forces acting on the airfoil under the conditions of unchanged motion form and vibration region position. As shown in figure 4-38, the effects of same and symmetric motion arrangements on lift and drag are nearly consistent. Therefore, a symmetric vibration distribution learning from dolphin skin offers a significant advantage on reducing instantaneous force fluctuations without compromising drag reduction effectiveness. The efficacy of drag reduction and airfoil performance improvement is remarkable. As shown in figure 4-38, the variation rates in time-averaged lift (C_L) and total drag (C_D) coefficients for the two scenarios are nearly identical: more than 94% and 73% drag reduction, accompanied by slight increases in lift coefficient, were achieved at AoAs of 7.5º and 10º, respectively. This results a significant improvement in lift-to-drag ratios (C_L/C_D), with increases of more than 19 and 16 times in the same and symmetric motion modes, respectively, at AoA=7.5º, and more than 287% at AoA=10º. Notably, as shown in figure 4-16, these variation rate can be further improved at lower AoAs, such as between 2º and 5º, which are typical angles of attack for aircraft during level flight [1,162]. In addition, it is worth noting that as the AoA decreases and approaches 0º, the total drag becomes negative, indicating that DTLMUWs

can not only significantly reduce drag but may even generate thrust at very low AoAs. Consistent with the conditions during actual dolphin cruising of small AoA, large coverage area and symmetric distribution of skin ridges, the addition of wall vibration can effectively reduce total drag, even convert drag into thrust, further suggesting that the existence of dynamic skin boundary in the form of micro-skin oscillation could be a crucial factor in achieving the excellent hydrodynamic performance in dolphins.

4.7 SUMMARY

Dolphins, being one of the fastest swimmers among animals, display outstanding hydrodynamic performance attributed to various factors such as their body shape, skin characteristic and secretions. Here, we focus on two key factors: the streamlined body shape and the dynamic skin boundary with LMUW motions inspired by the acoustic behavior and skin flexibility and sensitivity of dolphins, to study their combined effects. Numerical simulations are performed to investigate the influence of the addition of dynamic wall motion on airfoil performance. The results indicate that the near-wall velocity and pressure field are highly dependent on the wall motion forms, and the periodic flow variations induced by wall motion inevitably result in the force fluctuations. But the overall pressure distribution trend of the flow field around the airfoil is not altered by wall motion, coupled with the periodicity of motion, the lift on the airfoil will be symmetrically distributed around the original lift without wall vibration, leading to a very small impact on the time-averaged lift acting the airfoil before and after adding the wall LMUW motion. But the influence on the drag, especially for traveling LMUWs, cannot be ignored. Due to the existence of propagation characteristic in traveling LMUW cases, the wall motion-induced near-wall flow exhibits strong directionality in the trough region, downstream flow in downstream cases and reversed flow in upstream cases, which leads to an opposite phenomenon of pressure reduction, friction increase in downstream cases and pressure increase, friction reduction in upstream cases. And due to the dominant role of pressure in total drag, the downstream traveling LMUW can effectively reduce the pressure drag and ultimately achieve a reduction in total drag.

The advantage of total drag reduction induced by DTLMUW motion remains

unaffected within a certain range of AoA (0~18º in this chapter), but the extent of drag reduction decreases with an increase in AoA. When the AoA is near 0º, the addition of DTLMUW wall motion can induce the negative pressure, resulting in the excellent drag reduction performance. However, as the AoA increases, the pressure shows a converging characteristic towards the force under the no wall vibration state, causing the drag reduction effect to weaken. Different from the pressure, the addition of DTLMUW oscillation increases the magnitude of friction drag but does not significantly affect the trend of friction with AoA. Considering both two drag elements, the total drag reduction effect induced by the same wall motion is more pronounced under the condition of small AoA.

Due to the non-uniformity of forces on the airfoil surface from the LE to the TE, the drag reduction performance at different vibration region positions also be investigated. We firstly consider a single vibration case with the oscillation unit length of $0.1L_c$ and wall motion form of DTLMUW on the upper and lower surfaces of airfoil when AoA=0º and 7.5º. And we find that the total drag reduction can always be achieved regardless of where the single vibration is placed, but the minimum reduction effect occurs at the maximum thickness position. Particularly, the effectiveness increases away from the maximum thickness, especially at the tail end of the foil. But it is noticeable that as AoA increases, the flow separation occurs at the TE on the upper surface. The presence of flow separation will decrease the effectiveness of drag reduction induced by the addition of DTLMUW.

When we keep the wall motion equation unchanged, increasing the number of vibration units will lead to the cumulative effect of total drag reduction. But the arrangement of vibration units on the airfoil surface significantly influences the pressure distribution near the airfoil, resulting in different fluctuations in lift and drag within the period. When the vibration regions are discontinuous, the motion arrangement in multiple positions can be considered as a linear superposition of single vibration cases. However, the linear superposition relationship no longer be satisfied when the vibration region is continuous, and the motion-induced pressure fluctuations become more intense with the increase in vibration area. This situation can be alleviated when the oscillation region is directly connected to the tail end of foil. Although the degree of force fluctuations in a period has little impact on the final time-averaged drag and lift acting on the airfoil, considering the airfoil performance, we naturally hope to minimize the periodic force fluctuations while

maintaining the time-averaged effect of constant lift and reducing drag, which can be achieved by controlling the vibration area and position, and adjusting the motion phase between different motion units. Based on this, inspired by the distribution of cutaneous ridges on dolphin skin, we also construct the symmetric vibration motion (with motion phase of π) on the upper and lower surfaces simulations and find that it can effectively reduce the instantaneous force fluctuations induced by wall vibration, especially the lift acted on the foil, without compromising drag reduction performance, and thus improving the airfoil performance significantly.

In summary, the combination of streamlined shape and dynamic boundary with DTLMUW motion can effectively achieve a reduction in total drag, offering new design possibilities for improving the airfoil performance in engineering applications. Under conditions of small AoA (near 0º) and large vibration area, it can even induce negative drag, successfully converting drag into thrust. Moreover, when the vibration motion on the upper and lower surfaces is symmetric about the centerline of foil, the instantaneous lift fluctuations caused by wall motion can be greatly reduced, resulting in a higher stability. Interestingly, these three conditions that greatly enhance drag reduction performance of the combination of streamlined shape and wall motion, align perfectly with the biological habits of dolphins of maintaining a small AoA close to zero during their cruising process and the skin ridges covering most of its body and symmetric about the body's centerline. It can be inferred that the two-factor combination (body shape and dynamic skin boundary) may indeed provide a significant contribution to their high-speed and low-resistance behaviors. Therefore, this research, on one hand, delved deeper into the mystery of the excellent hydrodynamic performance of dolphins; on the other hand, provides potential new design inspirations for improving airfoil performance, which carries both scientific and engineering research value.

Chapter 5 APPLICATION OF LMUW SKIN MOTION IN ACTUAL SWIMMING

5.1 INTRODUCTION

The LMUW-induced drag reduction on a flat plate and a fixed airfoil has been demonstrated. Despite the significant drag reduction provided by LMUW, it is difficult to serve as the primary source of propulsion. Dolphins swim by generating thrust through the formation of a reverse von Kármán street, a thrust-type wake as a central momentum jet flow to propel the dolphin's body moving forward, from the action of the caudal flukes [93]. For underwater vehicles, propulsion is achieved through propellers or other propulsion systems [163–166]. Due to the high-frequency, micro-shape parameters of skin LMUW, its influence on the overall flow field is limited in scope. Therefore, theoretically, the addition of LMUW should not affect the flow field generated by the undulation of a dolphin's tail or the propellers of underwater vehicles. However, the variations in the near-wall flow around the vibrating area result in favorable drag reduction characteristics, providing an excellent design option to improve propulsion efficiency and optimize swimming or propulsion performance.

In this chapter, considering that skin LMUW vibrations occur during actual dolphin swimming, and the source of excitation for this motion (the click signals) also happens during real swimming for purpose like hunting and echolocation, we explore the application of such skin LMUW vibrations to the actual swimming process. Instead of simply imposing a fixed incoming flow velocity at the inlet, the thrust generation can be achieved through giving a motion of tail undulation, thus propelling the streamlined body forward. The skin LMUW vibrations occur on the front side of the body, near the excitation source. By combining the effects of two different undulation types, we examine the impact on the overall swimming propulsion and investigate the role and value of skin LMUW vibrations in this real-world propulsion scenario.

5.2 2D SWIMMING MODEL WITH LMUW

5.2.1 Physical problem

Dolphins rely on the vertical (up and down) fluke oscillations to propel themselves. When observed from the side, the fluke motion is in the form of a sinusoidal pathway and is symmetrical about the longitudinal axis of the body. The powerful motion generated by the tail flukes about the center of gravity also induces a corresponding moment in the front part of the body. These pitching movements at the beak result in a vertical oscillation amplitude of 1-7% of body length. And the motion of the beak and tails are pitched up or down simultaneously, indicating that the dolphin body can act as an elastic but not a rigid beam [100,167]. But because the motion of beak are smaller than the fluke movements, we only consider the tail fluke motion here for simulating fish propulsion. As mentioned by Wang et al. [168], we define a tail undulation region, with a length of λ, where the body undulates to achieve propulsion, while the rest of the body remains stationary. Here, we simplify the actual fish body propulsion model into a 2D streamlined model (NACA0012), as shown in figure 5-1. The undulation region is one-third of the body length ($\lambda = L/3$), and the maximum undulation amplitude of the tail h is $0.08L$. The tail fluke motion in the undulation region is defined as follows:

$$y = (ax^2 + bx)\sin(\omega t), \qquad (5-1)$$

where t is the time of strokes, $\omega = 2\pi f$, and f is the undulation frequency. The coefficients a and b can be calculated as $a = (2/3)\,h/\lambda^2$ and $b = (1/3)\,h/\lambda$, respectively.

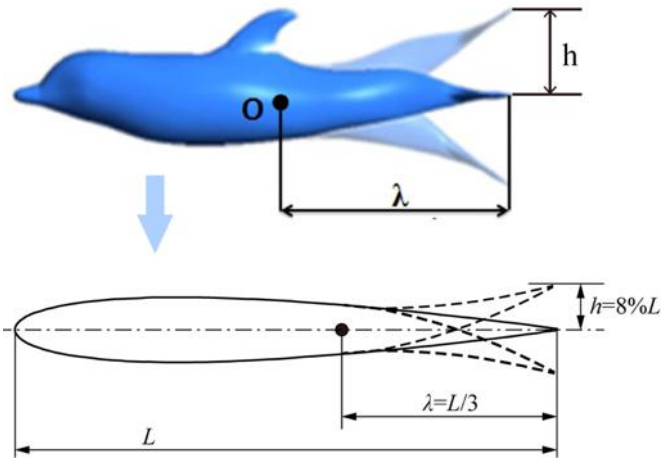

Figure 5-1 Tail fluke motion

5.2.2 Numerical setting

This work focuses on a fish-inspired self-propulsion in an incompressible viscous flow. The 2D unsteady, incompressible N-S equations are governing equations. The simulation comprises a 2D flexible deformation of streamlined body. To account for the changing domain caused by the body's flexible motion, the dynamic mesh model is employed. The entire system is calculated using the ANSYS Fluent software 2021. In this study, a one-degree-of-freedom (1-DOF) self-propulsion is implemented, allowing the streamlined model to perform periodic undulatory motions while swimming along the streamwise direction [169]. The undulation motion is a prescribed motion [equation (5-1)], but the swimming motion itself is unprescribed, meaning that the swimming speed depends dynamically on the net thrust generated at any given time. Here, we can calculate the swimming velocity U_s according to the Newton's law, given by

$$F_t = m\frac{\mathrm{d}U_s}{\mathrm{d}t}, \qquad (5-2)$$

where F_t is the thrust acting on the fish body, and the instantaneous swimming velocity, U_s, represents the velocity of the fish model at any given moment. For simplicity, the fish mass m is set to 1kg for convenience. The swimming velocity is determined iteratively at each time step, using the defined equations above in this model.

The fluid domain is a rectangular zone, discretized using structured meshes. As shown in figure 5-2, zone 1 as the background mesh, is always static without mesh motion. Zone 2 contains the fish body. All the dynamic mesh motions, including the tail flukes and skin microvibrations, occur in this region. In the simulation process, the swimming velocity U_s is not directly applied to the streamlined model itself but is instead imparted to the entire zone 2. At each time step, zone 2 moves forward at the calculated swimming velocity U_s to simulate the swimming motion of fish. Despite the whole movement of zone 2, it does not have an effect on the simulation, as the initial boundary conditions remain unaffected by the mesh configuration. The two zones (zone 1 and zone 2) are overlapping but independent, connected by an overset interface. The overset interface facilitates the connection between the two zones by interpolating cell data in the overlapping regions. The overset interface offers several advantages. One key benefit is that the motion mesh (zone 2) and static mesh in zone 1 can be generated independently with fewer limitations. Importantly, the

background zone is static and does not require dynamic mesh models, which reduces simulation costs. Compared to controlling deforming meshes across a large computational domain, managing the deformation of meshes in a smaller region (zone 2) is more efficient. Local region near the fish (zone 2) is filled with finer and more meshes to capture detailed flow characteristics and maintain the mesh quality despite the deforming motion. Meanwhile, the static mesh in zone 1 does not nees a high mesh density, reducing the computational cost of calculating the fluid filed far from the motion model. The use of overset interface represents a balance between computational cost and simulation accuracy, enabling the efficient modeling of localized flow dynamics while maintaining reasonable simulation times [169].

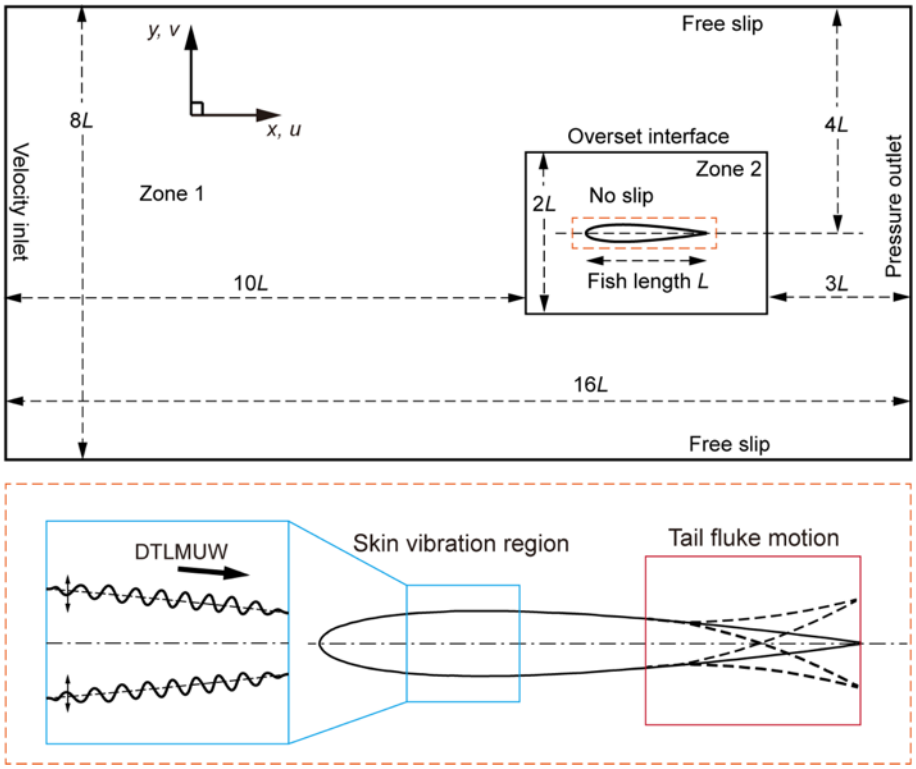

Figure 5-2 Sketch of the fish swimming model with DTLMUW

Due to the movement of zone 2 in the simulation, figure 5-2 can only indicate the initial setting in the simulation. The computational domain is 16L long and 8L wide, with the inlet and outlet initially located 11L and 4L away from the fish, respectively. The velocity-inlet boundary is used to the left boundary, with an initial inlet velocity of 0.01 m/s. This inlet

velocity here is only used to indicate that the environment of dolphin swimming is complex and not a still water environment. The actual swimming velocity is achieved mainly relying on the undulation of its tail. The pressure-outlet boundary is applied to the right boundary. The upper and lower boundaries, located roughly 4L away from the fish, are set to free-slip condition. No-slip boundary condition is applied on the fish body. Since the position of fish body changes during the simulation, we define the tail fluke motion in the simulation as:

$$y_{tail} = y + \{a[(x - x_s) - (L - \lambda)]^2 + b[(x - x_s) - (L - \lambda)]\}\sin(\omega t), \qquad (5-3)$$

where x_s is the swimming distance of the fish body under the self-propulsion, and the undulation frequency of tail fluke motion is set as 2 Hz here. In order to investigate the influence of LMUW on the actual dolphin swimming, we also define a skin vibration region at the front part of the streamlined body. The two motion regions (skin motion and tail region), as illustrated in figure 5-2, do not interfere with each other. Downstream traveling LMUW are used here, and the skin oscillation equation follows equation (4-4) in chapter 4. RANS (SST k-ω) modeling is employed for all the simulations here. We firstly calculate the fish swimming for 20 tail fluke periods (T_{tail}) with a time step of T_{tail}/1000. After that, we consider adding DTLMUW on body skin to investigate the swimming performance under the combined effects of both two motions.

5.2.3 Verification and validation

A C-type mesh was employed with more than 100 grids clustered to the fish body. The height of the first mesh layer adjacent to the wall surface was set to 0.002 mm to guarantee $y^+ \approx 1$. An evenly spaced grid with 4098 nodes (Basic grid in table 5-1) was initially used in the streamwise direction along the fish surface. In order to ensure an adequate mesh and effective computational methods, we initially utilize the basic mesh to compute the swimming velocity U_s and distance. And then, a refined evenly spaced grid with 7808 nodes on the fish body (Fine grid in table 5-1) is also provided. The nodes of background mesh also increase accordingly. The swimming speed and distance under the two grids have been compared in figure 5-3 and the difference is found to be negligible, indicating the basic grid, as shown in figure 5-4, is sufficient to monitor the swimming process. In addition, we also compare the swimming velocity under our basic grid and numerical setting with the simulation results of Wang and Wu [170]. As illustrated in figure 5-5, a favorable consistency

can be obtained, especially after 10 periods. Both the results indicate that the simulations based on the basic grid system and our boundary settings can capture the key parameters in dolphin swimming. As for the mesh density in the skin vibration region, we have already validated it in chapter 4. Here, we use the same mesh density arrangement.

Table 5-1 Grid information for verification of mesh independence

Grid	Component mesh (zone 2)		Background mesh (zone 1)	
	Nodes on fish surface	Grid quantity	Nodes on boundary (x-direction) × (y-direction)	Grid quantity
Basic grid	4098	847440	832×388	317507
Fine grid	7808	1582020	1150×388	439301

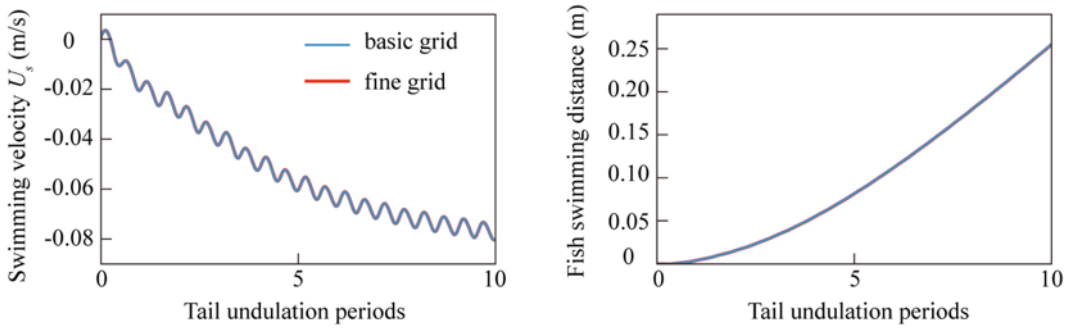

Figure 5-3 Mesh verification

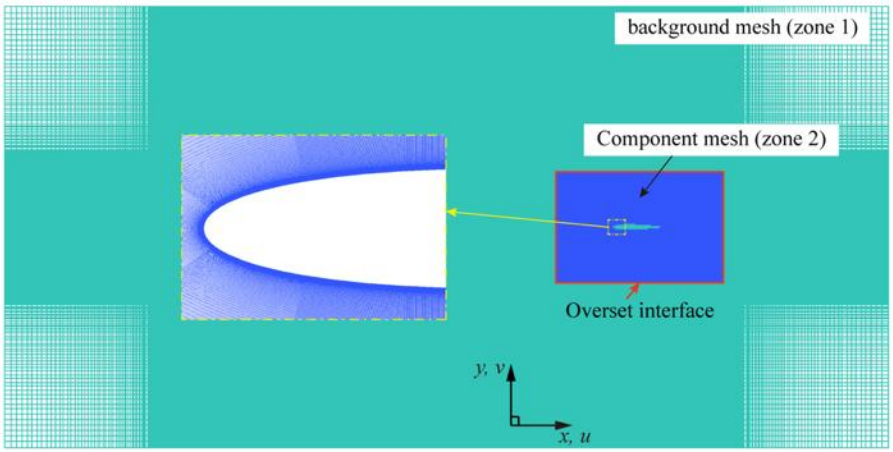

Figure 5-4 Grid system

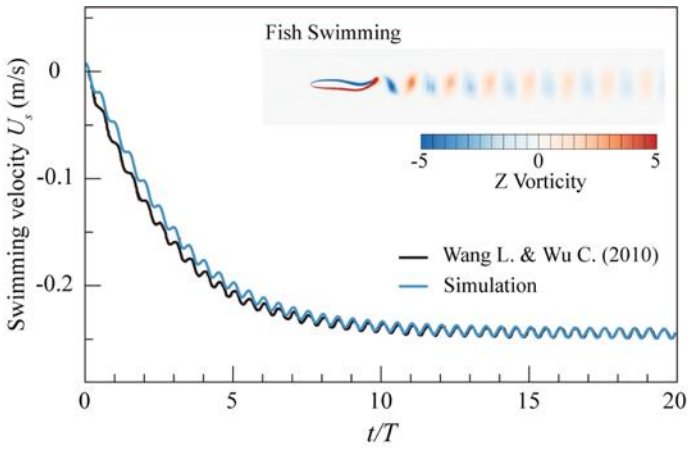

Figure 5-5 Validation. The z-vorticity is defined by $[\partial u_y/\partial x - \partial u_x/\partial y]$.

5.3 INFLUENCE OF DTLMUW ON SWIMMING

5.3.1 Transient effect of skin DTLMUW

From figure 5-5, we can see that it takes some time for the fish body to transition from the start of its swimming to a relatively stable state. Therefore, we first calculate 20 tail fluke cycles in the absence of skin dynamic behaviors and with a completely smooth surface, allowing the fish to reach a steady swimming state. During this process, the fish swimming velocity is shown in figure 5-6. And then, at the moment of t=20T_{tail}, skin DTLMUW motion is introduced in the skin vibration region [0.2L, 0.3L]. The shape parameters for DTLMUW are the same as described in the previous chapter and will not be repeated here. The wall motion equation follows equation (4-4). The skin microvibrations also last for 20 cycles, and by changing the vibration frequencies, we can obtain different velocity distributions, which are displayed in figure 5-7.

In figure 5-7, t' is the duration of skin vibration, defined as t'=t-20T_{tail}. And T_{LMUW} is the period of DTLMUW. We notice that when the frequency of skin microvibration is sufficiently high, especially in the ultrasonic frequency range, the addition of skin vibration can effectively accelerate the swimming, and this acceleration effect increases with the frequency. As analyzed in previous chapters, DTLMUW leads to an increase in friction force but a decrease in pressure force. As illustrated in figure 5-8(a), friction force increases while pressure force decreases monotonically as the skin vibration frequency increases. In this

high-frequency skin vibration cases, pressure force dominates, resulting in a reduction in the total drag. Here, the pressure corresponding to ultrasonic frequencies is negative strongly, which can offset the friction drag and provide thrust for the fish, thereby increasing the swimming speed. However, we note that at a vibration frequency of 1 kHz, the total drag induced by skin vibration increases [figure 5-8(b)], causing a negative impact on the fish swimming (figure 5-7). This can be explained by the first and second drag reduction region mentioned in chapter 2. We previously noted that the skin traveling LMUW generates a wave

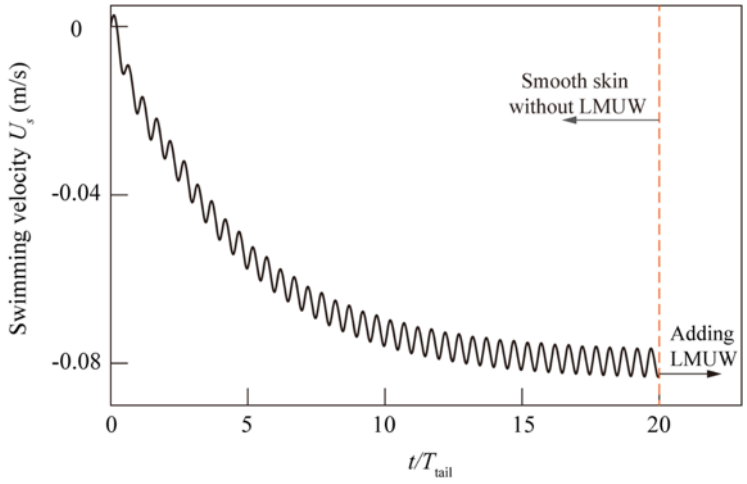

Figure 5-6 Swimming velocity without skin DTLMUW

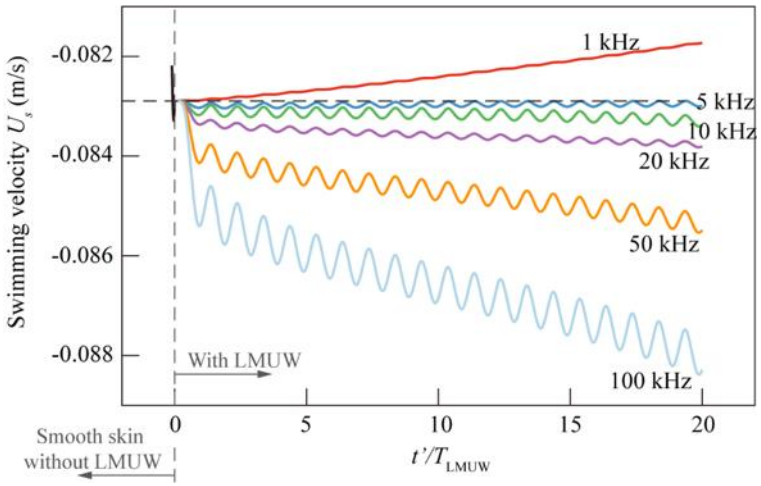

Figure 5-7 Transient effect of skin DTLMUW

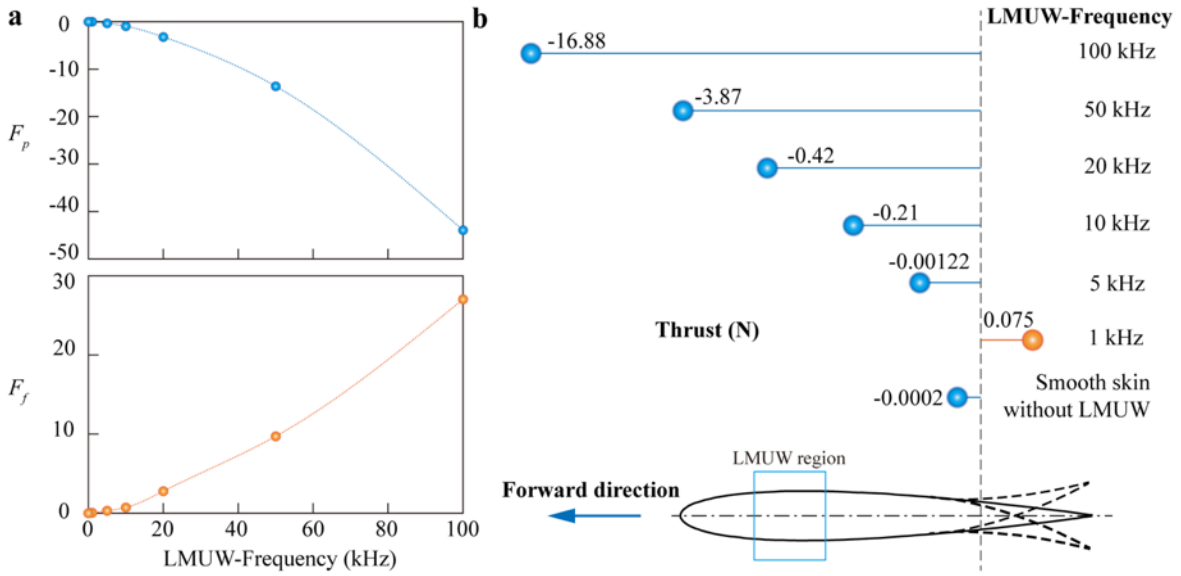

Figure 5-8 Distribution of forces acting on fish body

(a) Pressure and friction distribution induced by DTLMUW; (b) Total thrust effect

speed c, which creates a relative velocity ξ between the external flow (or the fish swimming speed). The second drag reduction region, dominated by pressure, covers most of the region where ξ is larger than 0. However, there exists a small region between the first and second drag reduction region where the total drag increases (figure 2-14). Therefore, if c is small and ξ does not enter the second drag reduction region, the total drag will increase, which is unfavorable for the swimming (such as the case of 1 kHz here). In contrast, the relative velocity induced by other frequencies here are large enough to enter the second drag reduction region, thus accelerating the fish swimming.

5.3.2 Effect of skin DTLMUW during a complete tail fluke

The click signals are considered the excitation source that stimulates dolphin skin to produce microvibrations. However, it should be noted that, based on the measurement results [127], the click signals do not exist continuously but rather in the form of pulse signals, as shown in figure 5-9(a). If we calculate based on the tail fluke frequency of 2 Hz used in this chapter, multiple click-signals (5~7) will occur within one tail undulation cycle. Each sound signal can act as a small excitation source to drive the micro-oscillations on dolphin skin, thus forming multiple pulsed skin oscillations within one tail fluke motion. Ideally, as

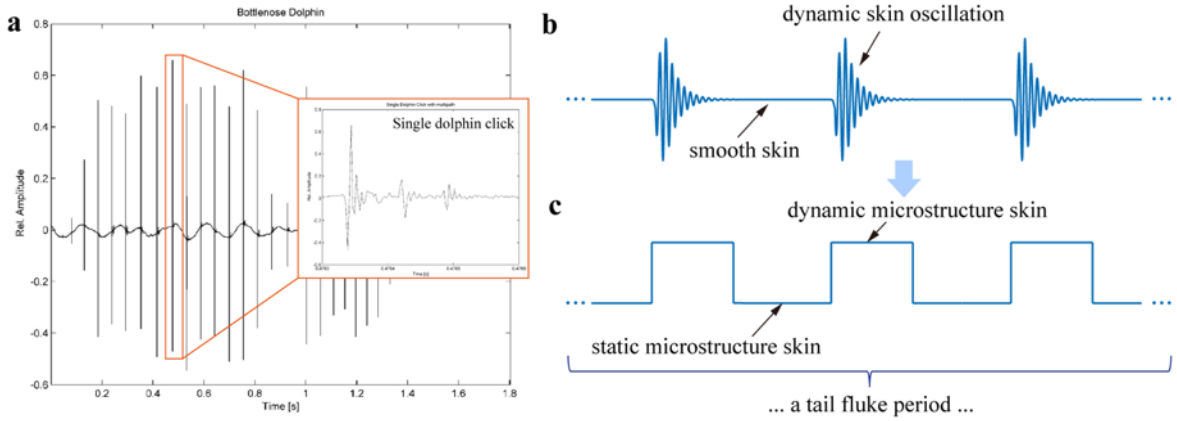

Figure 5-9 Excitation of dolphin click signals

(a) Dolphin's click signals [127]; (b) Ideal skin motion state; (c) Simplified skin motion state

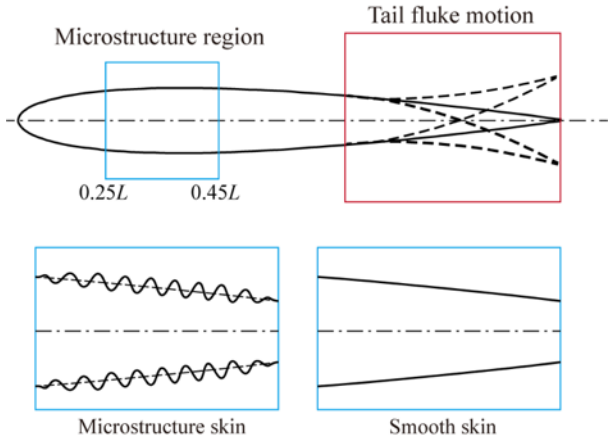

Figure 5-10 Microstructure skin and smooth skin

shown in figure 5-9(b), we believe that when the dolphin does not emit a click, its skin should be smooth. After a click signal is emitted, dynamic skin micro-oscillations begin to form on the originally smooth skin surface, and after the click disappears, the skin oscillations gradually decay until the skin returns to a smooth state. However, in reality, this situation is difficult to achieve in simulations, especially the process of skin oscillation decay to smoothness, where some microstructures are always retained, disrupting the originally smooth skin state. To solve this problem, we simplified this skin motion state shown in figure 5-9(c). That is, we assume that the dolphin skin already has microstructures, and when the click signal is emitted, the previously stationary microstructures begin to move in the form of traveling waves. When the sound signal stops, the microstructures cease movement and

return to a stationary state. This method is easier to implement in simulations and is less affected by the errors introduced by numerical simulations. Therefore, we firstly set a section of the front part of the fish body with a microstructure region $[0.25L, 0.45L]$, where microstructures exist on the skin surface (figure 5-10). The shape parameters of microstructures are consistent with the LMUW shape parameters mentioned earlier. Here, we first compare the effects of smooth skin and stationary microstructure skin on swimming. As shown in figure 5-11, we found that the difference between the two skin is not significant. And the swimming velocity corresponding to the two cases is in a great agreement, which is consistent with previous studies concluding that the stationary microstructures on dolphin skin do not greatly impact the overall swimming and drag characteristics of the dolphin [105]. Here, the z-vorticity in figure 5-11 is calculated by $\left[\partial u_y/\partial x - \partial u_x/\partial y\right]$.

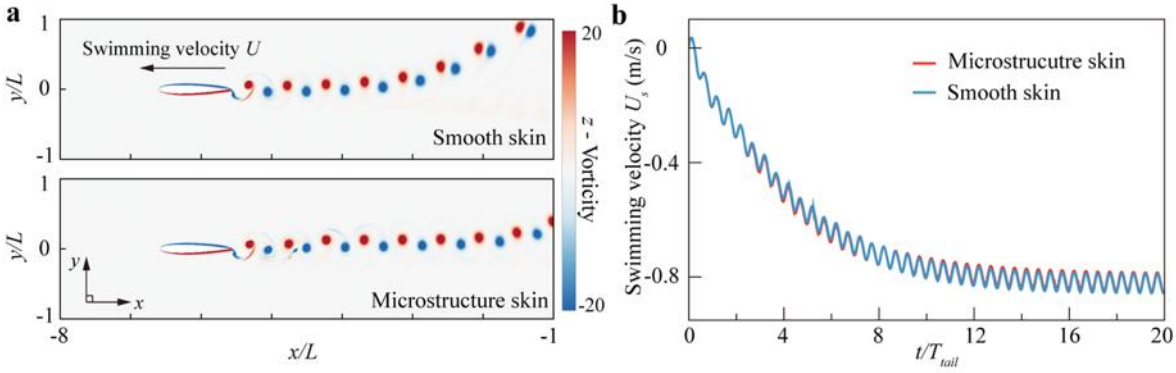

Figure 5-11 Comparation of swimming state between smooth and microstructure skin

(a) Flow state of fish swimming; (b) Distribution of swimming velocity

After several skin vibration cycles, the mesh quality near the microstructure skin tend to degrade. Due to this limitation, we have so far only completed simulations where one dynamic skin oscillation pulse is added within a tail fluke period. Figure 5-12(a) displays three scenarios: the first is a completely static microstructure skin; the second involves adding a short-time dynamic skin vibration, with the vibration lasting 20 cycles at a frequency of 100 kHz; and the third scenario adds a long-time microvibrations, lasting 40 cycles at the same frequency of 100 kHz. The results in figure 5-12 indicate that the addition of skin DTLMUW, regardless of duration, leads to an increase in swimming velocity during the skin microvibration period. The longer the vibration duration, the more pronounced the

speed increase. However, due to the extremely high vibration frequency, the time occupied by either the short- or long-time microvibrations within the entire tail fluke is only a brief moment. Therefore, as shown in figure 5-12(b-c), adding skin DTLMUW causes an instantaneous speed increase.

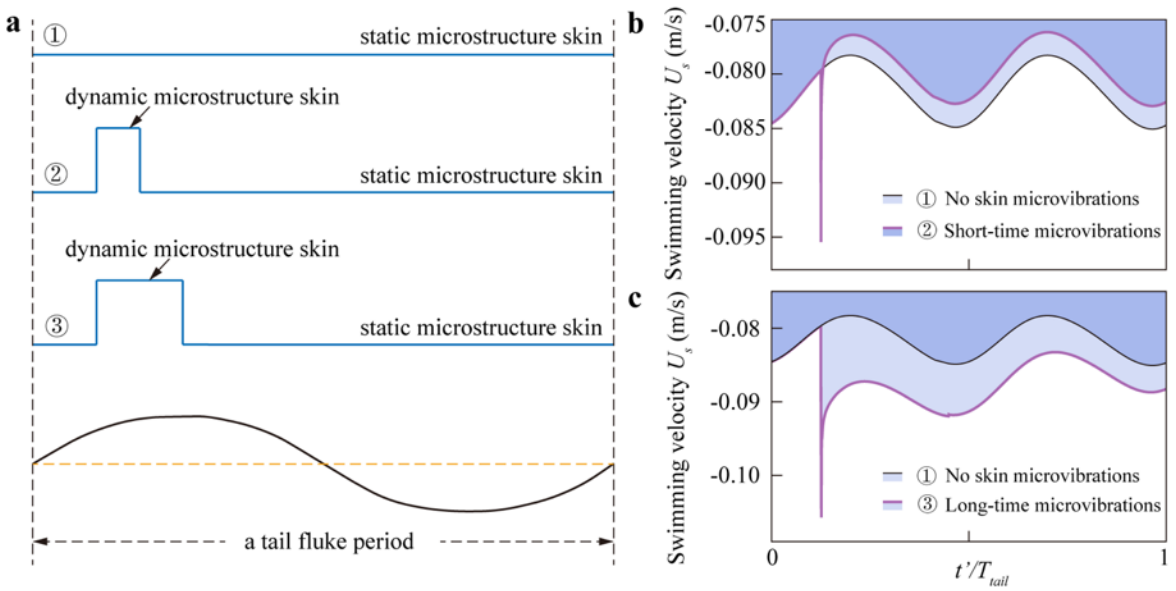

Figure 5-12 Effect of skin DTLMUW motion during a complete tail fluke

(a) Skin motion state in a tail fluke; (b) Swimming velocity after adding the short-time skin DTLMUW; (c) Swimming velocity after adding the longt-time skin DTLMUW

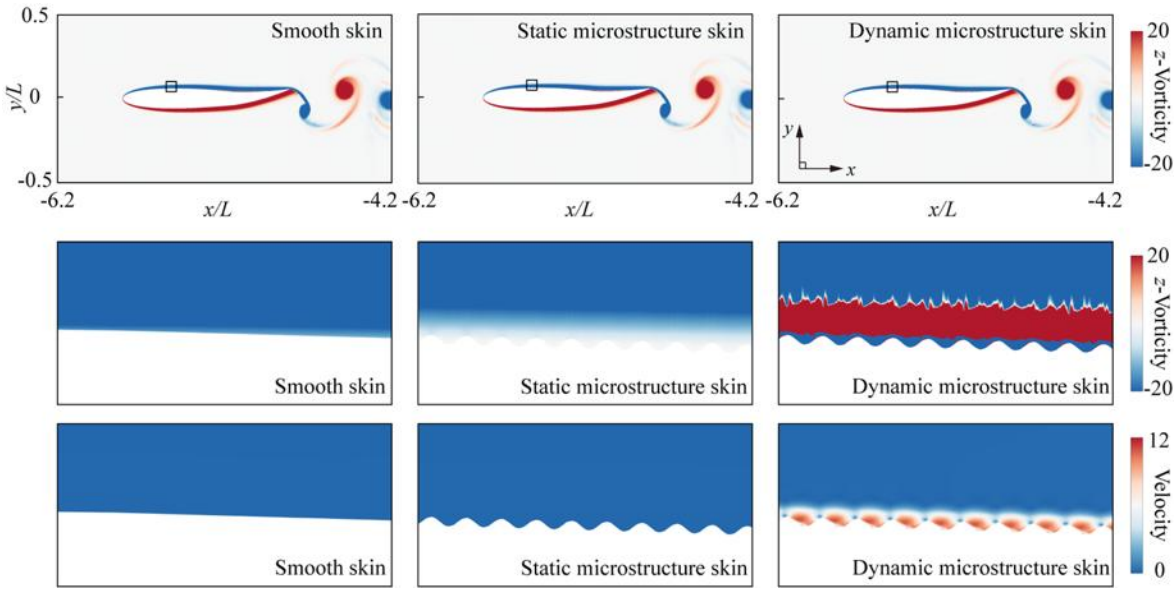

Figure 5-13 Near-wall flow distributions under different skin conditions

However, the addition of dynamic skin DTLMUW motion generates a high-speed flow near the vibrating skin in the streamwise direction (figure 5-13), which increases friction drag. When the skin microstructure transitions from dynamic to static, the pressure drag induced by the skin vibration disappears immediately, but the vibration-induced high-speed flow does not vanish instantly; instead, it gradually decays over time, as shown in figure 5-14. This means that the friction drag caused by the high-speed flow continues to affect swimming until it fully decays. Consequently, while adding skin vibrations results in an immediate speed increase, once the vibration stops, the high-speed flow will cause a speed attenuation shown in figure 5-12(b-c). This speed attenuation is related to the near-wall distribution induced by the dynamic skin microvibrations. Given the periodic nature of the vibration, we assume that this speed attenuation is constant under the same vibration frequency and shape parameters, regardless of the number of vibration cycles. Therefore, when the skin vibration-induced speed increase is smaller than this attenuation value, the addition of skin vibration has a negative impact on the overall swimming, such as the short-time microvibrations shown in figure 5-12(b). But when the duration of the skin vibration is extended, the resulting speed increase can offset this attenuation, leading to an overall increase in swimming speed, allowing the fish to cover more distance within a tail fluke cycle.

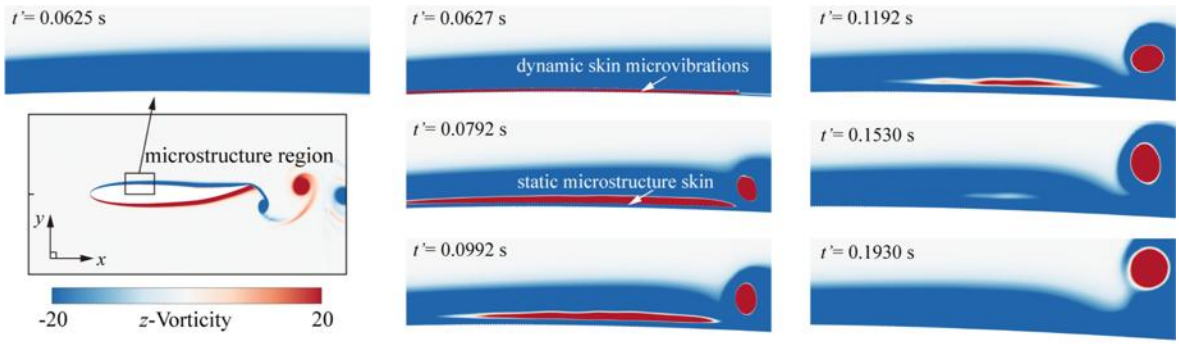

Figure 5-14 Attenuation of skin microvibration-induced near-wall high-speed flow

The propulsive performance of this swimming is also investigated according to certain parameters: mean thrust, mean swimming velocity, input power and propulsive efficiency. The propulsion of fish primarily relies on the undulatory motion of the tail. To sustain this

movement, a certain amount of input power is required, given by

$$P_{in} = \int p \frac{\mathrm{d}y_{tail}}{\mathrm{d}t} \mathrm{d}x \,. \tag{5-4}$$

The actual output power used for propulsion can be expressed as

$$P_{out} = \langle F_t \rangle \langle U_s \rangle, \tag{5-5}$$

where $\langle * \rangle$ denotes the time-averaged quantities. Thus, propulsive efficiency of the fish body is given as

$$\eta = \frac{P_{out}}{P_{in}} = \frac{\langle F_t \rangle \langle U_s \rangle}{\langle P_{in} \rangle}. \tag{5-6}$$

Table 5-2 presents the parameters related to propulsion performance. The propulsion efficiency of both smooth and microstructure skin is nearly identical, which once again indicates that the static microstructures on dolphin skin have a very limited impact on its swimming performance. However, the addition of skin dynamic DTLMUW motion has a significant effect on efficiency. In the case of short time microvibrations, the acceleration caused by skin DTLMUW is insufficient to compensate for the deceleration that occurs after the vibration stops, due to the high-speed boundary layer induced by the skin vibrations. Thus, the overall swimming speed decreases, leading to a reduction in propulsion efficiency. Conversely, in the case of long time microvibrations, the speed increase induced by skin DTLMUW offsets the near-wall flow induced speed attenuation, resulting in an overall increase in swimming speed and thus an increase in propulsion efficiency. Since we believe that the skin microvibrations are excited by the click signals and that is not necessary to maintain these skin vibrations for a long time, when considering propulsion efficiency, we only need to account for the power required to sustain the tail movement. Moreover, in this study, we applied only one dynamic skin microvibration pulse within a tail fluke period. In reality, dolphins may experience multiple skin microvibration pulses excited by the click signals within one tail motion cycle, which suggests that the actual swimming efficiency of dolphins may be even higher.

Table 5-2 Parameters related to propulsion performance

	$\langle F_t \rangle$ (N)	$\langle U_s \rangle$ (m/s)	$\langle P_{in} \rangle$ (W)	η
Smooth skin	-0.0104417	-0.09084339	0.001598564	0.5934
Microstructure skin	-0.0106	-0.09016998	0.001594525	0.5994
Short time microvibration	-0.006835	-0.08979577	0.001581382	0.3881
Long time microvibration	-0.015274	-0.0908332	0.001635121	0.8485

5.4 SUMMARY

Due to the high-frequency, micro-scale characteristics of skin LMUW vibration, when the skin vibration region is not directly connected to the tail fluke region, the skin vibrations do not significantly impact the propulsive motion induced by the tail fluke. However, as we analyzed previously, the skin microvibrations themselves have a notable effect on the near-wall flow near the vibration region, inevitably causing some variations to the overall flow and force involved. When the skin microvibrations are added, the strong negative pressure force generated by DTLMUW can effectively reduce drag and increase thrust, thereby accelerating the swimming of the fish body.

However, it is important to note that this negative pressure appears with the onset of skin vibrations and immediately disappears when the vibrations stop. But the near-wall boundary changes caused by the skin vibrations take time to revert to their original non-vibration state. The slow decay of the DTLMUW-induced high-speed near-wall flow will increase friction drag to some extent, leading to a speed attenuation after the skin vibrations stop, which compensates for the consumption of the high-speed boundary flow. This also means, if we want to achieve an overall increase in swimming speed, the speed increase brought by dynamic skin microvibrations must be sufficient to offset the deceleration after the vibrations cease. It is interesting that this speed attenuation is determined by the DTLMUW-induced high-speed near-wall flow and is related to the vibration frequency and shape parameters. Therefore, if the vibration parameters remain unchanged, the resulting speed attenuation will reach a fixed value regardless of the duration of the vibration cycle due to its periodicity. Thus, increasing the duration of skin microvibrations effectively eliminates the negative effects caused by speed attenuation. Additionally, we calculated the propulsion performance of the fish swimming, and the results show that under the excitation of long time microvibrations, propulsion efficiency significantly improves. But due to the limitation of grid quality, we only achieve the addition of one dynamic skin microvibraiton pulse per tail fluke period in this study. However, based on the distribution of click signals, we speculate that there should be as least 5 to 7 click pulses within one tail cycle, meaning multiple dynamic skin microvibration pulses. Therefore, the actual swimming efficiency of the fish swimming may further increase with the number of pulses.

Chapter 6 CONCLUSIONS

6.1 SUMMARY OF KEY FINDINGS

This thesis focuses on the effects of dynamic boundaries caused by the microvibrations on dolphin skin on its drag reduction performance. In this study, we hypothesize that the click signals of dolphin serve as an internal excitation source to drive the dynamic oscillation on its skin, in the form of longitudinal micro-ultrasonic wave (LMUW). A comprehensive CFD study involved a series of LES- and RANS-based simulations is undertaken to investigate the LMUW-actuated turbulent flows, dynamic boundary layer model and drag reduction effect. The main findings are summarized as follows:

(1) The dynamic boundary results in a flow and force distribution that is entirely different from that of a stationary boundary. Due to fluid viscosity, the near-wall flow is driven by the moving wall, resulting in different flow effects depending on the wall motion mode. As mentioned in the thesis, downstream traveling LMUW can drive near-wall fluid to flow in the streamwise direction; upstream traveling LMUW leads to a reversed near-wall flow, while standing LMUW induces near-wall vortices. These different near-wall flow inevitably leads to variations in the drag acting on the dynamic boundary. Specifically, the upstream traveling LMUW creates a reversed wall shear, resulting in a negative friction drag (i.e., thrust). The downstream LMUW produces a negative pressure drag (i.e., thrust) against an increased friction drag to overcome the trade-off between friction and pressure drag, potentially reducing the total drag. Standing waves, to some extent, reduce friction drag and increase pressure drag, but since they lack the propagation characteristics, the change in total drag is relatively small.

(2) This dynamic boundary offers a new approach to drag reduction, enabling active manipulation of the magnitude and direction of near-wall flow by altering the LMUW motion modes. This approach allows for changes in both the magnitude and direction of drag forces, rather than simply reducing the force value as in traditional methods. Based on this, the reduction in total drag dominated by pressure in the case of downstream traveling

LMUW can create a new drag reduction mechanism, where pressure can contribute to thrust by altering the direction of pressure force. And thus, even with an increase in friction drag, the total drag can still be reduced.

(3) This drag force distribution is highly correlated with the near-wall flow velocity distribution. Considering the periodicity of the wall motion, a theoretical velocity model for the dynamic boundary layer based on Fourier series is established, being verified to be capable of reasonably capturing the essential fluid flows and analytically correlating the LMUW-excited near-wall turbulent flow with the friction- and pressure-drag reduction by comparing with simulations results. The coefficient functions in this model play a dominant role in determine both the friction and pressure drag, and their corresponding theoretical differential equations have also been provided. By analyzing these equations of coefficient functions, the distributions and trends of drag forces on the dynamic boundary can be evaluated, thereby providing a theoretical foundation for the design of drag reduction using the dynamic wall motions.

(4) The combination of dynamic skin microvibrations with the streamlined body shape of dolphin demonstrates significant drag reduction advantages. The application of downstream traveling LMUW on the streamlined shape can effectively reduce drag without affecting lift, thereby improving the lift-to-drag ratio. Moreover, the flexible control over the location and motion phase of the wall LMUW motion on the foil surface can further contribute to some additional optimization goals, such as enhancing drag reduction performance and improving stability. This presents great potential for optimizing the airfoil performance. In addition, although the addition of skin microvibrations significantly affects near-wall flow, it does not impact the overall macroscope flow field. This means that during actual dolphin swimming, the presence of skin microvibrations will not significantly affect the propulsion effect originally generated by tail flukes. However, considering the drag reduction advantages after adding the skin DTLMUW motions on streamlined body, they may provide additional skin-generated thrust, thereby helping to increase the swimming speed and improve the propulsion efficiency of dolphin.

The findings of the thesis demonstrate a novel active flow control strategy to achieve drag reduction by relying on the dynamic wall LMUW excitation and offers new insight into the sophisticated drag-reduction mechanisms in association with Gray’s paradox in dolphin

swimming. The results provide valuable inspiration for the development of bioinspired designs of drag reduction technology.

6.2 FUTURE RESEARCH DIRECTIONS

In this thesis, we investigate and discover the significant role of skin microvibrations on the excellent drag-reduction performance of dolphins, as well as its immense potential in elucidating the Gray's paradox, through a comprehensive CFD study. It is noteworthy that this study only simulates and discusses the realistic flow physics around the dynamic boundary induced by skin microvibrations, unveiling essential drag reduction mechanisms under the same shape parameters of skin microvibrations. In order to deeply uncover the mystery behind dolphin swimming, there is still a wealth of research content that needs to be expanded and investigated further.

(1) Based on the research by Haider et al. [126] and Ridgway et al. [99], we believe that skin microvibrations exists on the surface of dolphin, creating a dynamic skin boundary that results in significant drag reduction effects. However, we currently lack actual biological evidence because the data of skin microvibrations during the real swimming process of dolphins have not been truly measured. Therefore, we hope to combine the high-speed photography with high-precision flexible sensor technology to monitor the skin state under real dolphin swimming conditions, aiming to confirm the existence of this high-frequency, micro-vibration phenomenon on dolphin skin. In addition, the construction of actual measurement experiments can also be used to observe and capture the biological characteristics corresponding to the skin microvibrations of dolphin, providing practical biological evidence and data for the subsequent biomimetic design and research.

(2) In previous studies on drag reduction using static microstructures, whether inspired by sharks or dolphins, it has been pointed out that the influence of structural parameters on drag reduction performance cannot be overlooked [9–12,103]. Therefore, a systematic parametrical study associated with the LMUW in terms of wavelength, amplitude, frequency and uniformity is essential. Moreover, based on the data obtained from parameter studies, we can integrate artificial intelligence (AI) technology (machine learning or deep learning or generating AI) to identify optimal LMUW-based parameter design methods to achieve

better drag-reduction performance. This may have great application prospects, whether in the study of dolphin swimming performance or in the practical engineering applications, for instance the improvement of airfoil/hydrofoil performance.

(3) Although the simulation results have provided us with a lot of guidance and inspiration, our ultimate goal is to apply this novel drag reduction strategy to real engineering applicants. Therefore, we will focus on establishing a realistic dolphin-inspired LMUW model to offer a comprehensive solution to the Gray's paradox and developing a novel device capable of achieving the LMUW-based turbulent drag reduction using techniques of MEMS, biomaterials and ultrasonics in the future work.

REFERENCES

[1] A Abbas, J De Vicente, E Valero. Aerodynamic technologies to improve aircraft performance[J]. Aerospace Science and Technology, 2013, 28(1): 100-132.

[2] C Guo, Y Wu, Y Han, et al. Experimental study on influence of sharkskin denticles structure on the hydrodynamic performance of airfoil[J]. Ocean Engineering, 2023, 271: 113756.

[3] M Walsh. Turbulent boundary layer drag reduction using riblets[C]//20th Aerospace Sciences Meeting. Orlando,FL,U.S.A.: American Institute of Aeronautics and Astronautics, 1982.

[4] G D Bixler, B Bhushan. Fluid Drag Reduction with Shark-Skin Riblet Inspired Microstructured Surfaces[J]. Advanced Functional Materials, 2013, 23(36): 4507-4528.

[5] H Schlichting, K Gersten. Boundary-Layer Theory[M]. Berlin, Heidelberg: Springer Berlin Heidelberg, 2017.

[6] E Salimipour. On the moving surface impact on flow field and aerodynamic performance of a thick airfoil[J]. Ocean Engineering, 2024, 291: 116504.

[7] P Ricco, M Skote, M A Leschziner. A review of turbulent skin-friction drag reduction by near-wall transverse forcing[J]. Progress in Aerospace Sciences, 2021, 123: 100713.

[8] S Martin, B Bhushan. Fluid flow analysis of a shark-inspired microstructure[J]. Journal of Fluid Mechanics, 2014, 756: 5-29.

[9] S Martin, B Bhushan. Modeling and optimization of shark-inspired riblet geometries for low drag applications[J]. Journal of Colloid and Interface Science, 2016, 474: 206-215.

[10] T Wu, W Chen, A Zhao, et al. A comprehensive investigation on micro-structured surfaces for underwater drag reduction[J]. Ocean Engineering, 2020, 218: 107902.

[11] G Tian, D Fan, X Feng, et al. Thriving artificial underwater drag-reduction materials inspired from aquatic animals: progresses and challenges[J]. RSC Advances, 2021, 11(6): 3399-3428.

[12] L Li, J Zhu, J Li, et al. Effect of vortex frictional drag reduction on ordered microstructures[J]. Surface Topography: Metrology and Properties, 2019, 7(2): 025008.

[13] H Choi, P Moin, J Kim. Direct numerical simulation of turbulent flow over riblets[J]. Journal of Fluid Mechanics, 1993, 255(1): 503.

[14] E Bacher, C Smith. A combined visualization-anemometry study of the turbulent drag reducing mechanisms of triangular micro-groove surface modifications[C]//Shear Flow Control Conference. Boulder,CO,U.S.A.: American Institute of Aeronautics and Astronautics, 1985.

[15] C Huang, D Liu, J Wei. Experimental study on drag reduction performance of surfactant flow in longitudinal grooved channels[J]. Chemical Engineering Science, 2016, 152: 267-279.

[16] D W Bechert, M Bartenwerfer. The viscous flow on surfaces with longitudinal ribs[J]. Journal of Fluid Mechanics, 1989, 206: 105-129.

[17] D W Bechert, M Bruse, W Hage, et al. Experiments on drag-reducing surfaces and their optimization with an adjustable geometry[J]. Journal of Fluid Mechanics, 1997, 338: 59-87.

[18] L Wu, G Luo, F He, et al. Bionic research on *Paramisgurnus dabryanus* scales for drag reduction[J]. RSC Advances, 2022, 12(34): 22226-22235.
[19] J Wang, G Zhou, D Chen. Drag Reduction by Microvortexes in Transverse Microgrooves[J]. Advances in Mechanical Engineering.
[20] A Boomsma, F Sotiropoulos. Direct numerical simulation of sharkskin denticles in turbulent channel flow[J]. Physics of Fluids, 2016, 28(3): 035106.
[21] L Wu, J Wang, G Luo, et al. Study on the Drag Reduction Characteristics of the Surface Morphology of Paramisgurnus dabryanus Loach[J]. Coatings, 2021, 11(11): 1357.
[22] L Jiang, Y Zhao, J Zhai. A Lotus-Leaf-like Superhydrophobic Surface: A Porous Microsphere/Nanofiber Composite Film Prepared by Electrohydrodynamics[J]. Angewandte Chemie International Edition, 2004, 43(33): 4338-4341.
[23] W Barthlott, C Neinhuis. Purity of the sacred lotus, or escape from contamination in biological surfaces[J]. Planta, 1997, 202(1): 1-8.
[24] X Feng, P Sun, G Tian. Recent Developments of Superhydrophobic Surfaces (SHS) for Underwater Drag Reduction Opportunities and Challenges[J]. Advanced Materials Interfaces, 2022, 9(2): 2101616.
[25] V Zorba, E Stratakis, M Barberoglou, et al. Biomimetic Artificial Surfaces Quantitatively Reproduce the Water Repellency of a Lotus Leaf[J]. Advanced Materials, 2008, 20(21): 4049-4054.
[26] Z Q Tang, T Tian, P J Molino, et al. Recent Advances in Superhydrophobic Materials Development for Maritime Applications[J]. Advanced Science, 2024, 11(16): 2308152.
[27] K Watanabe, Y Udagawa, H Udagawa. Drag reduction of Newtonian fluid in a circular pipe with a highly water-repellent wall[J]. Journal of Fluid Mechanics, 1999, 381: 225-238.
[28] M A Samaha, H V Tafreshi, M Gad-el-Hak. Superhydrophobic surfaces: From the lotus leaf to the submarine[J]. Comptes Rendus. Mécanique, 2011, 340(1-2): 18-34.
[29] Y Zhao, Z Xu, L Gong, et al. Recoverable underwater superhydrophobicity from a fully wetted state via dynamic air spreading[J]. iScience, 2021, 24(12): 103427.
[30] S Srinivasan, J A Kleingartner, J B Gilbert, et al. Sustainable Drag Reduction in Turbulent Taylor-Couette Flows by Depositing Sprayable Superhydrophobic Surfaces[J]. Physical Review Letters, 2015, 114(1): 014501.
[31] S Zhang, X Ouyang, J Li, et al. Underwater Drag-Reducing Effect of Superhydrophobic Submarine Model[J]. Langmuir, 2015, 31(1): 587-593.
[32] D C Tretheway, C D Meinhart. Apparent fluid slip at hydrophobic microchannel walls[J]. Physics of Fluids, 2002, 14(3): L9-L12.
[33] M Li, W Xiao, Z Yin, et al. Construction of a robust MOF-based superhydrophobic composite coating with the excellent performance in antifouling, drag reduction, and organic photodegradation[J]. Progress in Organic Coatings, 2024, 186: 108086.
[34] J W Gose, K Golovin, M Boban, et al. Characterization of superhydrophobic surfaces for drag reduction in turbulent flow[J]. Journal of Fluid Mechanics, 2018, 845: 560-580.
[35] J Ou, J P Rothstein. Direct velocity measurements of the flow past drag-reducing ultrahydrophobic surfaces[J]. Physics of Fluids, 2005, 17(10): 103606.

[36] J Ou, B Perot, J P Rothstein. Laminar drag reduction in microchannels using ultrahydrophobic surfaces[J]. Physics of Fluids, 2004, 16(12): 4635-4643.
[37] H Wang, G Luo, L Chen, et al. Preparation of a bionic lotus leaf microstructured surface and its drag reduction performance[J]. RSC Advances, 2022, 12(26): 16723-16731.
[38] T Kim, R Shin, M Jung, et al. Drag reduction using metallic engineered surfaces with highly ordered hierarchical topographies: nanostructures on micro-riblets[J]. Applied Surface Science, 2016, 367: 147-152.
[39] J Hu, Z Yao. Drag reduction of turbulent boundary layer over sawtooth riblet surface with superhydrophobic coat[J]. Physics of Fluids, 2023, 35(1): 015104.
[40] J W Hoyt. Hydrodynamic Drag Reduction Due to Fish Slimes[M]//T Y T Wu, C J Brokaw, C Brennen. Swimming and Flying in Nature. Boston, MA: Springer US, 1975: 653-672.
[41] T L Daniel. FISH MUCUS: *IN SITU* MEASUREMENTS OF POLYMER DRAG REDUCTION[J]. The Biological Bulletin, 1981, 160(3): 376-382.
[42] B A Toms. Some observations on the flow of linear polymer solutions through straight tubes at large Reynolds numbers[C]//Proceedings of the 1st International Congress on Rheology: 卷 2. 1948: 135-141.
[43] P S Virk, E W Merrill, H S Mickley, et al. The Toms phenomenon: turbulent pipe flow of dilute polymer solutions[J]. Journal of Fluid Mechanics, 1967, 30(2): 305-328.
[44] J L Lumley. Drag reduction in turbulent flow by polymer additives[J]. Journal of Polymer Science: Macromolecular Reviews, 1973, 7(1): 263-290.
[45] T Kouser, Y Xiong, D Yang. Contribution of Superhydrophobic Surfaces and Polymer Additives to Drag Reduction[J]. ChemBioEng Reviews, 2021, 8(4): 337-356.
[46] G H Choueiri, J M Lopez, B Hof. Exceeding the Asymptotic Limit of Polymer Drag Reduction[J]. Physical Review Letters, 2018, 120(12): 124501.
[47] D Liu, S Wang, I Ivitskiy, et al. Enhanced drag reduction performance by interactions of surfactants and polymers[J]. Chemical Engineering Science, 2021, 232: 116336.
[48] X Dai, B Li, L Li, et al. Experimental research on the characteristics of drag reduction and mechanical degradation of polyethylene oxide solution[J]. Energy Sources, Part A: Recovery, Utilization, and Environmental Effects, 2021, 43(8): 944-952.
[49] D M Bushnell, J C Reed. Polymer/riblet combination for hydrodynamic skin friction reduction: NAS 1.71:LAR-14271-1-CU[P]. 1990-08-14.
[50] P Zhao, X Li, Z Luo, et al. A Bio-Inspired Drag Reduction Method of Bionic Fish Skin Mucus Structure[J]. Micromachines, 2024, 15(3): 364.
[51] S L Ceccio. Friction Drag Reduction of External Flows with Bubble and Gas Injection[J]. Annual Review of Fluid Mechanics, 2010, 42(1): 183-203.
[52] S A Makiharju, M Perlin, S L Ceccio. On the energy economics of air lubrication drag reduction[J]. International Journal of Naval Architecture and Ocean Engineering, 2012, 4(4): 412-422.
[53] H Wang, K Wang, G Liu. Drag reduction by gas lubrication with bubbles[J]. Ocean Engineering, 2022, 258: 111833.
[54] H J Park, Y Tasaka, Y Murai. Bubbly drag reduction accompanied by void wave generation inside

turbulent boundary layers[J]. Experiments in Fluids, 2018, 59(11): 166.
[55] T Tanaka, H J Park, Y Tasaka, et al. Spontaneous and artificial void wave propagation beneath a flat-bottom model ship[J]. Ocean Engineering, 2020, 214: 107850.
[56] B R Elbing, E S Winkel, K A Lay, et al. Bubble-induced skin-friction drag reduction and the abrupt transition to air-layer drag reduction[J]. Journal of Fluid Mechanics, 2008, 612: 201-236.
[57] P Du, J Wen, Z Zhang, et al. Maintenance of air layer and drag reduction on superhydrophobic surface[J]. Ocean Engineering, 2017, 130: 328-335.
[58] C Xu, B C Khoo. Dynamics of the supercavitating hydrofoil with cavitator in steady flow field[J]. Physics of Fluids, 2020, 32(12): 123307.
[59] M Mirzaei, H Taghvaei. A novel configuration optimization for high-speed ventilated supercavitating vehicles[J]. Ocean Engineering, 2019, 179: 13-21.
[60] D Yang, Y L Xiong, X F Guo. Drag reduction of a rapid vehicle in supercavitating flow[J]. International Journal of Naval Architecture and Ocean Engineering, 2017, 9(1): 35-44.
[61] G Chen, T Sun, S Yang, et al. A study on the cavitating flow around an elliptical disk-shaped cavitator for non-body-of-revolution underwater vehicles[J]. Engineering Applications of Computational Fluid Mechanics, 2023, 17(1): 2159882.
[62] C Yao, J Zhang, Z Xue, et al. Bioinspired Cavity Regulation on Superhydrophobic Spheres for Drag Reduction in an Aqueous Medium[J]. ACS Applied Materials & Interfaces, 2021, 13(3): 4796-4803.
[63] S K Robinson. Coherent motions in the turbulent boundary layer[J]. Annual review of fluid mechanics, 1991, 23(1): 601-639.
[64] H Choi, P Moin, J Kim. Active turbulence control for drag reduction in wall-bounded flows[J]. Journal of Fluid Mechanics, 1994, 262: 75-110.
[65] K Fukagata, K Iwamoto, Y Hasegawa. Turbulent Drag Reduction by Streamwise Traveling Waves of Wall-Normal Forcing[J]. Annual Review of Fluid Mechanics, 2024, 56(1): 69-90.
[66] T Min, S M Kang, J L Speyer, et al. Sustained sub-laminar drag in a fully developed channel flow[J]. Journal of Fluid Mechanics, 2006, 558: 309.
[67] J Hœpffner, K Fukagata. Pumping or drag reduction?[J]. Journal of Fluid Mechanics, 2009, 635: 171-187.
[68] R Moarref, M R Jovanović. Controlling the onset of turbulence by streamwise travelling waves. Part 1. Receptivity analysis[J]. Journal of Fluid Mechanics, 2010, 663: 70-99.
[69] B K Lieu, R Moarref, M R Jovanović. Controlling the onset of turbulence by streamwise travelling waves. Part 2. Direct numerical simulation[J]. Journal of Fluid Mechanics, 2010, 663: 100-119.
[70] P Luchini. Acoustic Streaming and Lower-than-Laminar Drag in Controlled Channel Flow[C]//L L Bonilla, M Moscoso, G Platero, et al. Progress in Industrial Mathematics at ECMI 2006: Vol. 12. Berlin, Heidelberg: Springer Berlin Heidelberg, 2008: 169-177.
[71] S Taneda, Y Tomonari. An experiment on the flow around a waving plate[J]. JOURNAL OF THE PHYSICAL SOCIETY OF JAPAN, 1974, 36(6): 1683-1689.
[72] L Shen, X Zhang, D K P Yue, et al. Turbulent flow over a flexible wall undergoing a streamwise travelling wave motion[J]. Journal of Fluid Mechanics, 2003, 484: 197-221.
[73] R Yamamoto, J Morita, H Mamori, et al. Turbulent channel flow controlled by traveling-wave-like

body force mimicking oscillating thin films[J]. Physics of Fluids, 2022, 34(8): 085106.
[74] J I Choi, C X Xu, H J Sung. Drag Reduction by Spanwise Wall Oscillation in Wall-Bounded Turbulent Flows[J]. AIAA Journal, 2002, 40(5): 842-850.
[75] W J Jung, N Mangiavacchi, R Akhavan. Suppression of turbulence in wall-bounded flows by high-frequency spanwise oscillations[J]. Physics of Fluids A: Fluid Dynamics, 1992, 4(8): 1605-1607.
[76] P Ricco, M Quadrio. Wall-oscillation conditions for drag reduction in turbulent channel flow[J]. International Journal of Heat and Fluid Flow, 2008, 29(4): 891-902.
[77] F Laadhari, L Skandaji, R Morel. Turbulence reduction in a boundary layer by a local spanwise oscillating surface[J]. Physics of Fluids, 1994, 6(10): 3218-3220.
[78] C Viotti, M Quadrio, P Luchini. Streamwise oscillation of spanwise velocity at the wall of a channel for turbulent drag reduction[J]. Physics of Fluids, 2009, 21(11): 115109.
[79] M Quadrio, P Ricco, C Viotti. Streamwise-travelling waves of spanwise wall velocity for turbulent drag reduction[J]. Journal of Fluid Mechanics, 2009, 627: 161-178.
[80] A Yakeno, Y Hasegawa, N Kasagi. Spatio-temporally periodic control for turbulent friction drag reduction[C]//Sixth International Symposium on Turbulence and Shear Flow Phenomena: Vol. 2. Begel House Inc.., 2009: 598-603.
[81] E Touber, M A Leschziner. Near-wall streak modification by spanwise oscillatory wall motion and drag-reduction mechanisms[J]. Journal of Fluid Mechanics, 2012, 693: 150-200.
[82] M Quadrio, C Viotti, P Luchini. Skin-friction Drag Reduction via Steady Streamwise Oscillations of Spanwise Velocity[M]//J M L M Palma, A S Lopes. Advances in Turbulence XI: Vol. 117. Berlin, Heidelberg: Springer Berlin Heidelberg, 2007: 659-661.
[83] P Ricco, S Wu. On the effects of lateral wall oscillations on a turbulent boundary layer[J]. Experimental Thermal and Fluid Science, 2004, 29(1): 41-52.
[84] W Yuan, M Zhang, Y Cui, et al. Phase-space dynamics of near-wall streaks in wall-bounded turbulence with spanwise oscillation[J]. Physics of Fluids, 2019, 31(12): 125113.
[85] M Umair, S Tardu, O Doche. Reynolds stresses transport in a turbulent channel flow subjected to streamwise traveling waves[J]. Physical Review Fluids, 2022, 7(5): 054601.
[86] M Albers, P S Meysonnat, D Fernex, et al. Drag Reduction and Energy Saving by Spanwise Traveling Transversal Surface Waves for Flat Plate Flow[J]. Flow, Turbulence and Combustion, 2020, 105(1): 125-157.
[87] Y Nabae, K Fukagata. Drag Reduction Effect of Streamwise Traveling Wave-Like Wall Deformation with Spanwise Displacement Variation in Turbulent Channel Flow[J]. Flow, Turbulence and Combustion, 2022.
[88] T Agarwal, B Cukurel, I Jacobi. Localized drag modification in a laminar boundary layer subject to free-stream travelling waves via critical and Stokes layer interactions[J]. Journal of Fluid Mechanics, 2022, 937: A10.
[89] Y Bengana, Q Yang, G Tu, et al. Exact coherent states in plane Couette flow under spanwise wall oscillation[J]. Journal of Fluid Mechanics, 2022, 947: A2.
[90] Y Huang, L Wang, S Fu. Drag reduction in turbulent channel flows by a spanwise traveling wave of wall blowing and suction[J]. Physics of Fluids, 2021, 33(9): 095111.

[91] S R Koh, P Meysonnat, V Statnikov, et al. Dependence of turbulent wall-shear stress on the amplitude of spanwise transversal surface waves[J]. Computers & Fluids, 2015, 119: 261-275.
[92] J Gray. Studies in animal locomotion: VI. The propulsive powers of the dolphin[J]. Journal of Experimental Biology, 1936, 13: 192-199.
[93] F E Fish, P Legac, T M Williams, et al. Measurement of hydrodynamic force generation by swimming dolphins using bubble DPIV[J]. Journal of Experimental Biology, 2014, 217(2): 252-260.
[94] F Fish, T Williams, E Sherman, et al. Experimental Measurement of Dolphin Thrust Generated during a Tail Stand Using DPIV[J]. Fluids, 2018, 3(2): 33.
[95] W F Perrin, W Bernd, J G M Thewissen. Encyclopedia of Marine Mammals[M]. second Edition. Academic Press, 2009.
[96] F E Fish. The myth and reality of Gray's paradox: implication of dolphin drag reduction for technology[J]. Bioinspiration & Biomimetics, 2006, 1(2): R17-R25.
[97] S Alben, M Shelley, J Zhang. Drag reduction through self-similar bending of a flexible body[J]. Nature, 2002, 420(6915): 479-481.
[98] E Liu, L Li, G Wang, et al. Drag reduction through self-texturing compliant bionic materials[J]. Scientific Reports, 2017, 7(1): 40038.
[99] S H Ridgway, D A Carder. Features of dolphin skin with potential hydrodynamic importance[J]. IEEE Engineering in Medicine and Biology Magazine, 1993, 12(3): 83-88.
[100] B Cozzi, S Huggenburger, H Oelschläger. Anatomy of Dolphins: Insights into Body Structure and Function[M]. Elsevier Academic Press, 2017.
[101] L Li, B Liu, H Hao, et al. Investigation of the drag reduction performance of bionic flexible coating[J]. Physics of Fluids, 2020, 32(8): 084103.
[102] A Bandari. Dolphin-inspired drag reduction coatings clarify the effects of elasticity and viscosity[J]. Scilight, 2020, 2020(32): 321108.
[103] T Zheng, J Liu, L Qin, et al. Effect of dolphin-inspired transverse wave microgrooves on drag reduction in turbulence[J]. Physics of Fluids, 2024, 36(1): 015157.
[104] M Hassanalian, H Abdelmoula, S Mohammadi, et al. Aquatic animal colors and skin temperature: Biology's selection for reducing oceanic dolphin's skin friction drag[J]. Journal of Thermal Biology, 2019, 84: 292-310.
[105] D K Wainwright, F E Fish, S Ingersoll, et al. How smooth is a dolphin? The ridged skin of odontocetes[J]. Biology Letters, 2019, 15(7): 20190103.
[106] M O Kramer. Boundary layer stabilization by distributed damping[J]. Journal of the American Society for Naval Engineers, 1960, 27(1): 25-34.
[107] C Yu, M Liu, C Zhang, et al. Bio-inspired drag reduction: From nature organisms to artificial functional surfaces[J]. Giant, 2020, 2: 100017.
[108] V V Pavlov. Dolphin skin as a natural anisotropic compliant wall[J]. Bioinspiration & Biomimetics, 2006, 1(2): 31-40.
[109] G Yunqing, L Tao, M Jiegang, et al. Analysis of Drag Reduction Methods and Mechanisms of Turbulent[J]. Applied Bionics and Biomechanics, 2017, 2017: 1-8.
[110] Y Q Gu, D S Dai, J G Mou, et al. Overview of the Mechanisms of Drag Reduction by Means

of Flexible Surfaces[J]. Journal of Biomimetics, Biomaterials and Biomedical Engineering, 2015, 23: 18-23.

[111] M Ahmad, M F Baig, S F Anwer. Turbulent drag reduction in compressible flows using streamwise traveling waves[J]. Physics of Fluids, 2024, 36(3): 035135.

[112] F C Li, Y Kawaguchi, K Hishida. Investigation on the characteristics of turbulence transport for momentum and heat in a drag-reducing surfactant solution flow[J]. Physics of Fluids, 2004, 16(9): 3281-3295.

[113] J W R Peeters, R Pecnik, M Rohde, et al. Turbulence attenuation in simultaneously heated and cooled annular flows at supercritical pressure[J]. Journal of Fluid Mechanics, 2016, 799: 505-540.

[114] M Hassanalian, A Abdelkefi, M Wei, et al. A novel methodology for wing sizing of bio-inspired flapping wing micro air vehicles: theory and prototype[J]. Acta Mechanica, 2017, 228(3): 1097-1113.

[115] M Hassanalian, H Abdelmoula, S Ben Ayed, et al. Thermal impact of migrating birds' wing color on their flight performance: Possibility of new generation of biologically inspired drones[J]. Journal of Thermal Biology, 2017, 66: 27-32.

[116] M Hassanalian, S B Ayed, M Ali, et al. Insights on the thermal impacts of wing colorization of migrating birds on their skin friction drag and the choice of their flight route[J]. Journal of Thermal Biology, 2018, 72: 81-93.

[117] M Hassanalian, G Throneberry, M Ali, et al. Role of wing color and seasonal changes in ambient temperature and solar irradiation on predicted flight efficiency of the Albatross[J]. Journal of Thermal Biology, 2018, 71: 112-122.

[118] H Nagamine, K Yamahata, Y Hagiwara, et al. Turbulence modification by compliant skin and strata-corneas desquamation of a swimming dolphin[J]. Journal of Turbulence, 2004, 5: N18.

[119] V Sokolov, I Bulina, V Rodionov. Interaction of Dolphin Epidermis with Flow Boundary Layer[J]. Nature, 1969, 222(5190): 267-268.

[120] A J Smits. Undulatory and oscillatory swimming[J]. Journal of Fluid Mechanics, 2019, 874: P1.

[121] H Liu, D Kolomenskiy, T Nakata, et al. Unsteady bio-fluid dynamics in flying and swimming[J]. Acta Mechanica Sinica, 2017, 33(4): 663-684.

[122] H Ahmad, M F Baig, P A Fuaad. Numerical investigation of turbulent-drag reduction induced by active control of streamwise travelling waves of wall-normal velocity[J]. European Journal of Mechanics - B/Fluids, 2015, 49: 250-263.

[123] T Endo, N Kasagi, Y Suzuki. Feedback control of wall turbulence with wall deformation[J]. 2000.

[124] S Kang, H Choi. Active wall motions for skin-friction drag reduction[J]. Physics of Fluids, 2000, 12(12): 3301-3304.

[125] H Tanaka, G Li, Y Uchida, et al. Measurement of time-varying kinematics of a dolphin in burst accelerating swimming[J]. R Gurka. PLOS ONE, 2019, 14(1): e0210860.

[126] M Haider, D B Lindsley. Microvibrations in Man and Dolphin[J]. Science, 1964, 146: 1181-1183.

[127] W M X Zimmer. Passive Acoustic Monitoring of Cetaceans[M]. first editor. Cambridge University Press, 2011.

[128] J Tougaard, L A Kyhn. Echolocation sounds of hourglass dolphins (Lagenorhynchus cruciger) are similar to the narrow band high-frequency echolocation sounds of the dolphin genus Cephalorhynchus[J]. Marine Mammal Science, 2009, 26(1): 239-245.

[129] W W L Au. Echolocation signals of wild dolphins[J]. Acoustical Physics, 2004, 50(4): 454-462.

[130] M L Melcón, M Failla,, M A Iñíguez. Echolocation behavior of franciscana dolphins (*Pontoporia blainvillei*) in the wild[J]. The Journal of the Acoustical Society of America, 2012, 131(6): EL448-EL453.

[131] L Fang, S Li, K Wang, et al. Echolocation signals of free-ranging Indo-Pacific humpback dolphins (*Sousa chinensis*) in Sanniang Bay, China[J]. The Journal of the Acoustical Society of America, 2015, 138(3): 1346-1352.

[132] V A Ryabov. Acoustic signals and echolocation system of the dolphin[J]. Biophysics, 2014, 59(1): 135-147.

[133] W W L Au, K J Benoit-Bird. Automatic gain control in the echolocation system of dolphins[J]. Nature, 2003, 423(6942): 861-863.

[134] M G Strahan, D S Houser, J J Finneran, et al. Behaviorally measured tactile sensitivity in the common bottlenose dolphin, *TURSIOPS TRUNCATUS* [J]. Marine Mammal Science, 2020, 36(3): 802-812.

[135] D Zhang, Y Jiang, H Chen, et al. Micro- and nano-bionic surfaces: biomimetics, interface energy field effects, and applications[M]. 1st ed. San Diego: Elsevier, 2021.

[136] M S Triantafyllou, G S Triantafyllou, D K P Yue. Hydrodynamics of Fishlike Swimming[J]. Annual Review of Fluid Mechanics, 2000, 32(1): 33-53.

[137] J H Ferziger, M Perić, R L Street. Computational Methods for Fluid Dynamics[M]. Cham: Springer International Publishing, 2020.

[138] ANSYS. ANSYS Fluent Theory Guide[Z]. 2013.

[139] S Kunze, C Brücker. Flow control over an undulating membrane[J]. Experiments in Fluids, 2011, 50(3): 747-759.

[140] S Shukla, N Thekkethil, A Sharma, et al. Hydrodynamics study on a traveling wave-based undulating surface of a hydrofoil in a free-stream flow[J]. Physical Review Fluids, 2022, 7(8): 084703.

[141] H Liu, S Wang, T Liu. Vortices and Forces in Biological Flight: Insects, Birds, and Bats[J]. Annual Review of Fluid Mechanics, 2024, 56(1): 147-170.

[142] K Uchino, H Mamori, K Fukagata. Heat transfer in fully developed turbulent channel flow with streamwise traveling wave-like wall deformation[J]. Journal of Thermal Science and Technology, 2017, 12(1): JTST0003-JTST0003.

[143] H Liu, K Kawachi. A Numerical Study of Undulatory Swimming[J]. Journal of Computational Physics, 1999, 155(2): 223-247.

[144] A J Smits, B J McKeon, I Marusic. High–Reynolds Number Wall Turbulence[J]. Annual Review of Fluid Mechanics, 2011, 43(1): 353-375.

[145] M Ohashi, K Fukagata, N Tokugawa. Adjoint-Based Sensitivity Analysis for Airfoil Flow Control Aiming at Lift-to-Drag Ratio Improvement[J]. AIAA Journal, 2021, 59(11): 4437-4448.

[146] X Tian, L Zhang, H Zhang, et al. The Optimal Lift–Drag Ratio of Underwater Glider for Improving Sailing Efficiency[J]. IEEE Journal of Oceanic Engineering, 2021, 46(3): 808-816.

[147] E Stanewsky. Adaptive wing and flow control technology[J]. Progress in Aerospace Sciences, 2001, 37(7): 583-667.

[148] M Quadrio, A Chiarini, J Banchetti, et al. Drag reduction on a transonic airfoil[J]. Journal of Fluid Mechanics, 2022, 942: R2.

[149] Z Wu, S Li, M Liu, et al. Numerical research on the turbulent drag reduction mechanism of a transverse groove structure on an airfoil blade[J]. Engineering Applications of Computational Fluid Mechanics, 2019, 13(1): 1024-1035.

[150] H Zong, Y Wu, H Liang, et al. Experimental Investigation and Intelligent Optimization of Airfoil Zero-Lift Drag Reduction with Plasma Actuators[J]. AIAA Journal, 2023, 61(1): 223-240.

[151] S S Chauhan, J R R A Martins. RANS-Based Aerodynamic Shape Optimization of a Wing Considering Propeller–Wing Interaction[J]. Journal of Aircraft, 2021, 58(3): 497-513.

[152] A G Domel, M Saadat, J C Weaver, et al. Shark skin-inspired designs that improve aerodynamic performance[J]. Journal of The Royal Society Interface, 2018, 15(139): 20170828.

[153] M Seyhan, M Sarioglu. Investigation of drag reduction performance of half NACA 0009 and 0012 airfoils placed over a trailer on the flow around truck-trailer[J]. Journal of Mechanical Science and Technology, 2021, 35(7): 2971-2979.

[154] V Kornilov. Combined Blowing/Suction Flow Control on Low-Speed Airfoils[J]. Flow, Turbulence and Combustion, 2021, 106(1): 81-108.

[155] M Atzori, R Vinuesa, G Fahland, et al. Aerodynamic Effects of Uniform Blowing and Suction on a NACA4412 Airfoil[J]. Flow, Turbulence and Combustion, 2020, 105(3): 735-759.

[156] P R Viswanath. Aircraft viscous drag reduction using riblets[J]. Progress in Aerospace Sciences, 2002, 38(6-7): 571-600.

[157] NACA0012 AIRFOILS (n0012-il)[EB/OL]. http://airfoiltools.com/airfoil/details?airfoil=n0012-il.

[158] C L Ladson. Effects of Independent Variation of Mach and Reynolds Numbers on the Low-Speed Aerodynamic Characteristics of the NACA 0012 Airfoil Section: NASA-TM-4074[R]. 1988.

[159] R E Sheldahl, P C Klimas. Aerodynamic characteristics of seven symmetrical airfoil sections through 180-degree angle of attack for use in aerodynamic analysis of vertical axis wind turbines: SAND-80-2114, 6548367[R]. 1981: SAND-80-2114, 6548367.

[160] C L Ladson, A S Hill, Wu G Johnson. Pressure Distributions from High Reynolds Number Transonic Tests of an NACA 0012 Airfoil in the Langley 0.3-Meter Transonic Cryogenic Tunnel: NASA-TM-100526[R]. 1987.

[161] N Gregory, C L O'Reilly. Low-Speed Aerodynamic Characteristics of NACA 0012 Aerofoi] Section, including the Effects of Upper-Surface Roughness Simulating Hoar Frost: R. & M. No. 3726[R]. 1973.

[162] J D Anderson. Fundamentals of aerodynamics[M]. Sixth edition. New York, NY: McGraw-Hill Education, 2017.

[163] X Wei, T Yan, J Liu, et al. Study on the interaction characteristics of hull-propeller-appendages

of autonomous underwater vehicle based on unsteady conditions[J]. Ocean Engineering, 2024, 312: 119087.

[164] Z Zhou, Z Li, X Yang, et al. Investigation of the wake characteristics of an underwater vehicle with and without a propeller[J]. Ocean Engineering, 2022, 266: 113107.

[165] J Kadiyam, S Mohan. Conceptual design of a hybrid propulsion underwater robotic vehicle with different propulsion systems for ocean observations[J]. Ocean Engineering, 2019, 182: 112-125.

[166] O Chocron, E P Vega, M Benbouzid. Dynamic reconfiguration of autonomous underwater vehicles propulsion system using genetic optimization[J]. Ocean Engineering, 2018, 156: 564-579.

[167] F E Fish, J J Rohr. Review of Dolphin Hydrodynamics and Swimming Performance:[R]. Fort Belvoir, VA: Defense Technical Information Center, 1999.

[168] X Wang, P Wei, Y Yuan, et al. Evaluation of Dolphin Swimming Speed and Thrust Based on CFD[J]. International Journal of Offshore and Polar Engineering, 2018, 28(2): 120-127.

[169] C Wei, Q Hu, Y Liu, et al. Performance evaluation and optimization for two-dimensional fish-like propulsion[J]. Ocean Engineering, 2021, 233: 109191.

[170] L Wang, C Wu. An adaptive version of ghost-cell immersed boundary method for incompressible flows with complex stationary and moving boundaries[J]. Science China Physics, Mechanics and Astronomy, 2010, 53(5): 923-932.

ACKNOWLEDGEMENTS

I would like to extend my deepest gratitude to my supervisor, Professor Hao Liu, for his invaluable guidance and support. I am also deeply thankful to my family and friends for their unwavering encouragement and motivation throughout this journey. My sincere thanks to Chiba University for the Excellent International Student Scholarship support, and lastly, to myself for persevering and not giving up.

LIST OF PUBLICATIONS

Journal publications:

1. Wang D. & Liu H., Turbulence drag reduction using dolphin-inspired near-wall ultrasonic microvibrations, Physical of Fluids, 36, 051910 (2024).
2. Wang D. & Liu H., Dolphin-inspired skin microvibrations offer a novel pressure-dominated drag reduction mechanism. Journal of Bionic Engineering, (2024).

Conference participation:

1. Wang D. & Liu H., Simulations of dolphin-inspired high-frequency oscillation-induced boundary layer flows. [The IACM 22nd Computational Fluids Conference, Cannes, 2023]
2. Wang D. & Liu H., A novel dolphin-inspired turbulent-drag reduction strategy: micro-ultrasonic wave-based oscillations. [The Japan Society of Mechanical Engineering, 34th Bio-Frontier Seminar, Ube, 2023]
3. Wang D. & Liu H., Can compliant skin vibration provide a novel drag reduction strategy in dolphin swimming? [The Society for Experimental Biology (SEB) Annual Conference, Prague, 2024]
4. Wang D. & Liu H., Turbulence drag reduction by active dolphin-inspired ultrasonic skin-microvibrations. [The Japan Society of Fluid Mechanics (JSFM) Annual Conference, Sendai, 2024]
5. Wang D. & Liu H., A novel drag reduction strategy inspired by skin microvibrations in dolphin swimming. [International Workshop on Bionic Engineering (IWBE) & International Symposium on Nature-Inspired Technology (ISNIT), Sydney, 2024]